Metal Clusters in a Bacterial Iron-Trafficking Protein

A Thesis Submitted for the Degree of

Doctor of Philosophy

By

Haizhong Zhu, *M.Phil.*

School of Chemistry

The College of Science and Engineering

The University of Edinburgh

September 2003

Abstract

Bacterial resistance to standard antibiotic therapies is a critical health problem worldwide. Antimicrobial-resistant infections that are essentially untreatable have begun to occur as epidemics around the globe. In this thesis, I have used the techniques of coordination chemistry, molecular biology, and protein X-ray crystallography to study metal binding to ferric ion binding protein (FBP), a highly-conserved 34 kDa periplasmic iron transporter, a candidate as target for novel metalloantibiotic design.

FBP from the human pathogen *Neisseria gonorrhoeae* was overexpressed with recombinant DNA technology. Metal-free FBP and reloaded Fe-NTA-FBP and Fe_3-FBP were fully characterised in solution and were crystallised. Structural comparisons among the crystal structure of *apo*-FBP (1.9 Å resolution), Fe-NTA-FBP (1.8 Å resolution) and Fe_3-FBP (1.8 Å resolution) show that the characteristic dityrosyl motif of FBP can assemble/bind metal clusters in the open metal binding cleft of the protein, although closure of the hinged metal-binding cleft and the presence of the synergistic anion (phosphate) are usually considered obligatory for strong metal binding by FBP. The role of dityrosyl motif in metal binding was confirmed by studies on two mutant FBPs (E57H FBP and Y195H Y196H FBP).

Hf(IV) was loaded on to *apo*-FBP under physiological conditions. Hf-FBP was characterised in solution and was crystallised. As observed for reload Fe-FBP, the crystal structure of Hf-bound form of FBP (1.7 Å resolution) shows that the phosphate ion in the crystal structure of *apo*-FBP can be displaced by mononuclear $[Hf(NTA)_2]^{2-}$, yielding a range of oxo Hf(IV) clusters containing from 3 to 5 metal ions bound to FBP strongly in the open metal-binding cleft of FBP.

The binding of vanadate to *apo*-FBP was studied by ^{51}V NMR, and the data suggest that vanadate can bind similarity to phosphate and also as a vanadium cluster. Crystals of V-FBP were obtained which diffract to 2.0 Å.

The work in this thesis suggests a novel metal acquisitive mechanism, which reveals the possibility that bacterial metal uptake is mediated by novel FBP intermediates including cluster adducts.

Acknowledgements

First of all, I would like to thank my supervisor Prof. Peter J Sadler for introducing me to this fascinating research field and his invaluable support in these three years.

I am very grateful to Dr. Dmitriy Alexeev for his expertise protein crystal structural determination work and to Dr. Dominic J Campopiano for allowing me to work in his laboratory and teaching me molecular biology. Both of them have given me many very helpful discussions and suggestions about the research work. In addition, I thank Dr. Dominic J. B. Hunter for teaching me molecular biology technologies.

Thanks also go to Dr. John A Parkinson and Dr. Claudia Blindauer for their help with NMR experiments, and to Dr. Lesley J Yellowlees for her help of EPR experiments, and to Dr. Simon Parsons for X-ray diffraction data collection on small molecules.

I would like to thank Prof. Malcolm D. Walkinshaw for allowing me to do protein crystallisation work in his labs.

Many thanks to all PJS group members, past and present, for their friendship and support. Many thanks also to all people working in this department at various positions for their sincere help.

Finally, I would like to thank The Overseas Research Students Awards Scheme (ORS) and The University of Edinburgh (Research Student Studentship) for funding.

Table of Contents

Chapter 1 Introduction

1.1 Metal Ions in Biological Systems

Metal ions play key roles in biological systems. It has been estimated that over 50% of all proteins will turn out to be metalloproteins [1]. Metal-ion-containing molecules generally serve important functions as electron carriers, metal storage sites, O_2 binding and storage sites and in signal transduction [2].

There is a tradition to use inorganic compounds for therapy. Platinum anticancer, gold antiarthritic and bismuth anticancer drugs have been developed. Metal complexes are routinely used as contrast agents for MRI and other imaging techniques [3]. A focal point of bioinorganic research is the chemistry of metal ions and their role for life [4].

The structures of metal complexes are important because research on mechanisms is based on structural research. To understand biological processes at the molecular level, with the help of modern technology, complete protein sequences and X-ray structures have been achieved for large complex molecules with important biological functions.

It is particularly important to understand the nature of the interactions of metallo-drugs with cell membranes, proteins, enzymes and DNA. The increasing knowledge of the role of metals in genetic regulation and the nature of metal sensor, transport and chaperone proteins will eventually have a major impact on drug design [2].

1.2 Bacterial Iron Uptake Systems

1.2.1 Iron Availability and Storage of Iron in Cells

Iron is essential for the growth of most bacteria due to its diverse roles in the biochemistry of the cell. In aerobic environments, the solubility of iron is very low at physiological pH (10^{-18} M). Hence, the bio-availability of iron is poor although iron

is the most abundant transition metal on Earth. Insoluble ferric hydroxide complexes form in solution, severely limiting the amount of free iron [5]. The majority of iron in a mammalian host is intracellular being present as haem compounds and iron-sulphur clusters in various proteins, and in the storage molecule ferritin. Extracellular iron is complexed to transferrin and lactoferrin, and sometimes to citrate [6, 7]. In order for iron to be used by a bacterium, specialised uptake mechanisms are necessary to extract iron from the environment or the host. Once inside the bacterial cell, the major role of iron is its involvement in enzymatic redox reactions. However, iron can also play a structural role in proteins and change the reactivity of active site residues [8].

1.2.2 Transport of Iron Across the Outer Membrane

Several types of iron uptake systems exist in bacteria to obtain iron from the environment or an animal host, by directly binding iron or iron-binding proteins or by utilizing iron chelators [9, 10, 11], which are low molecular compounds called siderophores, and have a high affinity for iron. Most pathogenic bacteria can procure iron directly from the host's iron-binding proteins, transferrin (Tf) and lactoferrin(Lf) [12, 13], or indirectly from haem from hemoglobin (Hb) [14]. Under anaerobic conditions, Fe(II) is present. It is sufficiently soluble that it can be taken up by anaerobic bacteria without the help of iron chelators. Similarly, acid-tolerant bacteria might find enough Fe(III), which has a solubility of 10^{-8} M at pH 3, to supply their iron needs.

In Gram-negative bacteria, access to the iron-binding proteins is prevented by the outer membrane, which forms a permeability barrier for substrates of more than 600 Da, so transport of iron in Gram-negative bacteria involves a specific outer membrane receptor whereas in Gram-positive organisms, which lack an outer membrane, the receptor protein is anchored by a covalently linked lipid [15]. A periplasmic transport protein and several inner membrane associated proteins complete the transport of iron into the cell [9, 10]. This arrangement of proteins from periplasm to cytoplasm is similar to other bacterial periplasmic protein-dependent

systems, termed ABC transporters (for ATP binding cassette-type transport), which transport amino acids, peptides and sugars into the cell [16, 17, 18].

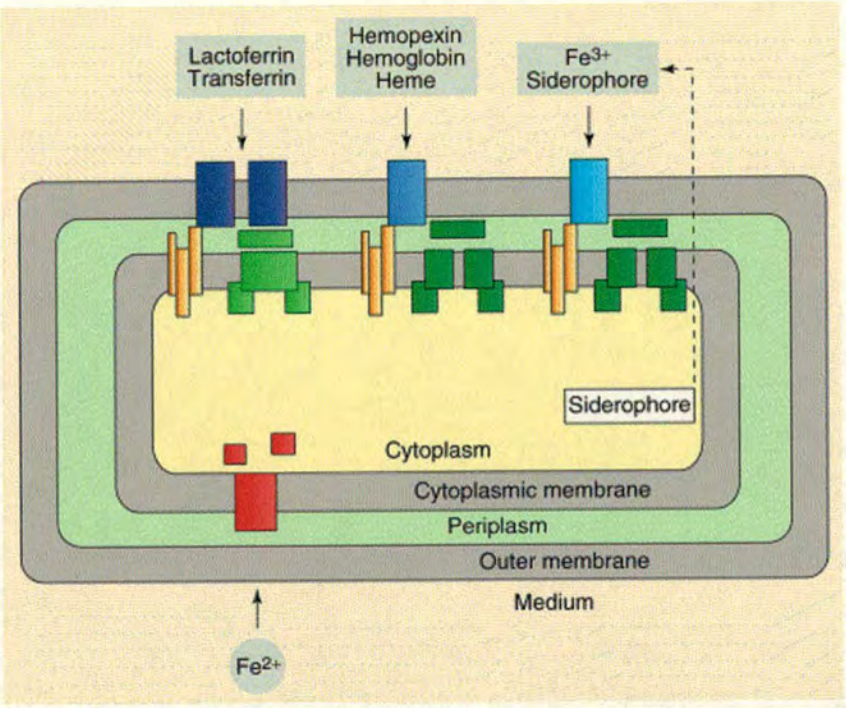

Figure 1.1 Fe(III) uptake system of Gram-negative bacteria. Fe(III) is delivered by lactoferrin or transferrin, haem or haem bound to hemoglobin or hemopexin of the host organisms, or siderophores. The receptor proteins (shown in blue) transport iron/iron ligand across the outer membrane: TbpA-TbpB (shown in darker blue) transports Fe(III); HasR (shown in mid-blue) transports haem, and FhuA (shown in lighter blue) transports ferrichrome. Active transport across the outer membrane is energized by the proton gradient across the cytoplasmic membrane. Presumably, conformational energy is transferred from the cytoplasmic membrane to the outer membrane by a protein complex consisting of the TonB, ExbB and ExbD proteins (shown in yellow). In the periplasm, Fe(III), haem or Fe(III) siderophores bind to binding proteins. The binding proteins deliver the iron compounds to transport proteins in the cytoplasmic membrane (shown in green); these transport proteins – for example, FhuB, translocates the iron compounds into the cytoplasm at the expense of ATP. The respective ATPases are associated with the inside of the

cytoplasmic membrane. Fe^{2+} presumably diffuses across the outer membrane and is actively transported across the cytoplasmic membrane by proteins (shown in red) [9].

Iron uptake does not necessarily begin with transport of iron by the requisite outer membrane receptors. Bacteria synthesise and secrete siderophores and hemophores in order to chelate iron or haem, and deliver them to the outer membrane receptors. The chemical structures of many different siderophores are well known [19]. Also, the structures of some outer membrane receptor proteins have been reported [22, 23, 24, 25].

A number of factors contribute to the existence of specific outer membrane receptors for ion uptake. Numerous receptors, between 75 and 85 kDa in size, bind their ligands with a very high affinity and with the specificity to transport compounds against a concentration gradient using energy from the inner membrane associated TonB-ExbB-ExbD complex [20, 21]. There is no source of energy in the form of an electrochemical gradient in the outer membrane nor are there any high energy compounds, such as ATP, in the periplasm. The initial transport across the outer membrane utilizes the electrochemical potential of the inner membrane. Its energy is coupled to the outer membrane by the TonB-ExbB-ExbD complex. Transferrin, Lactoferrin and haem protein receptors function to recruit these proteins to the cell surface and extract their iron. Although most substrates can diffuse through open porin channels in the outer membrane, haem complexes and ferric siderophores are too large to pass into the periplasm through this route, so outer membrane receptors are required to facilitate their transport. Since the concentration of ferric siderophores and haem in the external medium is low, high affinity receptor proteins are utilized by the bacterium, thereby concentrating them at the cell surface and increasing their rate of transport. Competition with other microrganisms for the same siderophore also favours having a receptor with high affinity. Since the receptor is usually rather specific for a particular compound, the bacteria can avoid taking up compounds which have antimicrobial effects, such as siderophore mimetic antibiotics [8].

1.2.2.1 Structure and Function of FepA, FhuA and FecA

The crystal structures of three outer membrane receptors for siderophores, ferric enterobactin receptor FepA [22], ferrichrome receptor FhuA [23, 24] and ferric citrate receptor FecA [25] from *E.coli* have been determined. The structures reveal interesting features that are likely to be related to their function and mechanism of transport utilised by other membrane receptors involved in ligand uptake. All three proteins are composed of three distinct domains: a barrel domain, a plug domain and a NH_2-terminal extension.

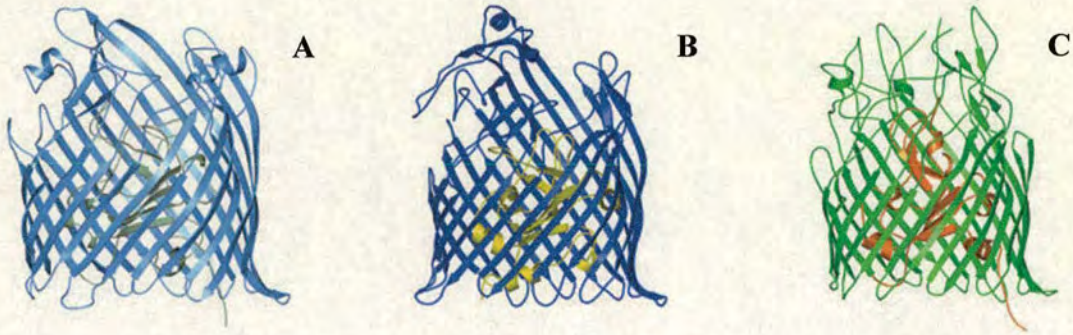

Figure 1.2 Comparison of the crystallographic structures of FecA, FhuA, and FepA in ribbon representation. (**A**) FecA, (**B**) FhuA, (**C**) FepA [26].

In all three structures, the monomeric transmembrane β-barrels are composed of 22 antiparallel strands. In *vivo*, these antiparallel strands transverse the outer membrane. Adjacent strands are connected by solvent-accessible extracellular loops containing two α-helices and three-β strands; turns are oriented toward to the periplasm. The position and length of these connecting segments are different for each receptor. Two girdles of aromatic residues inscribe the membrane-embedded hydrophobic surface of the receptor [25].

The plug domain of FecA is located inside the barrel, comprising five helices, two β-strands, and a mixed four-stranded β-sheet that is tilted by about 45° with respect to the membrane plane. FhuA and FepA present a similar fold [25].

The N-terminal domain folds in from the periplasmic side, almost filling up the space inside the barrel and contributing sites for ligand binding. The usual N-terminal cork domain found in both FepA and FhuA has been implicated in both siderophore recognition and binding. The domain sits in the β-barrel, anchored by more than 40 hydrogen bonds and several salt bridges with the barrel strands, blocking the pore. The unique fold of the domain allows several loops to rise above the bilayer interface extending towards the extracellular loops of the barrel. The N-terminal domain is important for function and the highest degree of sequence homology between these active transport proteins is found in this region [22]. Although the N-terminal residues appear to block the pore, a narrow water-filled channel in the FhuA structure connects the binding site to the periplasm [23]. Several residues in a loop of the cork domain [27] and along the inner wall of the barrel [23] are highly conserved between FhuA proteins in other bacteria. The flexible domain of FecA termed the NH_2-terminal extension was not visible in the electron density maps of the published crystal structure and could not be modelled [25]. The residues of this domain are entirely within the periplasm and transmit the liganded status of the receptor to FecR [28, 29].

The binding sites in three receptor proteins are different. In the structure of ferrichrome-bound FhuA, ferrichrome is found bound above the bilayer interface by interactions with residues from both the extracellular loops and the N-domain. The binding site of FhuA is predominantly formed by hydrophobic residues. The shape of the binding pocket, lined with aromatic residues, is highly complementary to the three dimensional conformation of ferrichrome. Three residues from the N-domain as well as two residues from the barrel form hydrogen bonds to ferrichrome, contributing to tight binding [23, 24]. Four hydrogen bonds are formed with the hydroxamic acid portion of the ferric siderophore while two more bonds form with the peptide backbone [8]. Tentative identification of the binding site residues in FepA involved in ferrienterobactin binding is based on the characteristics of the siderophore. From the position of the putative iron sites in the crystal structure [22] and mutagenesis studies [30], residues important in the binding site include aromatic

and positively-charged residues from both the extracellular loops and the N-domain loops. In the same way, residues from receptors involved in binding other siderophores would possess chemical and structural characteristics complementary to the ligand. In addition, receptors for the same siderophore in different species could possibly be structurally related [8]. A single dinuclear ferric citrate molecule can bind within the external pocket of FecA [25]. Three loops of the plug domain extend above the plane of the upper leaflet of the outer membrane. In the liganded structure, three loops together with residues located on extracellular loops form hydrogen bonds and electrostatic interactions with dinuclear ferric citrate.

Combined with the latest observations for this family of TonB-dependent receptors, a transport mechanism has been derived [25]. Stage 1: the siderophore is adsorbed from the medium with low affinity, primarily by aromatic residues found within the upper portion of the external pocket of the unliganded receptor. Stage 2: the siderophore is transferred to its high-affinity binding site, where primarily apices A, B, and C of the plug domain and numerous charged residues found within the extracellular loops and strands of the barrel form electrostatic contacts with the siderophore. These interactions cause translations of apices A, B, and C toward and away from the siderophore, as well as the concerted downward movement of other plug domain segments, leading to the unwinding and repositioning of the switch helix and the TonB-box. Stage 3: multiple extracellular loops of the receptor change their relative conformation and position. This bipartite gating mechanism closes the external pocket of the barrel, thereby favoring directed transport by disrupting the low-affinity binding site and shielding the high-affinity binding site from the solvent. However, the structural transitions observed in stages 2 and 3 may also be concerted. Stage 4: given the absence of an unobstructed channel of sufficient size to accommodate the passage of siderophores through TonB-dependent receptors, transitions that modify the conformation of the plug domain and/or barrel are required for transport. These changes are mediated by physical interactions between TonB and the TonB-box [31, 32, 33, 34], and possibly by periplasmic turns of the

barrel [35]. Formation of a complex with TonB results in the transfer of stored potential energy to the receptor [36], which in turn promotes ligand transport.

1.2.2.2 HasA Mediated Bacterial Haem Transport

Haemophores are extracellular proteins that acquire haem either from haemopexin, such as HxuA [37] or from various haemoproteins, such as HasA [38]. HasA haemoproteins are produced by several Gram-negative bacteria. They form an independent family of haem-binding proteins without homology to any other known proteins. HasA stands for haem acquision system which forms an independent family of haemoproteins that take up haem from the host and shuttles it to specific receptors, HasR [39]. The receptor is essential for haem acquisition, whereas the haemophore is not, although synergy between the haemophore and its receptor reduces the minimal haem or haemoglobin concentration required for growth by 100-fold [40].

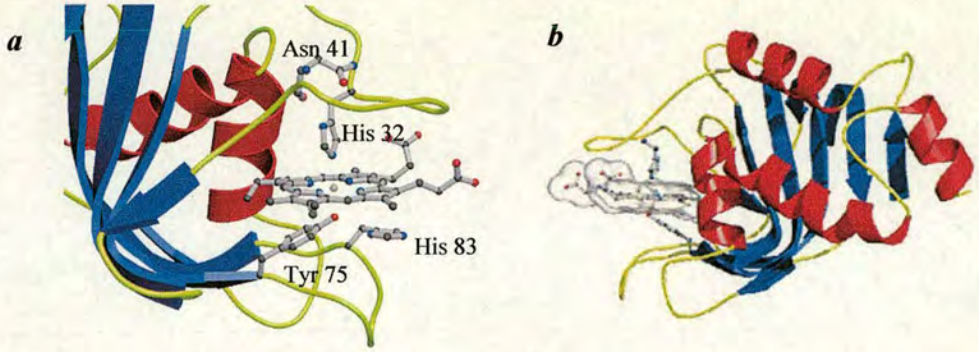

Figure 1.3 X-ray crystal structure of HasA. ***(a)*** View of the residues in the haem binding site. His 83 is presumed to be involved in both processes of haem capture and release. The residues and the haem are shown in ball-and-stick representation. The surrounding backbone is represented as a ribbon. ***(b)*** Backbone structure of HasA. Ribbon diagram with helices coloured in red and strands in blue. The ligands of the haem (His, Tyr) and the haem are shown in ball-and-stick representation. The surface occupied by the haem is transparent [43].

HasA from *S. marcescens* is a monomer (19 kDa) that binds b haem with a very high affinity and 1:1 stoichiometry. Both haem-free (*apo*protein) and haem-loaded (holoprotein) HasA bind to HasR, suggesting a direct protein-protein interaction in

the haem delivery mechanism. Haem iron in *holo*-HasA is in a low-spin ferric state and Fe is six coordinated at neutral pH [41]. The crystal structure of the holoprotein indicates that the haem is held by two loops and greatly exposed to solvent [42]. The iron atom is ligated by the N_ϵ atom of histidine 32 on one side and by the phenolate of tyrosine-75 on the other [43]. This residue pair, histidine-tyrosine, is a rare pattern of b haem ligation, only observed in *Chlamydomonas* chloroplast haemoglobin [44] and its various mutated proteins [45]. The phenolate of tyrosine-75 is also involved in a tight hydrogen bond with the N_δ atom of histidine 83. Some results from mutant protein show that Fe-Y75 ligation is stronger than Fe-H32 ligation. Mutation of H83 results in a significant loss of affinity, however, histidine-83 may become an alternative iron ligand in the absence of tyrosine-75. The triple mutant protein, H32A-Y75A-H83A, has no detectable affinity for haem at all [39].

Haemophores greatly facilitate haem acquisition via their specific receptors without being internalised with their ligand. Hence, haem uptake involves sequential steps: schematically (i) haemophore-receptor interaction; (ii) haem transfer from the haemophore to the receptor; and (iii) haem internalisation through the haemophore receptor channel. The investigations of mechanisms of these steps show that HasA binding to HasR involves protein-protein interactions and indicates that none of the haem-binding residues is required for this interaction [39]. Also, both *apo*- and *holo*-HasA bind with the same affinity to a common or overlapping site on HasR. These findings suggest that the recycling of haemophores at the cell surface when haem has been taken up does not occur by a mechanism of *apo*-haemophore ejection and replacement by newly loaded haemophore molecules. A preferred mechanism is haem exchange from a free loaded haemphore to a receptor-bound *apo*-haemophore. This mechanism allowing haem exchange from a loaded haemophore to a cell-bound *apo*-haemophore could involve interaction between the two haemophore forms or could be a consequence of the cell-bound form having a higher affinity for haem.

1.2.2.3 Structure and Function of the *Transferrin* Receptor TbpA and TbpB

The transferrin receptor consists of two types of subunits, TbpA and TbpB (transferrin-binding proteins A and B), both of which have the capacity to independently bind their ligand, human transferrin (htf) [46]. TbpA (100 kDa) is thought to be a porin-like integral membrane protein that is proposed to serve as a channel for the transport of iron across the outer membrane. TbpA shares sequence similarities with FepA and FhuA [47]. Both proteins have been shown to form an antiparallel β-barrel [22, 48], and TbpA is thought to have a similar structure [49]. TbpB (65-85 kDa) is considered to be an outer membrane protein that is anchored to the membrane via the lipidated N-terminal part of the protein [50, 51].

TbpB has two different isotypes, both isotypes differ in their molecular masses: isotype I proteins have molecular masses of ~68 kDa, whereas isotype II proteins are characterized by molecular masses of ~80-90 kDa [52]. The *apo*-htf binding to TbpA was substantially stronger than the value obtained for the binding of *holo*-htf. TbpA has an affinity ~20 times greater for *apo*-htf than *holo*-htf [53]. The mode of ligand binding is different for the two isotypes. The binding of *holo*-htf to isotype I TbpB is enthalpy-driven and opposed by an unfavorable entropy change. In contrast to the isotype I TbpB, the *holo*-htf binding to isotype II TbpB is driven by favorable entropy and enthalpy changes. The interaction of both TbpB isotypes with *apo*-htf is negligible. Furthermore, the number of binding sites (n) was found to be close to 1, confirming 1:1 stoichiometry for the binding of htf to TbpB [54]. When *holo*-htf binds to the mixture of TbpA and TbpB, it is found that a total of three *holo*-htf molecules are needed to saturate the receptor, contains one high affinity site and two low affinity sites. For TbpB, both N-ter (N-terminal domain of TbpB) and C-ter (C-terminal domain of TbpB) were found to contain very little secondary structure; this means a large part of both proteins is present in a coil conformation. However, the secondary structure content of a stoichiometric mix of both domains was found to be higher to that of both domains on their own. This is evidence that the domain interaction is accompanied by structural rearrangements. No interaction between *holo*-htf and C-ter was observed. TbpB, N-ter and C-ter were found to bind TbpA.

The binding of N-ter to TbpA is independent of its conformation; in contrast, C-ter binding to TbpA is conformation-specific [53].

1.2.3 ABC Transport Systems

ABC (ATP-binding cassette) transport systems, consist of a soluble periplasmic protein, a transmembrane permease and an ATP-binding lipoprotein, and are used for the uptake of many different ligands [55]. These proteins share consensus sequences which identify them as belonging to a particular family [17] but they cannot replace each other in different systems. In addition to those systems for transporting iron and iron complexes, similar ABC transport systems are found for amino acids, peptides, sugars, and other essential nutrients [16].

Although the periplasmic proteins in ABC transport systems share very little sequence homology and recognise diverse ligands, most are closely related in structure [18]. Periplasmic proteins can be grouped into distinct classes based on similarities in primary sequence [17]. Many consist of two globular domains connected by short stretches of polypeptide chain, which allow movement of the two lobes by a hinge mechanism. Each lobe consists of a central β-sheet flanked by α-helices, and molecular recognition of ligands arises from slight differences in the number and arrangement of the β-strands and α-helices in the two globular domains. As a result of the differences in domain structure and sequence of the periplasmic receptors, the structure of the binding site is highly variant. In most periplasmic proteins, cross-overs of the polypeptide chain between the two domains form the hinge region and the base of the binding cleft. The manner of closure around the substrate in the deep binding cleft formed by the two domains is suggestive of a "Venus fly trap" [56, 57] or "Pac-man" motion. This mode of binding gives rise to many interactions between the protein and substrate, conferring ligand binding selectivity to the protein [8].

The topology of typical periplasmic binding proteins is represented by the homologous iron-binding proteins FBP from *N. gonorrhoeae* and *H. influenzae* [58].

FBP can be described as "half transferrin". A detailed structural comparison between FBP and transferrin will be given in section **1.4**. Although the nature of the amino acid side-chains coordinating the iron are similar in FBP and transferrin, they arise from different regions of the protein. The iron is also more solvent-exposed in FBP than it is in the transferrins, since the iron binding site is deeper within the protein and the loop covering the binding site is missing. As such, FBP shares more structural similarity with other anion-binding periplasmic proteins such as the phosphate-binding protein, sulphate-binding protein, maltodextrin-binding protein, and spermidine-binding protein. Thus, the evolutionary descent of periplasmic and iron-binding proteins can be traced more accurately based on a combination of structural and sequence information (**Figure 1.6**). The *apo* form of FBP has the same overall fold but the two lobes of the protein are rotated by approximately 20° with respect to each other. Changes in the dihedral angles of the β-sheets lining the bottom of the binding site opens the binding cleft to the solvent [101].

Transport of ferric siderophores across the inner membrane is dependent upon the energy provided by respective cytoplasmic membrane-associated components. Studies of ABC transport systems for maltose and histidine show that only the ligand-loaded binding proteins initiate ATP hydrolysis [59], preventing wasteful hydrolysis. This implies that a signal from the periplasmic protein to the ATPase component of the ABC transport system must occur at some point to allow ATP hydrolysis [8].

1.3 Structure and Function of Transferrin

The transferrins comprise a class of iron-binding proteins, which are known to be at least as ancient as the insects [60]. There are major classes of transferrins: serum transferrin, lactoferrins and ovotransferrins. They are all monomeric glycoproteins with an approximate molecular mass of 80 kDa, bind two ferric ions per molecule with high affinity, and have high sequence similarity. Serum transferrins or serotransferrins are responsible for the transportation of iron in serum and delivery of iron to cells via receptor-mediated endocytosis [61]. Ovotransferrins (formerly called

conalbumin) are found in avian egg whites and are identical to their serum counterpart except for their attached carbonhydrates [62], and are also capable of serving as an iron donor for immature erythrocytes in the avian embryo [63], but can not bind to mammalian receptors. Lactoferrins or lactotransferrins are found in numerous extracellular fluids and in the specific granules of polymorphonuclear lymphocytes and are known to be multifunctional, acting as antimicrobial agents [64], antifungal agents [65] and sequence-specific DNA-binding moieties [66].

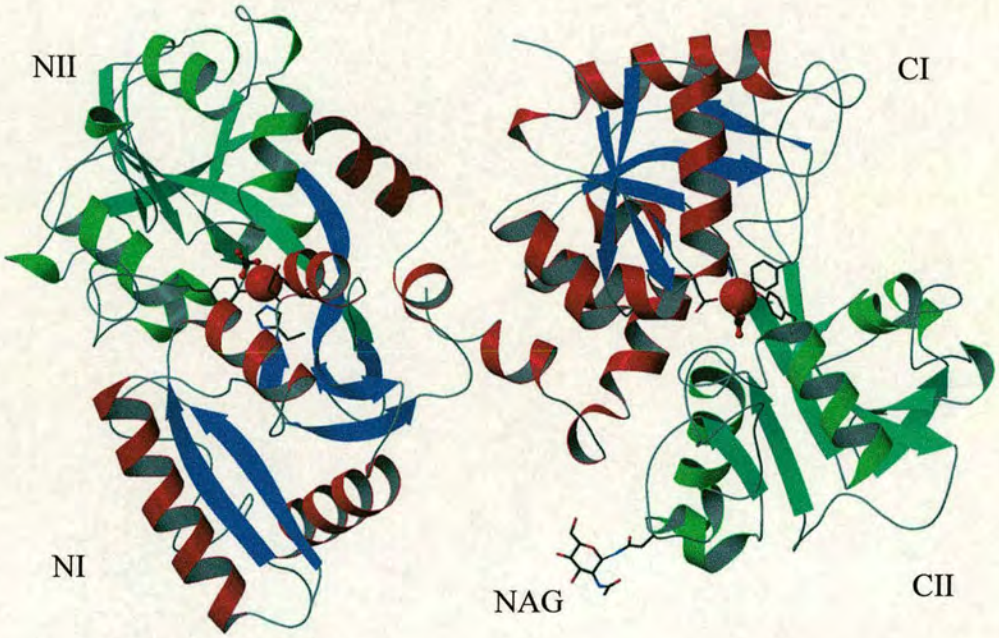

Figure 1.4 A model of porcine serum transferrin showing the bilobal structure and domain arrangement whereby NI is equivalent to CI (red and blue secondary structure) and NII is equivalent to CII (green and cyan secondary structure). The liganded iron and carbonate of both lobes is shown. The *N*-acetyl glucosamine (*N*AG) that is covalently linked to Asn497 is shown in stick representation [67].

The three-dimensional arrangements of all the members of the transferrin family whose structures have so far been determined are fundamentally the same. **Figure 1.4** shows the structure of pST (porcine serum transferrin). The polypeptide chain of transferrin is disposed in two lobes, representing the N-terminal and C-terminal halves of the molecule. Each lobe of the transferrin structure is split into two

dissimilar domains (NI and NII, CI and CII in **Figure 1.4**) with a deep cleft in between where the Fe(III) cation is bound in conjunction with the synergistic carbonate anion. In both lobes the similar NII and CII domains are formed from a continuous polypeptide separating the two regions that make up the similar domains NI and CI. It can be seen that each domain has a central mixed β-sheet flanked on either side by α-helices. The folding of the domains is an approximate β / α repeat. Two antiparallel β-strands connect the two domains of each lobe and form the hinge region about which the domain II pivots to give the open-lobe form of the *apo* protein. A short sequence connects both two lobes and takes the form of a helix in human lactoferrin and a β-strand in rabbit serum transferrin [68].

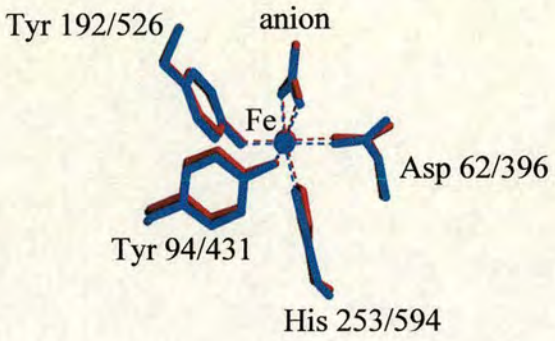

Figure 1.5 The iron-binding sites of porcine serum transferrin: the overlay of the iron ligands of N-lobe and C-lobe, where the components of the N-lobe are in red and those of the C-lobe in blue [67].

The binding of iron by serum transferrin is sufficiently strong to resist hydrolysis [69], and it is physiologically reversible. The iron-binding sites in each lobe of porcine serum transferrin are very similar and comprise a distorted octahedral coordination involving four protein ligands, namely two tyrosines, a histidine, an aspartate and a bidentate synergistic carbonate anion. For pST, the protein ligands are Tyr94 and Tyr192 in the N-lobe (Tyr431 and Tyr526 in the C-lobe), His253 in the N-lobe (His594 in the C-lobe) and Asp62 in the N-lobe (Asp396 in the C-lobe). The aspartate residues have a dual role, they not only bind to iron, but also make hydrogen bonds with residues at the N-termini of α-helices, thereby helping to stabilise the lobe in closed conformation when metal is bound, but leaving it in an

open conformation in the absence of metal [70]. The synergistic anion of iron-transferrin is carbonate, acting as a bridging ligand between protein and metal ion and completing the coordination needs of the metal ion. The carbonate is bidentate and binds between the iron and a positively-charged site on domain II of each lobe. When carbonate is absent, a variety of other bifunctional anions bearing at least one carboxylate group may take its place [71]. Iron is the most strongly bound metal to transferrin, however, human transferrin can accommodate a wide variety of other metals, more than 35 have been identified, metal ions with electron or nuclear paramagnetism have been especially valuable in probing the metal-binding properties of transferrins [4].

Numerous crystallographic structures of transferrins from the three major classes have been solved. However, relatively few precise structural data are available for the serum transferrins, the first solved being the diferric form of rST (rabbit serum transferrin) at a resolution of 3.3 Å [72]. Other partial structures of serum transferrins include the N-terminal half domain from rST [73] and several recombinant N-lobe mutants of hST (human serum transferrin) [74, 75, 76, 77]. The structure of the human serum transferrin with Fe in the C-lobe only has also been reported at a resolution of 3.3 Å [78]. A high resolution structure (2.15 Å) of porcine serum transferrin shown above was reported recently [67], and it is a good example for the detailed structure of serum transferrin.

Table 1.1 X-ray crystal structures of transferrins released in Protein Data Bank [79]

PDB ID	**Source**	**Descriptor**
1A8E	Homo sapiens	Recombinant N-lobe of human transferrin reveals a structural change implicated in iron release ($P2_12_12_1$)
1A8F	Homo sapiens	Same as 1A8E, but different space group ($P4_12_12$)
1B3E	Homo sapiens	Human serum transferrin, N-terminal lobe,

PDB ID	Source	Descriptor
		expressed in *Pichia pastoris*
1BP5	Homo sapiens	Human serum transferrin, recombinant N-terminal lobe, *apo* form
1BTJ	Homo sapiens	Human serum transferrin, recombinant N-terminal lobe, *apo* form, crystal form 2
1FQE	Homo sapiens	Mutant (K206A) that abolish the dilysine interaction in the N-lobe of human transferrin
1FQF	Homo sapiens	(K296A) that abolish the dilysine interaction in the N-lobe of human transferrin
1JNF	Oryctolagus cuniculus	Rabbit serum transferrin
1JQF	Homo sapiens	Human transferrin N-lobe mutant H249Q
1N7W	Homo sapiens	Human serum transferrin, N-Lobe L66W Mutant
1N7X	Homo sapiens	Human serum transferrin, N-Lobe (Y45E)
1N84	Homo sapiens	Human serum transferrin, N-lobe
1OQG	Homo sapiens	D63E mutant of the N-lobe human transferrin
1OQH	Homo sapiens	R124A mutant of the N-lobe human transferrin
1D3K	Homo sapiens	Two mutants (K206Q, H207E) of the N-lobe of human transferrin with increased affinity of iron
1D4N	Homo sapiens	Two mutants (K206Q, H207E) of the N-lobe of human transferrin

PDB ID	Source	Descriptor
1DTG	Homo sapiens	Human transferrin N-lobe mutant H249E
1B0L	Homo sapiens	Recombinant human diferric lactoferrin
1BIX	Equus caballus	Structure of diferric mare lactoferrin
1BIY	Bubalus arnee bubalis	Structure of diferric buffalo lactoferrin
1BKA	Homo sapiens	Oxalate-substituted diferric lactoferrin
1BLF	Bos taurus	Structure of diferric bovine
1CB6	Homo sapiens	Structure of human *apo*lactoferrin
1CE2	Bubalus arnee bubalis	Structure of diferric buffalo lactoferrin
1DTZ	Camelus dromedarius	Crystal structure of camel *apo*-lactoferrin
1EH3	Homo sapiens	R210K N-terminal lobe human lactoferrin
1F9B	Mare colustru	X-Ray structure of the complex of mare lactoferrin with melanin monomers
1FCK	Homo sapiens	Structure of diceric human lactoferrin
1H43	Homo sapiens	R210E N-terminal lobe human lactoferrin
1H44	Homo sapiens	R210L N-terminal lobe human lactoferrin
1H45	Homo sapiens	R210G N-terminal lobe human lactoferrin
1HSE	Homo sapiens	H253M N-terminal lobe of human lactoferrin
1I6B	Equus caballus	Equine *apo*lactoferrin

PDB ID	Source	Descriptor
1I6Q	Camelus dromedarius	An iron-saturated intermediate in the ferric iron binding pathway of camel lactoferrin
1L5T	Homo sapiens	A domain-opened mutant (R121D) of the human lactoferrin N-lobe
1LFG	Homo sapiens	Diferric lactoferrin
1LFH	Homo sapiens	Structure of *apo*lactoferrin, a protein displaying large-scale conformational change
1LFI	Homo sapiens	Crystal structure of human copper-lactoferrin
1LGB	Homo sapiens	A legume lectin complexed with the human lactotransferrin N2 fragment, and with an isolated biantennary glycopeptide
1LGC	Lathyrus ochrus	A legume lectin complexed with the human lactotransferrin N2 fragment, and with an isolated biantennary glycopeptide
1N76	Homo Sapiens	Human seminal lactoferrin
1QJM	Equus caballus	A complex of lactoferrin with Sm(III)
1VFD	Homo sapiens	Human lactoferrin, N-Terminal lobe mutant (R121E)
1VFE	Homo sapiens	Human lactoferrin, N-terminal lobe mutant (R121S)
1AIV	Gallus gallus	hen ovotransferrin, *apo* form

PDB ID	Source	Descriptor
1AOV	Anas platyrhynchos	*Apo* duck ovotransferrin
1DOT	Anas platyrhynchos	Diferric duck ovotransferrin
1GV8	Anas platyrhynchos	18 Kda fragment of N-II domain of duck ovotransferrin
1GVC	Anas platyrhynchos	18Kda N-II domain fragment of duck ovotransferrin + NTA
1IEJ	Gallus gallus	Ovotransferrin, N-terminal lobe, *holo* form
1IQ7	Gallus gallus	Ovotransferrin, C-terminal lobe, *apo* Form
1JL4	Homo sapiens	Human Cd4 N-terminal two domain fragment complexed to a class II mhc molecule
1JL4	Mus musculus	Human Cd4 N-terminal two domain fragment complexed to a class II mhc molecule
1JL4	Gallus gallus	Human Cd4 N-terminal two domain fragment complexed to a class II mhc molecule
1NFT	Gallus gallus	Ovotransferrin, N-terminal lobe, iron loaded open form
1NNT	Gallus gallus	pH-sensitive dilysine trigger in the hen ovotransferrin N-lobe
1OVB	Anas sp.	The structure of an 18 Kda Nii-domain fragment from duck ovotransferrin
1OVT	Gallus gallus	Diferric hen ovotransferrin

PDB ID	Source	Descriptor
1TFA	Gallus gallus	Ovotransferrin, N-Terminal lobe, *apo* Form
1TFD	Oryctolagus cuniculus	Rabbit serum transferrin - preliminary structure-analysis of the N-terminal half-molecule
1H76	Sus scrofa	Diferric porcine serum transferrin

All nonhaem iron in the circulation is normally carried by transferrin. In disorders characterised by iron overload, such as transfusion-dependent thalassemia and hemochromatosis, nonhaem iron may also be found in the plasma. Such iron, largely as its complex with citrate [80], maybe more reactive and available than transferrin-borne iron [81] and hence a threat to virtually all cells and tissues [4].

Although transferrin binds iron tightly at physiological pH, transferrin may relinquish Fe(III) to other molecules of biological interest. In the presence of citrate, intermolecular transfer of iron among transferrin molecules themselves can occur [82]. Ferritin is the major intracellular storage depot for iron, it is described as "bag of iron". Its hollow spherical structure can accommodate up to 4500 atoms of iron (as hydrated ferric oxide), deposited when iron is plentiful and released when iron is scarce. When ferritin is mixed with *apo*-transferrin, iron can be delivered from ferritin to transferrin, and the reaction rate is doubled by 1 mM citrate [83]. If the proteins are separated by a dialysis membrane, no exchange of iron is observed in the absence of a mediating agent, this reveals the importance of iron carriers in intracellular iron metabolism. Other proteins, like hemoglobin in the reduced, native state can accept iron from transferrin. Uteroferrin, with mediating agents such as citrate, pyrophosphate, ATP or ascorbate, can transport iron to transferrin unidirectionally [84].

Many important human pathogens, among them *Haemophilus influenzae, Neisseria meningitidis*, *Moraxella catarrhalis*, and *Neisseria gonorrhoeae*, are capable of securing iron from transferrin or lactoferrin. To accomplish this, they elaborate a pair

of transferrin-binding proteins, TbpA and TbpB, or LbpA and LbpB, which act in concert to trap transferrin [13]. The pathogens are not known to elaborate siderophores, but effectively remove iron from transferrin by a process involving these transferrin receptors [85]. The primary site in the human transferrin molecule recognised by the bacterial receptors is in the C-lobe [86], as is the site for recognition by the human transferrin receptor. A soluble iron-binding protein in the periplasmic space of pathogenic *Neisseria* has a function in the delivery of iron from simple iron chelates to the bacteria [4].

1.4 Structure and Function of FBP from *Neisseria Gonorrhoeae*

FBP is ferric ion binding protein. It is found in for example *Haemophilus influenzae* (*h*FBP), *Neisseria gonorrhoeae*, *Neisseria meningitidis* (*n*FBP), *Serratia marcescens* (*s*FBP), *Yersinia enterocolitica* (*y*FBP) [87, 88, 89, 90], and belongs to the superfamily of transferrin proteins, which encompasses the mammalian transferrin proteins [91].

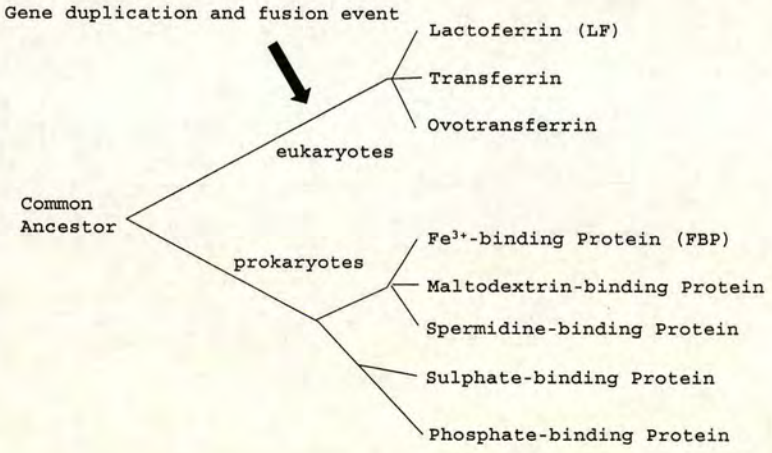

Figure 1.6 Deduced evolutionary tree for selected members of the transferrin superfamily, based on comparison of structures and sequences. This tree combines the transferrins with periplasmic transport proteins in clusters I (sulphate- and phosphate-binding) and VI [Fe(III)- and maltodextrin- binding] based on the analysis of Tam and Saier [17]. Clusters II, III, and IV of the prokaryotic periplasmic transport proteins are also related by evolutionary descent, based on the topological

similarity of known crystal structures, but may lie outside the pattern shown here [58].

FBP is a periplasmic binding protein, it is a convergent nodal point for Fe(III) trafficking subsequent to a variety of very different transport strategies across the outer membrane [92]. Recombinant FBP (*r*FBP) has been cloned and overexpressed in *Escherichia coli*, allowing for its efficient purification in near-gram quantities [94]. Wild-type FBP is pink and the molecular mass is 33 606 Da [93]. It is a basic protein (pI > 9.35) comprised of 309 residues [94, 95]. One FBP molecule is thought to bind only to one ferric ion [96]. Circular dichroism analysis of purified FBP indicates an α-helix/β-sheet content of 32/27% [97].

Figure 1.7 Crystal structure of *holo*-FBP from *Neisseria gonorrhoeae* (left), and its metal binding site (right). Tyr195, Tyr196 (yellow), His9 (blue), Glu57 (red), phosphate and a water bind to Fe(III) with octahedral geometry [98].

In FBP, six ligands coordinate the Fe(III) with nearly ideal octahedral geometry. The protein itself contributes tyrosinate oxygen ligands from Tyr195 and Tyr196, a

carboxylate oxygen ligand from Glu 57, and an imidazole nitrogen ligand from His 9. Two additional oxygen ligands are provided by a water molecule and an exogenous phosphate ion (**Figure 1.7**).

FBP is critical for the transport of growth-essential Fe(III) from the periplasm into the bacterial cytosol [99]. It is characteristic of the well-described class of periplasmic binding proteins, but is unique in that it functions in the transport of iron [100]. The function of FBP is summarised in **Figure 1.8**. The transportation of the Fe(III) into the bacterial cell requires the direct interaction of the host protein and a bacterial surface-associated Tf or Lf receptor. Pathogenic bacteria express Tf and Lf receptors that bind the host iron-binding proteins with micro-molar affinities, whereupon iron is extracted directly from Tf or Lf [51]. This step is typified by binding Tf to the bacterial heterodimeric receptor complex consisting of transferrin-binding proteins TbpA and TbpB [101].

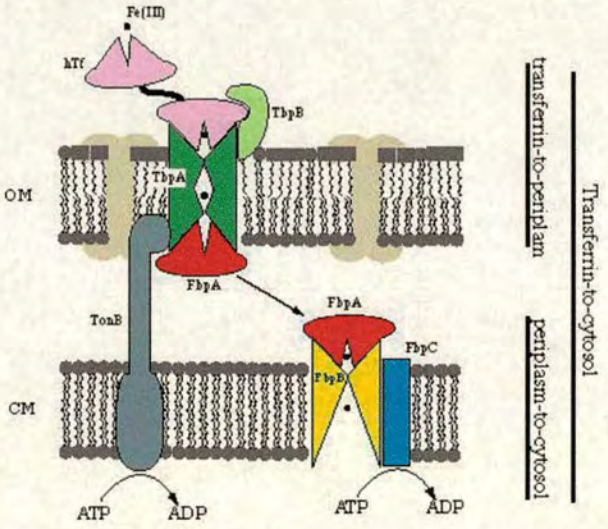

Figure 1.8 Model of iron transport from transferrin to the cytosol in pathogenic *Neisseria* and *H. influenzae* [103].

The process by which the iron is extracted from Tf and shuttled across the outer membrane and into the periplasmic space remains largely undescribed. However, an energy source mediated by TonB and associated proteins (ExbB and ExbD) is generally considered to be required [102]. After transport across the outer membrane,

free iron associates with the periplasmic Fe(III) binding protein FBP [89]. Transport of iron from FBP across the cytoplasmic membrane is accomplished using a free-iron ABC transporter, consisting of a genetically linked permease and ATP binding protein [90, 103]. Cytoplasmic iron is then assimilated directly into iron-coordinating proteins or prosthetic groups (e.g., haem), or is stored in the form of bacterioferritin [104].

Transferrin and FBP operate in different compartments (serum *vs* periplasm) and have arisen through separate evolutionary lineages, However, FBP is structurally and functionally analogous to one lobe of transferrin without sequence homology [96, 58]. Nevertheless, there are crucial differences in iron binding between FBP and transferrin. The coordination of the iron by the oxygens of two tyrosines, an imidazole nitrogen from histidine are the same for FBP as for transferrin, but FBP completes the octahedral coordination of Fe(III) with oxygens from a glutamate, phosphate and a water molecule, whereas transferrins utilize the oxygen from an aspartate and two oxygens from a carbonate anion [58], and no water molecule is involved in Fe(III) binding in transferrin. Although similar amino acid residues are used to bind Fe(III) in both FBP and transferrin, the residues come from different parts of the polypeptide chain, this suggests that FBP and transferrin are descended from an iron-binding common ancestor [58].

Table 1.2 Comparison of properties of hTf, hLf, and Fbp [96]

Characteristic	**Transferrin**	**Lactoferrin** [105]	**FBP**
Molecular Mass (Da)	74,000-80,000	80,000-92,000	33,642
Bound Fe	Ferric	Ferric	Ferric
Fe(III)-binding sites	two, one per lobe	two, one per lobe	one
UV-Vis, λ_{max} [Fe(III)-bound]	470 nm	460 nm	481 nm

The transferrins can efficiently bind metals other than iron, including Al(III), Ga(III), Cu(II), Zn(II), Cr(III), and Tb(III), among a total of 35 elements [105]. Due to the structural and functional homology of FBP and transferrin, based on the previous research on transferrin, binding of *apo*-FBP to some other metals has been investigated [96, 107]. The results suggest that the same range of metal binding can occur within FBP that is characteristic of the transferrins.

1.5 Aims of the Project

The aims of this work were as follows

(1) To prepare recombinant FBP and investigate methods for reconstituting with iron, and especially the possibility that FBP may bind clusters of iron atoms.

(2) To investigate the possibility that Hf(IV) can bind to FBP and replace Fe(III) from FBP and therefore to be a candidate metalloantibiotic.

(3) To study the binding of vanadate to FBP and the possibility that vanadate can not only bind to the Fe(III) site, but also mimic the binding of phosphate.

A particular aim of this project was also to crystallise novel metal adducts of FBP for X-ray structural determination.

References

1 Thomson, A.J., Gray, H.B., *Curr. Opin. Chem. Biol.* **2** 155 (1998).

2 Shriver, D.F.; Atkins, P.W., *Inorganic Chemistry,* **Third Edition**, Oxford, pp 645 (1999).

3 Broderick J.B., Coucouvanis D., *Curr. Opin. Chem. Biol.* **7** 157 (2003).

4 Sigel, A., Sigel, H., *Met. Ions Biol. Syst.*, Marcel Dekker, New York **v35** (1998).

5 Crichton, R. R., *Inorganic Biochemistry of Iron Metabolism*, Ellis Horwood: New York (1991).

6 Griffiths, E., *Biol. Met.*, **4**, 7 (1991).

7 Payne, S.M., *Trends. Microbiol.*, **1**, 66 (1993).

8 Clarke, T. E., Tari, L. W., Vogel, H. J., *Curr. Top. in Med. Chem.*, **1**, 7 (2001).

9 Braun, V., Killmann, H., *Trends Biochem. Sci.*, **24**, 104 (1999).

10 Schryvers, A. B., Stojiljkovic, I., *Mol. Microbiol.*, **32**, 1117 (1999).

11 Vasil, M. L., Ochsner, U. A., *Mol. Microbiol.*, **34**, 399 (1999).

12 Wolz, C., Hohloch, K., Ocaktan, A., Poole, K., Evans, R. W., Rochel, N., Albrecht-Gary, A. M., Abdallah, M. A., Doring, G., *Infect. Immun.*, **62**, 4021 (1994).

13 Cornelissen, C. N., Sparling, P. F., *Mol. Microbiol.*, **14**, 843 (1994).

14 Dyer, D. W., West, E. P., Sparling, P. F., *Infect. Immun.*, **55**, 2171 (1987).

15 Cockayne, A., Hill, P. J., Powell, N. B., Bishop, K., Sims, C., Williams, P., *Infect. Immun.*, **66**, 3767 (1998).

16 Higgins, C. F., *Annu. Rev. Cell. Biol.*, **8**, 67 (1992).

17 Tam, R., Saier, M. H., Jr. *Microbiol. Rev.*, **57**, 320 (1993).

18 Quiocho, F. A., Ledvina, P. S., *Mol. Microbiol.*, **20**, 17 (1996).

19 Neilands, J. B., *J. Biol. Chem.*, **270**, 26723 (1995).

20 Braun, V. *FEMS Microbiol. Rev.*, **16**, 295 (1995).

21 Braun, V., Hantke, K., Koster, W., *Met. Ions. Biol. Syst.*, **35**, 67 (1998).

22 Buchanan, S.K., Smith B.S., Venkatramani, L., Xia D., Esser, L., Palnitkar, M., Chakraborty, R., van der Helm, D., Deisenhofer, J., *Nat. Struct. Biol.*, **6**, 516 (1999).

23 Ferguson, A.D., Hofmann E., Coulton, J.W., Diederichs, K., Welte, W., *Science,* **282**, 2215 (1998).

24 Locher, K.P., Rees, B., Koebnik, R., Mitschler, A., Moulinier, L., Rosenbusch, J.P., Moras, D., *Cell,* **95**, 771 (1998).

25 Ferguson, A.D., Chakraborty, R., Smith, B.S., Esser, L., van der Helm, D., Deisenhofer, J., *Science*, **295,** 1715 (2002).

26 Supplemental material on *Science* Online at http://www.sciencemag.org/cgi/content/full/295/5560/1715/DC1.

27 Killmann, H., Herrmann, C., Wolff, H., Braun, V., *J. Bacteriol.*, **180**, 3845 (1998).

28 Härle, C., Kim, I., Angerer, A., Braun, V., *EMBO J.,* **14**, 1430 (1995).

29 Angerer, A., Enz, S., Ochs, M., Braun, V., *Mol. Microbiol.,* **18**, 163 (1995)

30 Newton, S.M., Allen, J.S., Cao, Z., Qi, Z., Jiang, X., Sprencel, C., Igo, J.D., Foster, S.B., Payne, M.A., Klebba, P.E., *Proc. Natl. Acad. Sci. USA,* **94,** 4560, (1997).

31 Cadieux, N., and Kadner, R. J., *Proc. Natl. Acad. Sci. U.S.A.* **96**, 10673 (1999).

32 Cadieux, N., Bradbeer, C., Kadner, R. J., *J. Bacteriol.* **182**, 5954 (2000).

33 Moeck, G. S. and Letellier, L., *J. Bacteriol.* **183**, 2755 (2001).

34 Moeck, G. S., Coulton, J. W., Postle, K., *J. Biol. Chem.* **272**, 28391 (1997).

35 Braun, M., Killmann, H., Braun, V., *Mol. Microbiol.* **33**, 1037 (1999).

36 Larsen, R. A., Thomas, M. G., Postle, K., *Mol. Microbiol.* **31**, 1809 (1999).

37 Cope, L., Thomas, S., Hrkal, Z., and Hansen, E., *Infect. Immun.*, **66**, 4511 (1998).

38 Létoffé, S., Ghigo, J.M., and Wandersman, C., *J. Bacteriol.* **176**, 5372 (1994).

39 Léoffé, S., Deniau, C., Wolff, N., Dassa, E., Delepelaire, P., Lecroisey, A., Wandersman, C., *Mol. Microbiol.,* **41**, 439 (2001).

40 Ghigo, J.M., Létoffé, S., and Wandersman, C., *J. Bacteriol.* **179**, 3572 (1997).

41 Izadi, N., Henry, Y., Haladjian, J., Goldberg, M.E., Wandersman, C., Delepierre, M., and Lecroisey, A., *Biochemistry* **36**, 7050 (1997).

42 Ghigo, J.M., Letoffe, S., Wandersman, C., *J. Bacteriol.,* **179**, 3572, (1997).

43 Arnoux, P., Haser, R., Izadi, N., Lecroisey, A., Delepierre, M., Wandersman, C., and Czjzek, M., *Nature Struct. Biol.* **6**, 516 (1999).

44 Das, T.K., Couture, M., Lee, H. C., Peisach, J., Rousseau, D.L., Wittenberg, B.A., Wittenberg, J. B., Guertin, M., *Biochemistry* **38**, 15360 (1999).

45 Maurus, R., Bogumil, R., Luo, Y., Tang, H.L., Smith, M., Mauk, A.G., and Brayer, G.D. *J. Biol. Chem.,* **269**, 12606 (1994).

46 Cornelissen, C. N., and Sparling, P. F., *J. Bacteriol.* **178**, 1437 (1996).

47 Legrain, M., Mazarin, V., Irwin, S. W., Bouchon, B., Quentin-Millet, M.-J., Jacobs, E., and Schryvers, A. B., *Gene* (*Amst.*) **130**, 73 (1993).

48 Locher, K. P., Rees, B., Koebnik, R., Mitschler, L., Moulinier, A., Rosenbusch, J. P., and Moras, D., *Cell,* **95**, 771 (1998).

49 Schryvers, A. B., and Stojiljkovic, I., *Mol. Microbiol.* **32**, 1117 (1999).

50 Cornelissen, C. N., and Sparling, P. F., *Mol. Microbiol.* **14**, 843 (1994).

51 Gray-Owen, S. D., and Schryvers, A. B., *Trends Microbiol.* **4**, 185 (1996).

52 Rokbi, B., Mazarin, V., Maitre-Wilmotte, G., and Quentin-Millet, M.-J., *FEMS Microbiol. Lett.* **110**, 51 (1993).

53 Krell, T., Renauld-Mongenie, G., Nicolai, M-C., Fraysse, S., Chevalier, M., Berard, Y., Oakhill, J., Evans, W., Gorringe, A., Lissolo, L., *J Biol. Chem.* **278**, 14712 (2003).

54 Boulton, I. C., Gorringe, A. R., Allison, N., Robinson, A., Gorinsky, B., Joannou, C. L., and Evans, R. W., *Biochem. J.* **334**, 269 (1998).

55 Nikaido, H., Saier, M. H., Jr. *Science*, **258**, 936 (1992).

56 Mao, B., Pear, M.R., McCammon, J.A., Quiocho, F.A. *J. Biol. Chem.*, **257**, 1131 (1982).

57 Ames, G.F. *Annu. Rev. Biochem.*, **55**, 397 (1986).

58 Bruns, C.M., Nowalk, A.J., Arvai, A.S., McTigue, M.A., Vaughan, K.G., Mietzner, T.A., McRee, D.E. *Nat. Struct. Biol.*, **4**, 919 (1997).

59 Boos, W., Lucht, J.M. *Escherichia coli and Salmonella typhimurium*, ASM Press Washington (1996).

60 Gasdaska, J.R., Law, J.H., Bender, C.J. and Aisen, P., *J. Inorg. Biochem.*, **64**, 247 (1996).

61 Jandl, J.H., Inman, J.K., Simmons, R.L., and Allen, D.W., *J. Clin. Invest.*, **38**, 161 (1959).

62 Thibodeau, S.N., Lee, D.C., and Palmiter, R.D., *J. Biol. Chem.* **253**, 3771 (1978).

63 Williams, S.C. and Woodworth, R.C., *J. Biol. Chem.*, **248**, 5845 (1973).

64 Arnold, R.R., Cole, M.F., and McGhee, J.R., *Science,* **197** 263 (1977).

65 Singh, T.P., Sharma, S., Karthikeyan, S., Betzel, C., and Bhatia, K.L., *Proteins. Struct. Funct. Genet.* **33**, 30 (1998).

66 He, J., and Furmanski, P., *Nature,* **373,** 721 (1995).

67 Hall, D.R., Hadden, J.M., Leonard, G.A., Bailey, S., Neu, M., Winn, M., Lindley, P.F., *Acta Cryst.* **D58**, 70 (2002).

68 Baker, E.N., and Lindley, P.F., *J. Inorg. Biochem.*, **47**, 147 (1992).

69 Aisen, P., leibman, A., and Zweier, J., *J. Biol. Chem.*, **253**, 1930 (1978).

70 Grossmann, J.G., Neu, M., Evans, R.W., Lindley, P.F., Appel, H., and Hasnain, S.S., *J. Mol. Biol.*, **229**, 585 (1993).

71 Schlabach, M.R., and Bates, G.W., *J. Biol. Chem.*, **250**, 2182 (1975).

72 Bailey, S., Evans, R. W., Garratt, R. C., Gorinsky, B., Hasnain, S., Horsburgh, C., Jhoti, H., Lindley, P. F., Mydin, A., Sarra, R. & Watson, J. L., *Biochemistry*, **27**, 5804 (1988)

73 Sarra, R., Garratt, R., Gorinsky, B., Jhoti, H. & Lindley, P., *Acta Cryst.* B**46**, 763 (1990).

74 MacGillivray, R. T. A., Moore, S. A., Chen, J., Anderson, B. F., Baker, H., Luo, Y., Bewley, M., Smith, C. A., Murphy, M. E. P., Wang, Y., Mason, A. B., Woodworth, R. C., Brayer, J. D. & Baker, E. N., *Biochemistry*, **37**, 7919 (1998).

75 Jeffrey, P. D., Bewley, M. C., MacGillivray, R. T. A., Mason, A. B., Woodworth, R. C. & Baker, E. N., *Biochemistry*, **37**, 13978 (1998).

76 Bewley, M. C., Tam, B. M., Grewal, J., He, S., Shewry, S., Murphy, M. E P., Mason, A. B., Woodworth, R. C., Baker, E. N. & MacGillivray, R. T. A., *Biochemistry*, **38**, 2535 (1999).

77 Nurizzo, D., Baker, H. M., He, Q.-Y., MacGillivray, R. T. A., Mason, A. B., Woodworth, R. C. & Baker, E. N., *Biochemistry*, **40**, 1616 (2001).

78 Zuccola, H. J., *PhD thesis*, Georgia Institute of Technology, Atlanta, Georgia, USA (1993).

79 Protein Data Bank, http://www.rcsb.org

80 Grootveld, M., Bell, J.D., Halliwell, B., Aruoma, O.I., Bomford, A., and Sadler, P.J., *J. Biol. Chem.*, **264**, 4417 (1989).

81 Hershko, C., Graham, G., Bates, G.W., and Rachmilewitz, E.A., *Br. J. Haematol.*, **40**, 255 (1978).

82 Lentz, D.J., Henderson, G.H., and Eyring, E.M., *Mol. Pharmacol.*, **9**, 514 (1973).

83 Jin, Y, Crichton, R. R.. *FEBS Lett.* **215**, 41 (1987).

84 Aisen, P., in *Iron Carriers and Iron Proteins* (ed. Loehr, T.M.), VCH, New York (1989).

85 Gray-Owen, S.D., and Schryvers, A.B., *Microb. Pathog.*, **14**, 389 (1993).

86 Alcantara, J., Yu, R.H., and Schryvers, A.B., *Mol. Microbiol.*, **8**, 1135 (1993).

87 Crosa, J.H., *Annu. Rev. Microbiol.*, **38**, 69 (1984).

88 Weinberg, E.D., *Physiol. Rev.*, **64**, 65 (1984).

89 Mietzner, T.A., Tenza, S.B., Adhikari P., Vaughan K.G., Nowalk AJ., *Curr. Topics Microbiol. Immunol.*, **225**, 113 (1998).

90 Adhikari, P., Kirby S.D., Nowalk A.J., Veraldi K.L., Schryvers A.B., Mietzner T.A., *J. Biol. Chem.*, **270**, 25142 (1995).

91 Aisen, P., in *Met. Ions. Biol. Syst.* **V35**, (eds. Sigel, A. and Sigel, H.), Marcel Dekker, New York, p585 (1998).

92 Butler, A., *Nat. Struct. Biol.*, **10**, 240 (2003).

93 Nowalk, A. J., Vaughan, K.G., Day, B.W., Tencza, S.B., Mietzner, T.A., *Biochemistry* **36**, 13054 (1997).

94 Berish, S. A., Mietzner, T. A., Mayer L.W., Genco C.A., Holloway BP., Morse SA., *J. Exp. Med.* **171**, 1535 (1990).

95 Berish, S. A.; Chen, C.-Y.; Mietzner, T.A.; Morse, S.A., *Mol. Microbiol.* **6**, 2607 (1992).

96 Nowalk, A. J.; Tencza, S. B.; Mietzner T.A., *Biochemistry*, **33**, 12769 (1994).

97 Chen, C.-Y., Berish., S. A., Morse S.A., Mietzner T.A., *Mol. Microbiol.*, **10**, 311 (1993).

98 Mcree, D. E., Bruns, C. M., Williams, P. A., Mietzner, T. A., Nunn, R., Protein Data Bank (1d9y), http://www.rcsb.org.

99 Mietzner, T. A., and Morse, S.A., *Annu. Rev. Nutr.*, **14**, 471, (1994).

100 Mietzner, T.A., and Cohen, M., in The Molecular Approach to New and Improved Vaccines (Levine, M. M., Kaper, J., et al., Eds.) p 817, Marcel Dekker, Inc., New York (1996).

101 Bruns, C.M., Anderson, D.S., Vaughan, K.G., Williams, P.A., Nowalk, A.J., McRee, D.E., Mietzner, T.A., *Biochemistry* **40**, 15631 (2001).

102 Cornelissen, C.N., and Sparling, P.F., *Mol. Microbiol.*, **14**, 843 (1994).

103 Adhikari, P., Berish, S.A., Nowalk, A.J., Veraldi, K. L., Morse, S.A., and Mietzner, T.A., *J. Bacteriol.*, **178**, 2145 (1996).

104 Andrews, S.C., *Adv. Microbiol. Physiol.*, **40**, 281 (1998).

105 Welch, S. in *Transferrin: The Iron Carrier* (Welch, S., Ed.), 1 CRC Press, Boca Raton, FL. (1992).

106 Mietzner, T. A., & Morse, S. A., in *The pathogenic Neisseriae* (Schoollink, G. K., Brooks, G. F., Falkow, S., Knapp, J.S., McCutchan, A., & Morse, S. A., Eds.) 406 American Society for Microbiology, Washington, D.C. (1985).

107 Guo, M. *PhD Thesis*, University of Edinburgh (2000).

Chapter 2 Materials and General Experimental Methods

2.1 General Reagents

All chemicals and solvents were purchased from Sigma-Aldrich, Fisher, Acros, Pharmacia, Promega, Bio-Rad or Invitrogen unless specified in later chapters.

2.2 Solutions and Buffers

Ampicillin: a stock solution (100 mg/ml) was made and filtered by 0.2 μm filter. A final concentration of 100 μg/ml was used in various media. The stock solution was stored at 4°C.

Ethidium Bromide: a stock solution (10 mg/ml) was made and used at a final concentration of 5 μg/ml. The stock solution was stored in a dark bottle at 4°C.

SDS running buffer: Tris-HCl (25 mM, pH 8.3), glycine (192 mM), SDS (1% w/v).

SDS sample buffer: Tris-HCl (0.5 M, pH 6.8, 1.0 ml), glycol (2.0 ml), SDS (10% w/v, 1.6 ml), 2-β-mercaptoethanol (0.4 ml), bromophenol blue (0.05%, w/v, 2.0 ml).

TAE (Tris-Acetate-EDTA) buffer: The 50 x stock TAE buffer was obtained from Bio-Rad. After being diluted with deionised water, the TAE buffer (1 x) contains Tris-HCl (40 mM), acetic acid (20 mM), EDTA (1M), pH 8.3.

Physiological buffer – 100 mM NaCl, 4 mM NaH_2PO_4 and 25 mM $NaHCO_3$, dissolved in water and adjusted to pH 7.4.

2.3 Media

Agar plates: bacto-agar (15 g/l) was added to specified media with appropriate antibiotic to prepare agar plates.

Luria Bertani (LB): bacto-tryptone (10 g), bacto-yeast extract (5 g), sodium chloride (10 g) were dissolved in 1 litre of deionised water and then the pH was adjusted to 7.5 using sodium hydroxide.

S-Gal/LB/amp plate: a pack of S-Gal™/LB Agar Blend (Sigma C-4478) was dissolved in 500 ml water and autoclaved, then ampicillin was added to the solution to prepare plates.

SOC: bacto-tryptone (20 g), bacto-yeast extract (5 g), sodium chloride (0.5 g), magnesium chloride (5 g), and glucose (3.2 g) were dissolved in 1 litre of deionised water and then the pH adjusted to 7.5 using sodium hydroxide.

2YT (2 x YT medium): bacto-tryptone (16 g), bacto-yeast extract (10 g), and sodium chloride (5 g) were dissolved in 1 litre of deionised water and then the pH was adjusted to 7.5 using sodium hydroxide.

2.4 Bacterial Cell Lines

Escherichia coli TOP10™ (Invitrogen) cell lines were used for the storage of genes, for the initial transformation of ligation products, and also for overexpressing proteins.

2.5 Storage of Bacterial Stocks

LB or 2YT medium containing the appropriate antibiotics were used for the short-term storage of *E. coli.* Colonies of bacteria were stored on inverted parafilm sealed agar plates at 4 °C for up to one month. For long-term storage, strains were frozen at –80 °C in LB or 2YT media containing 15% glycerol.

2.6 Overexpression of FBP in *E. coli*

2.6.1 DNA Plasmid of Wild-Type FBP

The plasmid pTrc99A containing the gene for FBP from *Neisseria gonorrhoeae* (pTrc99A/FBP_NG) was supplied by Professor R.T.A. MacGillivray (University of British Columbia, Vancouver, Canada).

2.6.2 Transformation of *E. coli* Competent Cells with Recombinant DNA

The competent cells were gently suspended by tapping and 25 μl of the suspension was transferred to a sterilised Eppendorf tube. It was left on ice for 30 minutes and the expressing plasmids (pTrc99A/FBP/NG) were added (up to 40 ng). Then, the cells were heat-shocked at 42 °C for 30 seconds, and then left to sit on ice for 2 minutes. After that, 250 μl SOC was added. The mixture was incubated by shaking at 250 rpm at 37 °C for 1 hour. Then, the suspension (30 μl) was spread to dryness on selective agar plates and incubated at 37 °C for 16 hours.

2.6.3 Small Scale Preparation of FBP from *E. coli*

A single colony from a freshly-transformed agar plate was transferred for growing in 10 ml of 2YT containing 100 μg/ml ampicillin at 37 °C for 16 hours. The cells were harvested by centrifugation at 3,000 rpm at 4 °C for 15 minutes. The best-expressed cells (the darkest pink colour) were picked out for large scale preparation of FBP.

2.6.4 Large Scale Preparation of FBP from *E. coli*

The cells from a small scale preparation were re-suspended with 2YT solution and each 1 ml of re-suspended solution was transferred to 250 ml LB containing 100 μg/ml ampicillin. The mixture was incubated by shaking at 37 °C for 18 hours. The cells were harvested by centrifugation at 10,000 rpm for 15 minutes. The pink wild-type FBP pellet was collected and frozen at –20 °C for further protein extraction and purification.

2.6.5 Wide-type FBP Purification

Wild-type FBP was purified by a slight modification of methods described previously [1,2]. The pellet from the large scale preparation (*ca.* 5 g) was defrosted at room temperature and was re-suspended in 50 ml of 1 M Tris (pH 8.0) and 50 ml 2% CTAB (Cetyltrimethylammonium Bromide, Aldrich, Cat. No. 85582-0). EDTA-free anti-protease tablets (Complete®, Roche, Cat. No. 1873580) were added followed by stirring gently for 6 hours at 37 °C. The white insoluble materials were removed by centrifugation at 10,000 rpm at 4 °C for 15 minutes. The supernatant was diluted by deionised water to a final volume of 1 litre and incubated at 4 °C for over 16 hours. Any insoluble material was removed by centrifugation (10,000 rpm, 4 °C, 15 minutes), followed by ultrafiltration with a 0.45 μm membrane. A RESOURCE®S column (6 ml, Pharmacia) was washed according to the manufacturer's instruction and equilibrated with 10 mM Tris buffer (pH 8.0, buffer A). The CTAB extract was centrifuged at 10,000 rpm for 15 minutes at 4 °C and filtered through a 0.45 μm membrane, and then loaded onto the column by FPLC (Pharmacia) and the protein was eluted with a NaCl gradient from low to high salt concentration (0-1 M) using a 10 mM Tris, 1 M NaCl buffer (pH 8.0, buffer B). Parameters of the loading method and elution method are listed in **Table 2.1**. Fractions (4 ml) were collected and analysed by SDS-PAGE. FBP-containing fractions were pooled and concentrated by ultrafiltration (Amicon concentrator 30, 30 kDa cut-off) and purified on a HiLoad Superdex 200 column (26/60, Pharmacia) by elution with 10 mM Tris, 100 mM NaCl buffer, pH 8.0.

Table 2.1 FPLC methods for FBP purification using a RESOURCE®S column (6 ml)

Loading Method			**Eluent Method**		
Volume (ml)	Parameter	Value	Volume (ml)	Parameter	Value
0.00	CONC %B	0.0	0.00	CONC %B	0.0
0.00	ML/MIN	4.00	0.00	ML/MIN	4.00
0.00	PORT.SET	6.0	0.00	PORT.SET	6.1
0.00	VALVE.POS	1.1	0.00	VALVE.POS	1.1
250.0	CONC %B	0.0	90.0	CONC %B	0.0
			210.0	CONC %B	100
			240.0	CONC %B	100
			240.0	CONC %B	0.0
			270.0	CONC %B	0.0

2.7 *apo*-Fbp Preparation

Apo-Fbp was prepared by a modification of a published method [3]. Ten volumes of 0.25 M citric acid solution (pH 4.5) were added to the *holo*-Fbp solution. This was kept at room temperature for half an hour, and then loaded on to a PD-10 column (Pharmacia). The protein was eluted with 0.25 M citric acid buffer (pH 4.50). Then the buffer was changed from 0.25 M citric acid to 10 mM ammonium acetate using a PD-10 column, followed by dialysis of the collected fraction against 10 mM ammonium acetate (5 litres), three times (10 hours each time). Finally, the protein solution was treated by Chelex® 100 resin to remove any trace metal, followed by lyophilisation. The *apo*-FBP powder was stored at –20 °C.

2.8 Protein Crystallisation

Proteins consist of long macromolecule chains made up from 20 different amino acids. The chains can be several hundred residues long and fold into a 3-dimensional structure. It is therefore quite understandable that protein molecules have irregular shapes and are not ideally suited to be stacked into a periodic lattice, i.e., a crystal. Protein crystals are thus very fragile, soft and sensitive to all kinds of environmental variations. Protein crystals contain on average of 50% solvent, mostly in large channels between the stacked molecules in the crystal. The interactions holding the molecules together are usually weak, hydrogen bonds, salt bridges, and hydrophobic interactions, compared to strong covalent or ionic interactions in mineral crystals. This explains the fragility of the crystals, but allows for the possibility of soaking metal solutions or even large enzyme substrates or inhibitors, into the crystals [4].

In order to obtain a crystal, the protein molecules must assemble into a periodic lattice. To a solution of the protein with a fairly high concentration (2-50 mg/ml), reagents are added that reduce the solubility close to spontaneous precipitation. By slow further concentration, and under conditions suitable for the formation of a few nucleation sites, small crystals may start to grow. Often very many conditions have to be tried to succeed. This is usually done by initial screening, followed by a systematic optimisation of conditions. Crystals should be a few tenth of a mm in each direction to be useful for diffraction experiments [4].

The most common setup to grow protein crystals is the hanging drop technique. A few microliters of protein solution are mixed with an equal amount of reservoir solution containing the precipitants. A drop of this mixture is put on a glass slide which covers the reservoir. As the protein/precipitant mixture in the drop is less concentrated than the reservoir solution, water evaporates from the drop into the reservoir. As a result the concentration of both protein and precipitant in the drop slowly increases, and crystals may form. There is a variety of other techniques available such as sitting drops, dialysis buttons, and gel and microbatch techniques.

Robots are useful for automatic screening and optimisation of crystallisation conditions [4].

The hanging drop vapor-diffusion method was used for protein crystallisation in this project. Purified and concentrated protein (~ 350 μM) and precipitant solutions (various concentrations of PEG 1450 and PEG 4000), 0.1 - 0.2 M KCl, 0.4 M malate/imidazole or imidazole/HCl buffer, pH 6.5 – 8.0. The drop (10 μl) of protein solution and precipitant solution (1 : 1, v/v) was placed on a siliconised cover slip (BDH, Cat. 406/0189/44) and placed upside down over a wax-coated well lip. The crystal was grown at 4 °C or 17 °C. In some cases, seeding was used to grow better crystals. Normally, a crystal suitable for X-ray diffraction was obtained two weeks after setting up the drop.

2.9 Instruments

2.9.1 UV-Vis Spectroscopy

The UV/Vis spectrophotometers used in this project were Perkin Elmer Lambda 16, Perkin Elmer Lambda 20, Shimadzu UV-2501PC and Varian Cary 300 equipped with temperature control systems. 1 cm quartz cuvettes were used with 500 μl working volume. Normally, only solvent was used as reference.

A common application of UV-Vis spectroscopy is the determination of the concentration of a substance in solution if the extinction coefficient is known and the Beer-Lambert law is obeyed. Proteins and nucleic acids have characteristic absorbances at 280 nm and 260 nm [5]. Their concentrations can be determined from absorbance (A) at these wavelengths and the Beer-Lambert law ($c = A_{280}/\epsilon b$, c is the protein concentration, ϵ is the molar extinction coefficient at 280 nm [$M^{-1}cm^{-1}$], b is the path length [cm]).

For protein samples with known amino acid components, ϵ can be roughly calculated using the number of Trp(N_{Trp}) and Tyr(N_{Tyr}) residues and disufide bonds ($N_{s\text{-}s}$) in the protein as follows [6]: $\epsilon_{280} = 5540N_{Trp} + 1480N_{Tyr} + 134N_{s\text{-}s}$

2.9.2 ICP-AES

ICP-AES stands for inductively coupled plasma atomic emission spectrometry. The plasma is formed by argon gas flowing through a radiofrequency field where it is kept in a state of partial ionisation, i.e. the gas consists partly of electrically charged particles. This allows it to reach very high temperatures of up to approx. 10,000 °C. A plasma is an electrically neutral, partially ionised gas composed of ions, electrons and neutral species (atoms and molecules) of an inert gas which is maintained by an external field, and has sufficiently high temperature to atomise, ionise and excite most elements. A variety of inert gases such as argon, helium and nitrogen can be used to form analytically useful plasmas. Typically quoted plasma temperatures range from 7,000 to 10,000 K. At high temperature, most elements emit light of characteristic wavelengths which can be measured and used to determine their concentrations [7].

The sample is introduced into the plasma as a fine droplet aerosol. Light from the different elements is separated into different wavelengths by means of a grating and is captured by light-sensitive detectors, one for each element being analysed. This permits simultaneous analysis of up to 40 elements and ICP-AES is consequently a multi-element technique. ICP-AES generally gives significantly improved limits of detection for most elements. Detection limits are typically at the μg/l (ppm) level for aqueous solutions.

All ICP-AES analyses in this project were carried out on a Thermo Jarrell Ash IRIS instrument. The R. F. power was 1150 watts, the nebulizer flow was 30 psi, the pump rate was 100 rpm and the purge time was 90 s. Commercially available atomic absorption standard solutions of hafnium (BDH), iron (Aldrich), phosphate (Aldrich) and sulphur (Aldrich) were diluted and used as standards. The protein samples were measured without the digestion of samples. The standard concentration unit in ICP-AES is ppm. The element codes, the slope of the standard line, and Y-int (the intercept of the standard line or zero-concentration) are listed in **Table 2-2**.

Typically, five standards were used, and the correlation coefficients was better than 99.8%.

Table 2-2 The emission lines used for ICP-AES analysis

Element code	Wavelength (nm)	Slope	Y-int
Hf 3399	339.980 (76)	24.02	0.3007
Fe 2395	239.562(108)	27.82	0.5705
P 2149	214.914 (121)	1.337	0.4920
S 1820	182.034 (142)	0.7936	0.0341

2.9.3 Nuclear Magnetic Resonance Spectroscopy

Basic theory and concepts of NMR are given in various textbooks, such as Friebolin [8] and Mason [9]. The nuclei used in this project and their magnetic properties are given in **Table 2.3**.

Table 2.3 Magnetic properties [10] of nuclei used in this project

Nuclei	^{31}P	^{51}V
Nuclear Spin (I)	1/2	7/2
Frequency (MHz) at 11.74 T	202.4	131.5
Natural Abundance (%)	100	99.75
Magnetogyric Ratio γ (10^7 rad T^{-1} s^{-1})	10.83	7.05
Nuclear quadrupole moment, Q (barn)	-	-0.052

In this project, the NMR instrument used was a Bruker DMX 500. All NMR spectra were recorded at 310 K. The solvent for protein samples was H_2O/ D_2O (90% : 10%, v/v). Phosphoric acid (0 ppm) sealed in a capillary was used as external standard for

^{31}P NMR, $VOCl_3$ (0 ppm), also sealed in a capillary, was used as external standard for ^{51}V NMR. D_2O (10%) was used for locking. The probe used for ^{31}P NMR was a 5 mm triple-resonance probehead in multinuclear version TBI probe (^{1}H, ^{31}P, Broad Band), and the probe used for ^{51}V NMR was a 5 mm BBO probe (Broad Band probe in the low frequency).

2.9.4 Electron Paramagnetic Resonance Spectroscopy

In electron paramagnetic resonance (EPR), also called electron spin resonance (ESR), electromagnetic radiation (usually of microwave frequency) is absorbed by molecules, ions, or atoms possessing electrons with unpaired spins, *i.e.* electronic spin $S > 0$. The sample material is immersed in a strong static magnetic field and exposed to an orthogonal low- amplitude high-frequency field. EPR usually requires microwave-frequency radiation (GHz). Energy is absorbed by the sample when the frequency of the radiation is appropriate to the energy difference between two states of the electrons in the sample, but only if the transition satisfies the appropriate selection rules. More details of the theory of EPR can be found in textbooks of Slicher [11] or Weil [12]. A Bruker ER 200D-SRC spectrometer (X-band) was used to record EPR spectra at 120 K using a liquid nitrogen insert Dewar and standard rectangular cavity.

2.9.5 Crystallographic Data Collection and Structure Analysis

X-ray crystallography is a technique that exploits the fact that X-rays are diffracted by crystals. It is not an imaging technique. X-rays have the proper wavelength (in the Ångström range, $\sim 10^{-8}$ cm) to be scattered by the electron cloud of an atom of comparable size. Based on the diffraction pattern obtained from X-ray scattering by the periodic assembly of molecules or atoms in the crystal, the electron density can be reconstructed. Additional phase information must be extracted either from the diffraction data or by supplementing diffraction experiments to complete the reconstruction (the phase problem in crystallography). A model is then progressively

built into the experimental electron density, refined against the data and the result is an accurate molecular structure [13].

To perform an X-ray diffraction experiment, an X-ray source is needed. In most cases a rotating anode generator producing an X-ray beam of a characteristic wavelength is used. Intense, tunable X-ray radiation produced by a Synchrotron provides additional advantages. The primary X-ray beam is monochromated by either crystal monochromators or focusing mirrors. After the beam passes through a helium-flushed collimator, it passes through the crystal mounted on a pin on a goniometer head. The head is mounted to a goniometer which allows the crystal to be positioned at different orientations in the beam. The diffracted X-rays are recorded using image plates, multiwire detectors or CCD cameras (**Figure 2.1**).

Flash cooling protein crystals to cryogenic temperatures (~100 K) offers many advantages, the most significant of which is the elimination of radiation damage. A part of the X-rays passing through the crystal are scattered in different directions into a detector. In our facility, multiwire detectors and CCD detectors were used. They all deliver an image of the diffraction spots. A large number of these images recorded from different crystal orientations are processed (scaled and merged) into a final list of indexed reflection intensities.

Data for the protein crystals were collected and processed by Dr. Dmitriy Alexeev on DL 9.6 (SRS at Daresbury laboratory), the wavelength for data collection was 0.87 Å. For in-house data collection, a Enraf-Nonius FR591with MAR 345 Image Plate Detector was used. The wavelength for data collection was 1.54 Å (K_α radiation of copper). All data were collected at 100 K.

Data for the small hafnium complex [$Na_2Hf(NTA)_2 \cdot H_2O$] were collected by Dr. S. Parsons on a Bruker SMART ADEX CCD area detector diffractometer using graphite monochromated Mo K_α radiation ($\lambda = 0.71073$ Å).

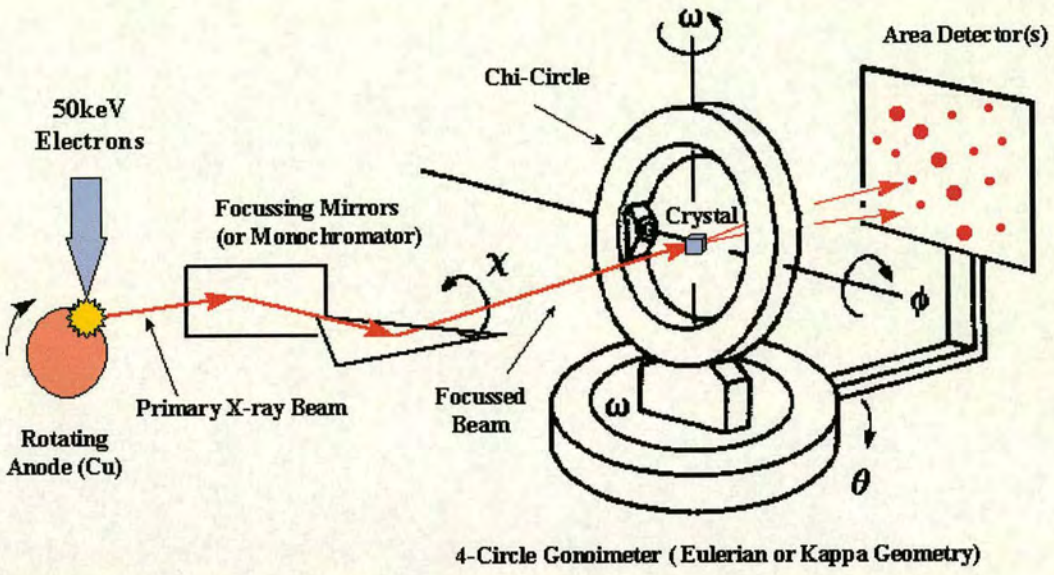

Figure 2.1 Working principle of X-ray diffraction equipment [4].

References

1 Berish S.A., Chen C.Y., Mietzner T.A., Morse S.A., *Mol. Microbiol.*, **6,** 2607-2615 (1992).

2 Guo M.L., *PhD Thesis*, University of Edinburgh, 221-222, (2000).

3 Taboy, C. H.; Vaughan, K. G.; Mietzner T.A.; Aisen P; Crumbliss A.L., *J. Biol. Chem.* **276**, 2719-2724, (2001).

4 http://www-structure.llnl.gov/Xray/101index.html

5 Robyt, John F., *Biochemical Techniques*, Sue Ewing Ed.; Brooks/Cole, California, p52, (1987).

6 Mach H., Middaugh C.R., Lewis R.V., *Anal. Biochem.*, **200,** 74-80, (1992).

7 http://www.sgab.com (2001).

8 Friebolin, H., *Basic One- and Two-dimensional NMR spectroscopy* 3rd rev. ed. WILEY-VCH, Weinheim ; Chichester, (1998).

9 Mason J, Ed., *Multinuclear NMR*, Plenum Press, New York, (1987).

10 http://www.webelements.com (1993-2003).

11 Slichter, C. P., *Principles of Magnetic Resonance (CLAS)*, **3rd ed.**, p. 65 Springer-Verlag (1992) and Harper & Row, (1963).

12 Weil, J.A., *Electron Paramagnetic Resonance : Elementary Theory and Practical Applications* New York ; Chichester : Wiley (1994).

13 Rhodes, G. *Crystallography Made Crystal Clear*, **2nd ed.** Academic Press, San Diego, (2000).

Chapter 3 *Apo*-FBP and Reloaded Fe-FBP

3.1 Introduction

3.1.1 Iron in Biological Systems

Iron is the fourth most abundant element in the earth's crust, the second most abundant metal besides aluminium [1]. The value of iron to biological systems is largely due to its incomplete filled orbitals giving two relatively stable oxidation states, namely iron(II) (d^6) and iron(III) (d^5), which provide a considerable range of reactivity for iron. The redox potential between these two states is such that oxidation processes centred on the iron can be coupled to metabolic reactions. Both ferrous and ferric forms can form salts with common anions. When bound to appropriate organic ligands, the reactivity of iron can be manipulated, allowing it to catalyse a wide range of chemical reactions essential to the cell. Iron is also the active component of the oxygen-carrier proteins. The necessity of sufficient iron for microbial metabolism is reflected by the almost universal requirement for the metal; only members of the *genus Lactobacillus* have replaced iron with other cofactors [2].

Iron can have a dual role in the life of a cell both as a protector from oxidation damage and as a destroyer by promoting such damage. Both iron insufficiency (by depressing the oxidative defences) and iron excess (by promoting the Fenton reaction) render cells at risk to damage from oxy-radicals [3]. The adult human body contains about 4 g of iron (i.e. ~0.005% of body weight), of which about 3 g is in the form of haemoglobin, and this level is maintained by absorbing a mere 1 mg of iron per day-a remarkably economical utilization.

Many proteins contain iron. Iron is found in a variety of different chemical environments in biology. Iron-containing metalloproteins fall into three main structural groups: **A)** Iron-sulfur proteins; this group of proteins contains one or more iron atom ligated by sulfide and thiolato sulfur. These proteins fulfill a variety of functions ranging from electron transfer and transport with both redox and non-redox roles, such as succinate dehydrogenase, nitrogenase, and aconitase. The iron can

exist in either or both of the oxidation states, +2 or +3. **B)** Haem proteins. It was known that Fe(IV) can be found in some haem proteins. The haem group is a common motif in biological systems and consists of an iron atom co-ordinated in an approximately square planar fashion by the pyrrole nitrogens of the porphyrin ring with one or two further axial ligands. The spin and the redox state of the iron influences the function of haem proteins leading to further subdivisions. *I.* Oxygen carriers such as myoglobin and haemoglobin where the iron is in the +2 oxidation state and cycles between a high-spin state and a low-spin electronic configuration. *II.* Oxygen activators such as peroxidases, oxidases and cytochromes P450 where both high and low spin states and oxidation states from +2 to +6 may be important. *III.* Electron transfer proteins such as cytochromes a, b, and c where the low spin configurations of iron in the +2 and +3 oxidation states are important. **C)** Non-haem and non-Fe/S proteins (metalloenzymes); this type of protein includes superoxide dismutase, dioxygenases, oxygenase, lipoxygenases, and ribonucleotide reductase. Iron may exist in the +2 or +3 oxidation states or both. Some iron-containing proteins found in nature are listed in **Table 3.1** [4].

Iron is usually present in aqueous aerobic environments as insoluble ferric oxy-hydroxides FeO(OH) [5]. At pH values approaching neutral, the maximum solubility of iron(III) is limited to 10^{-18} M due to its K_{sp} value of 10^{-39} M^4 [6]. Thus ferric ions are quickly hydrolysed to insoluble polymeric hydroxides. In contrast iron(II) is readily soluble ($K_{sp}=10^{-17}$ M^3) corresponding to a maximum concentration close to 1 mM at pH 7. Although ferrous salts are quite stable in the solid state, they are readily oxidised to the ferric form in solution in the presence of oxygen. It is thus obvious that under physiological conditions, neither iron(II) nor iron(III) is likely to exist in aerobic aqueous solutions as the hexa-aqua ions, $[Fe(H_2O)_6]^{2+}$ and $[Fe(H_2O)_6]^{3+}$, to any appreciate extent. Only by the use of suitable ligands is it possible to keep iron(III) in aqueous solution under neutral and basic conditions. The low aqueous solubility of iron(III) at neutral pH has required the development of specialised methods for organisms to acquire the metal from their surroundings. Many micro-organisms have evolved specific iron(III) sequestering agents, named siderophores,

in order to maintain the iron(III) in soluble form so as to facilitate the acquisition of the exogenous metal [6].

Table 3.1 Naturally Occuring Iron Proteins [4]

Name	Donor atoms, Stereochemistry of Fe	Function	Source	Approx. Mol wt	No. of Fe atoms
		Haem proteins			
Haemoglobin	5 x *N* Square pyramidal	O_2 transport	Animals	64500	4
Myoglobin	5 x *N* Square pyramidal	O_2 storage	Animals	17000	1
Cytochromes	5 x *N* + *S* or O (Tyr) or N (His) Octahedral	Electron transfer	Bacteria, plants, animals	12400	4
		***NHIP* (non-haem iron proteins)**			
Transferrin	5 x O, 1 x N	Transport of Fe	Animals	80000	2
Ferritin	FeO(OH) mineral	Storage of Fe	Animals	460000	20% Fe
Ferredoxins	4 x *S* Distorted tetrahedral	Electron transfer	Bacteria, plants	6000-12000	2-8
Rubredoxin	4 x *S* Distorted tetrahedral	Nitrogen fixation	Bacteria	6000	1
"MoFe protein"	4 x *S* Distorted tetrahedral	Nitrogen fixation	In nitrogenase	220000-230000	24-36
"Fe protein"	4 x *S* Distorted tetrahedral	Nitrogen fixation	In nitrogenase	50000-70000	4

Siderophores are low molecular weight compounds which can chelate ferric ion with high affinity. They can solubilise iron from insoluble complexes of the metal and form six-coordinated octahedral complexes with ferric ions [7, 8]. The bacteria then acquire the iron through outer membrane receptor protein complexes. However, not all bacteria use a siderophore-mediated uptake process, including possibly *Neisseria* [9]. Gram-negative pathogenic bacteria acquire iron from the host's lactoferrin and transferrin proteins by expressing receptors for these proteins (TbpA, TbpB, LbpA, LbpB) on their cell surface. Once the iron is deposited in the periplasmic space, *Neisseria gonorrhoea* and many other bacteria use FBP to facilitate transport of iron presented at the outer membrane across the periplasm to the cytoplasmic membrane.

3.1.2 Conformational Differences Between *apo*-hFBP and *holo*-hFBP

FBP is composed of two domains, with the iron-binding site occurring in a small cleft between the domains. The binding of Fe(III) by FBP is necessarily reversible, this means that FBP must be able to bind and donate iron and therefore exist in both metal-bound and metal-free conformations. The two domains of FBP move as rigid bodies about a hinge point located within the central β-sheet connecting them [10].

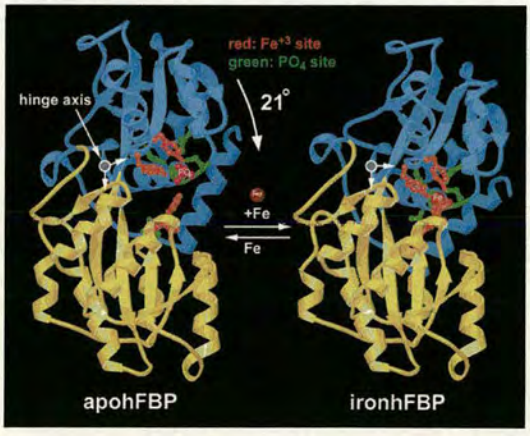

Figure 3.1 Conformational change between *apo*-hFBP and *holo-h*FBP [11].

Figure 3.1 shows that for FBP from *Haemophilus influenzae* (*h*FBP), comparison of the *apo*-hFBP structure with that of *holo*-hFBP reveals a distinct change in the orientation of the two structural domains. *Apo-h*FBP displays a 21° hinge movement

of the two domains relative to the iron-loaded form of the protein. The C-terminal iron half-site (top) retains the same structure in both the *apo* and iron forms, including the presence of a phosphate ion (pre-existing complementarity), while the N-terminal half-site reorganises upon iron binding (induced fit) [11].

3.1.3 Anion of Fe-FBP

As observed in the structure of *holo*-FBP, a monodentate tetrahedral phosphate is the synergistic anion of *holo*-FBP, although it has been found that a large excess of $NaHCO_3$ increases the iron binding capacity of *apo*-FBP [12]. In addition, many other anions can also bind to Fe-FBP. When iron was reloaded to *apo*-FBP, it was found that NTA (nitrilotriacetiate), oxalate, and pyrophosphate also appear to serve as synergistic anions, but not sulfate or perchlorate. In addition, phosphate in *holo*-FBP can be replaced by carbonate in the presence of a large excess of bicarbonate [13].

3.1.4 Summary of Studies in this Chapter

FBP can bind iron reversely. In order to understand the mechanism of iron loading and release, *apo*-FBP was prepared, and the mononuclear complexes $Na_3[Fe(NTA)_2]$ and binuclear complex $(Hpy)_2[Fe_2(cit)_2(H_2O)_2]$ were used to load iron into *apo*-FBP (from *Neisseria gonorrhoeae*). The reloaded Fe-FBP was characterised by ICP-AES, high-resolution chromatography and EPR. To investigate the function of residues which are involved in iron binding in *holo*-FBP, two mutant FBP proteins (E57H FBP and Y195H/Y196H FBP) were expressed and characterised. The possibility that Fe-FBP can cleave phosphoester bonds was also investigated. High-quality crystals of *apo*-FBP, mononuclear Fe-FBP and multinuclear Fe-FBP were prepared and the structures were investigated by X-ray crystallography.

3.2 Experimental Methods

Chemicals Ferric nitrate, $Fe(NO_3)\cdot 9H_2O$, (Prod. No. 28384), polyethylene glycol 4000 (Prod. No. 442734X), ammonia acetate (Prod. No. 10013) and tri-sodium citrate ($Na_3C_6H_5O_7\cdot 2H_2O$, Prod. No. 10242) were purchased from BDH. Nitrilotriacetic acid (Cat. No. N840-7), atomic absorption standard solution of Fe (Cat. No. 30595-2) and S (Cat. No. 33329-8), and bis(4-nitrophenyl) phosphate (BNPP) (Cat. No. 12394-3) were obtained from Aldrich. Imidazole (Cat. No. I-2399) was purchased from Sigma. Citric Acid (Cat. No. C/6240/53), sodium chloride and sodium hydroxide were purchased from Fisher. Polyethylene glycol 1450 (Cat. No. 41804-5000) was purchased from Acros.

Starting materials *Apo*-FBP was prepared as described in Chapter 2. $Na_3[Fe(NTA)_2]\cdot 5H_2O$ solution was prepared with Clegg's method [14]. Dinuclear Fe(III) complex $(Hpy)_2[Fe_2(cit)_2(H_2O)_2]\cdot 2H_2O$ was prepared with Shweky's method [15]. Both complexes were characterised by CHN analysis.

UV-Vis (Ultraviolet-Visible) spectroscopy UV-Vis experiments were performed with a Cary 300 UV-Vis spectrometry using 0.5 ml of sample in 1 cm quartz cuvettes with temperature control unit. The spectra in this chapter were recorded between 700 nm / 800nm and 220 nm.

Preparation of *holo*-Fe-FBP *Holo*-Fe-FBP (no phosphate bound) was prepared by using 50 mM Tris buffer (pH 8.0) to wash *holo*-Fe-P_i-FBP (with phosphate bound) with 30 kDa molecular weight cut off Centricon® (YM-30, Millipore) for three times.

Preparation of reloaded Fe-FBP Reloaded Fe-FBP was prepared by adding a 50-fold molar excess of iron(III). Either $Na_3[Fe(NTA)_2]$ or $(Hpy)_2[Fe_2(cit)_2(H_2O)_2]\cdot 2H_2O$ was added to an *apo*-FBP solution in 10 mM Tris, 100 mM NaCl, pH 8.0. The mixture was incubated in a 37 °C water bath for three hours, and low molecular weight impurities were removed using a PD-10 column

(Amersham), and then by ultrafiltration (Centricon®, 30 kDa cut off, YM-30, Millipore).

Phosphoester bond cleavage by Fe-FBP Reloaded Fe-FBP was prepared as described above. The compound BNPP was mixed with Fe-FBP in 10 mM Tris, 100 mM NaCl, pH 8.0 at 37 °C with 1:1 molar ratio. The reaction was monitored by UV-Vis spectra from 800 nm to 220 nm at 30 minute time intervals. To determine the rate constant, a 14-fold molar excess of BNPP was reacted with reloaded Fe-FBP in 50 mM Tris, 0.1 M $NaNO_3$, pH 8.0, at 37 °C. As control, a cuvette containing the same buffer and BNPP, but no reloaded Fe-FBP was used.

Fe-FBP and DNA interaction The interaction between Fe-FBP and DNA (pUC18, Invitrogen) was investigated by 1% agarose gel and 6% DNA retardation gel (EC63652, Invitrogen). Linear PUC18 DNA was prepared by cutting circular pUC18 plasmid DNA with NdeI and purified by 1% agarose gel. Linear DNA was incubated with various concentrations of Fe-FBP in 50 mM Hepes, pH 7.5 in a 37 °C water bath for 3-24 hours. The protein-DNA interaction was examined with both 1% agarose gels and 6% DNA retardation gels.

3.2.1 Site-Directed Mutagenesis of DNA

Molecular biology reagents Restriction enzyme NcoI, HindIII, NdeI and related buffers were purchased from New England BioLabs. TOPO TA cloning® kit was obtained from Invitrogen. DNA marker I and IV were purchased from Bioline. DNA sequencing kit (Big dye v3) was obtained from Biosystem.

Electrophoresis of DNA (1% agarose gel) Agarose (1.44 g) was added to 120 ml TAE buffer and heated in a microwave oven at 100 °C until it was dissolved. The solution was cooled to 60 °C and 7 μl ethidium bromide (10 mg/ml) was added to the agrose solution. The gel was then poured into the casting mould and allowed to set at room temperature.

Electrophoresis of proteins NuPAGE® Noves 12% Bis-Tris Gel (NP0342) and related buffers were purchased from Invitrogen.

Preparation and purification of plasmid DNA Plasmid DNA was prepared from cells as described in the QlAprep® Spin miniprep Kit protocol (QIAGEN). Plasmid DNA was purified with a 1% agarose gel and then extracted from the gel using the QlAquick® Gel Extraction Miniprep Kit protocol (QIAGEN).

The mutant gene for FBP/Y195HY196H was made by the PCR megaprimer method [16]. CACCAC were used as the mutant codons to change the TACTAC encoding Tyr-Tyr to His-His. Synthetic oligonucleotides were used as mutant primers for making the mutants. The mutagenic PCR reactions involve two PCR steps.

Plasmid and oligonucleotide primer Plasmid for mutant protein FBP_E57H was provided by Dr. Dominic J.B. Hunter. The primer for FBP_Y195HY196H was purchased from Sigma Genosys. The sequences are shown below.

FBP_HisHis	5'-ATCAACAACCACCACTGGCACGCT-3'
FBP_Ng_For	5'-CCATGGCAAAAACATCTATCCGATAC-3'
pTRC_His_Rev	5'-TGTCTAATTTAGTCTTGCGTCTTC-3'

Production of the Megaprimer (step 1) pTrc99A/FBP_NG (1 μl) was used as template, FBP_HisHis as reverse primer (5 μl) and FBP_Ng_For as forward primer (5 μl), then 39 μl H_2O was added to make the final volume to 50 μl. The solution was overlayed with PCR oil and cycled 30 times at 95 °C for 1 minute, 58 °C for 30 seconds, and 72 °C for 20 seconds. Finally, heating at 72 °C for 5 minutes to terminate the reaction. The PCR products were mixed with 5 μl blue loading dye and then applied on a 1% agarose gel and the band containing the target product was cut and purified.

Production of the Mutant FBP Gene (step 2) Megaprimer (15 μl) produced from step 1 was used as template, FBP_HisHis (1 μl) was used as reverse primer and FBP_Ng_For (5 μl) was used as forward primer, then 29 μl H_2O was added to make the final volume up to 50 μl. The solution was overlayed with two drops of PCR oil and cycled 30 times at 95 °C for 1 minute, 58 °C for 30 seconds, and 72 °C for 60 seconds. Finally, heating at 72 °C for 5 minutes to terminate the reaction. The product was analysed by 1% agarose gel electrophoresis. The band containing the target gene was cut and purified.

Amplification of DNA PCR and sequencing reactions were carried out using a Perkin Elmer 480 thermal cycler. To a PCR tube (0.5 ml) containing two Ready to Go PCR™ beads (Pharmacia), other components were added and the experiment was set up as described in PCR reaction step 1 and step 2. For the sample prepared for DNA sequencing, a PCR tube (0.5 ml) containing plasmid DNA (2 μl), primer (1 μl, either PCR2.1 Rev 10 or PCR 2.1 FOR 10), Big Dye v3 (4 μl) and 13 μl H_2O to make the final volume to 20 μl. The mixed solution was covered by two drops of PCR oil and cycled 25 times at 96 °C for 30 s, 45 °C for 15 s and 60 °C for 4 minutes. The final product was transferred to a 1.5 ml Eppendorf tube for DNA sequencing by the service in ICMB (Institute of Cell and Molecular Biology, University of Edinburgh).

TOPO Cloning The PCR products of mutant genes were cloned into PCR 2.1 TOPO® plasmids. This system provides a one step cloning strategy for the direct insertion of Taq polymerase-amplified PCR products into a plasmid vector. Taq polymerase adds a single deoxyadenosine (A) to the 3' end of a PCR product. The PCR2.1-TOPO vector supplied in the kit is linearised with single, overhanging 3'-deoxythymidine (T) residue, so PCR can therefore ligate efficiently into the vector. By using this method, the PCR product of mutants was ligated into PCR2.1-TOPO and transformed into chemically TOPO competent cells to form the plasmid PCR2.1/FBP_NG (mutant). In this experiment, 4 μl inserted mutant FBP gene, 1 μl salt solution (from the TOPO cloning kit) and 1 μl TOPO vector were mixed in a 1.5 ml Eppendorf tube. The mixture was left at room temperature for 30 minutes. After

this, 2 μl product from the last step was mixed with 25 μl TOP10 cells, the mixture was sat in ice for 30 minutes, then in a 42 °C water bath for 30 seconds, and then sat in ice for 2 minutes. Then 250 μl SOC was added to the solution and shaken at 250 rpm at 37 °C for 1 hour. All solution was spread on a s-gal/LB/ampicillin plate and incubated at 37 °C for more than 12 hours until the colonies were large enough. The white positive colonies were selected for small scale preparation to produce more plasmid DNA for DNA sequencing and the following experiments. The result of the cloning was examined by cutting gene inserted plasmid DNA with EoRI or NcoI, and then checked by a 1% agarose gel.

Digestion of DNA with Restriction Endonucleases The required amount of DNA (2 μl, ~ 0.5-1 μg) was treated with the appropriate amount of enzyme (1 μl) and buffer (2 μl) and deionised water (13 μl). The sample was placed at the appropriate temperature for the required of time (buffer and temperature conditions for each enzyme as advised by the manufacturer). Typically, 2 μl blue loading dye was mixed with sample, which were subjected to electrophoresis on a 1% agarose gel. The gels were analysed and photographed under ultraviolet light.

Cloning DNA Fragments into Expression Vectors The expression vector containing wild-type FBP gene (43 μl) was cut with NcoI (1 μl) and HindIII (1 μl) in buffer 2 (5 μl, New England BioLabs) to remove the wild-type FBP gene. Also, the mutant FBP gene was removed from the TOPO vector with NcoI and HindIII. Expression vector (pTrc99A) and mutant FBP gene were purified on a 1% agarose gel. The mutant FBP DNA fragment (14 μl), the host vector (4 μl, pTrc99A), 10xT4 DNA ligase buffer (2 μl) and T4 DNA ligase (1 μl, 40,000 unit) were placed in an Eppendorf tube. A control using water (14 μl) instead of the gene or PCR product was also set up. The reaction was left at room temperature for 16-50 hours, and then the expression vector containing Y195HY196H FBP gene was purified on a 1% agarose gel. The purified DNA (4 μl) was transformed into 50 μl TOP10 cells.

Mutant FBP Expression Plasmid E57H FBP or Y195HY196H FBP was transformed to TOP10 cells and the colonies were picked up for small scale

expression. For large scale expression, instead of using LB media, 2YT was used for mutant FBP expression. All other procedures are the same as wild-type FBP expression and purification as described in Chapter 2.

3.2.2 Crystallisation of *apo*-FBP and Fe-FBPs

Apo-FBP was crystallised using the hanging-drop method. The well solution was made from PEG 1450 30%, 0.4 M imidazole/HCl buffer, pH 7.2. The concentration of the stock solution of *apo*-FBP was 380 μM in 0.1 M KCl. The drop was a mixture of 5 μl well solution and 5 μl *apo*-FBP stock solution. The crystallisation tray was left in a 4 °C room and large crystals appeared after two weeks.

Reloaded Fe-FBP was crystallised using the hanging-drop method. The well solution was made from PEG 4000 22%, 0.4 M Imidazole/HCl buffer, pH 6.9. Fe-FBP was made by reacting $Na_3[Fe(NTA)_2]$ with *apo*-FBP solution as described above. The concentration of the stock solution of Fe-FBP was 400 μM in 0.1 M KCl. The drop was a mixture of 5 μl vial solution and 5 μl Fe-FBP stock solution. The crystallisation tray was left in a 4 °C room and a large crystal appeared after two weeks.

Cluster Fe-FBP crystals were prepared by soaking *apo*-FBP crystals in a drop containing $(Hpy)_2[Fe_2(cit)_2(H_2O)_2]$. High quality *apo*-FBP crystals were prepared freshly by introducing seeds from crushed old *apo*-FBP crystals to the saturated drop. The well solution (30% PEG 1450, pH 7.2) and the crystallisation drop were prepared as described before. After one week of seeding, *apo*-FBP crystals were harvested and stored in the vial solution.

The stock solution containing Fe(III) dinuclear compound was made from 30% PEG 1450, 0.4 M imidazole/HCl buffer, pH 7.2, $(Hpy)_2[Fe_2(cit)_2(H_2O)_2]$ was added to this solution, and the final concentration of $(Hpy)_2[Fe_2(cit)_2(H_2O)_2]$ in the soaking stock solution was 10 mM.

The final soaking solution was prepared by mixing the stock soaking solution with well solution in the ratio of 30% : 70% (v/v). The *apo*-FBP crystals were transferred to the final solution and left at 17 °C overnight (~16 hours). The colour of the crystals changed from colourless (before soaking) to brown (after soaking).

E57H Fe-FBP was crystallised by the hanging drop method. The well solution is composed of 21% PEG 4000, 0.5 M imidazole/HCl buffer, pH 6.90 and 0.2 M NaCl. protein solution (5 μl) was mixed with 5 μl well solution. The crystallisation tray was stored at 4 °C, and the crystal appeared within two weeks.

3.3 Experimental Results

3.3.1 Overexpression of Mutant FBP

The structure of wild-type FBP revealed that Fe(III) is six-coordinate with octahedral geometry. In order to investigate the function of some residues around the metal binding site in FBP, two FBP mutants were prepared. In the first mutant a histidine residue replaced Glu57; In the second mutant FBP two histidine residues replace Tyr195 and Tyr196. The purpose of the mutations was to investigate which residues play key roles in metal binding.

Compared with wild-type FBP (~ 100 mg/l), the yield of E57H Fe-FBP was low (~ 20 mg/l). The colour of E57H Fe-FBP was red, and a strong LMCT band was found at 478 nm. This suggested that Fe(III) was bound to FBP. However, the yield of Y195H-Y196H FBP was high (~ 100 mg/l), but this protein had no colour. The sample as isolated was analysed by ICP-AES, no metal was found in Y195H-Y196H FBP sample. Three bands were found in the SDS-PAGE gel as shown in **Figure 3.2**, but only a single peak was found by UV detection at 280 nm during the purification process on a gel filtration column. This suggested that this protein is not stable at room temperature, but is degraded to two small fragments. The size of two fragments suggested that the bond between H195-H196 might be broken.

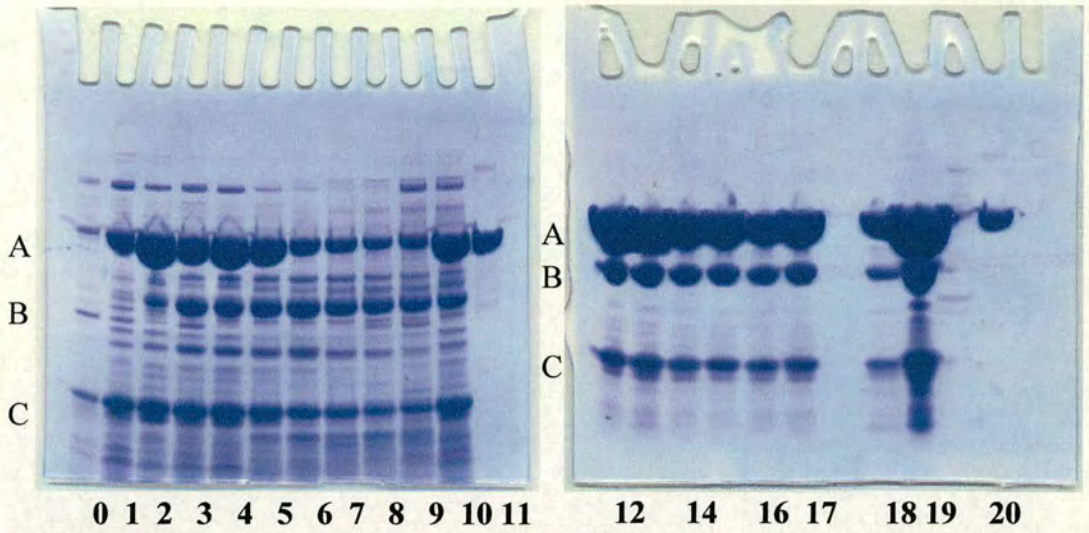

Figure 3.2 SDS-PAGE gel of Y195H-Y196H FBP. The left diagram shows the collected fragments after the protein was purified by cation exchange chromatography at 4 °C. The right diagram is the mutant protein which was purified by gel-filtration column at room temperature. Lanes 12-18 are the collected fragments after purification by gel filtration chromatography. Lane 19 is the protein before purification by gel filtration. Lane 11 and lane 20 are *apo*-FBP, which was used as reference. Three main bands were found in the gel, which were marked as A (~34 kDa), B (~25 kDa) and C (~14 kDa).

3.3.2 UV-Vis Spectra

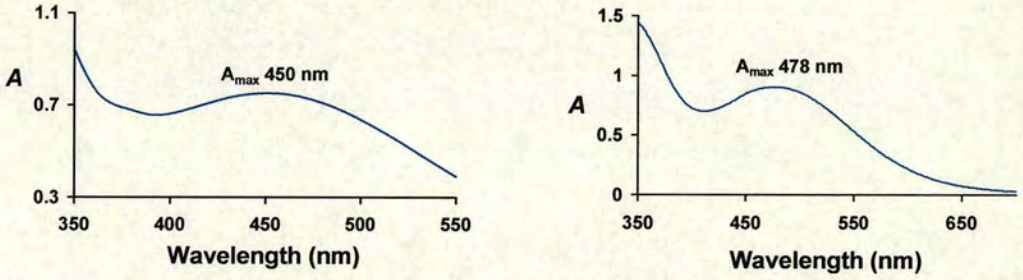

Figure 3.3 UV-Vis spectra of Fe-FBP reloaded using $(Hpy)_2[Fe_2(cit)_2(H_2O)_2]$ (left) and E57H Fe-FBP as isolated (right).

A broad charge-transfer band was found in both reloaded Fe-FBP and E57H Fe-FBP as shown in **Figure 3.3**. For the Fe-FBP made from $Na_3[Fe(NTA)_2]$, A_{max} was found

at 463 nm, but if the starting material was $(Hpy)_2[Fe_2(cit)_2(H_2O)_2]$, A_{max} was found at 450 nm. For E57H Fe-FBP, A_{max} was found at 478 nm.

3.3.3 EPR Spectra Characterisation

Holo-FBP, Fe-FBP reloaded by $Na_3[Fe(NTA)_2]$ and E57H Fe-FBP were characterised by EPR to compare their Fe(III) sites.

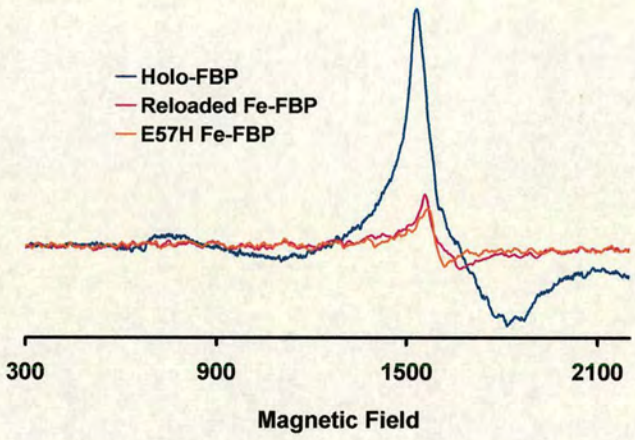

Figure 3.4 EPR spectra of *holo*-FBP (1 mM, dark blue line), reloaded Fe-FBP (0.4 mM, pink line) and E57H Fe-FBP (0.4 mM, orange line) in 10 mM Tris, 100 mM NaCl, pH 8.0. Microwave frequency 9.49 GHz; microwave power 11.1 milliwatts; receiver gain $6.3x10^4$, temperature -153 °C; conversion time and time constant , 500 ms; sweep time 500 s.

The Fe(III) binding environments in three proteins are quite similar ($g_{holo\text{-}FBP}$ = 4.43, $g_{reload\ Fe\text{-}FBP}$ = 4.35 and $g_{E57H\ FBP}$ = 4.32), the slight differences among the g values are due to small changes in the bound ligands of Fe(III) in different proteins. The EPR spectra confirm that the Fe(III) bound to FBP in the high-spin state in a weak field ligand site with low symmetry holo-FBP. Besides the concentration difference, the low intensity of signals from E57H FBP and reloaded Fe-FBP may be due to the low-spin state of bound Fe(III) ions in these proteins.

3.3.4 ICP-AES Analysis of Reloaded Fe-FBP

Fe(III) was reloaded onto *apo*-FBP with $Na_3[Fe(NTA)_2]$ in 10 mM Tris, pH 7.8. In addition, some phosphate was added to the reloaded Fe-FBP solution to observe the effect of phosphate in the process of Fe(III) binding to FBP. *Holo*- FBP was also mixed with $Na_3[Fe(NTA)_2]$ to investigate whether more iron could be loaded on to *holo*- FBP. For both samples, excess $Na_3[Fe(NTA)_2]$ was initially removed by a PD-10 column, followed by ultrafiltration. The Fe/S/P ratio was determined by ICP-AES and three repeat measurements were made; the molar concentration of sulphur was used to assess the concentration of protein (one sulphur per protein molecule). The analysis results are shown in **Table 3.2**. Multiple iron binding was found over a wide range of conditions (salt concentrations, buffers, pH). Except for *holo*-native samples, all other samples were incubated in a 37 °C water bath before purification.

Table 3.2 Analysis of Fe-FBP samples

Sample	Treatment	Mol element per mol protein	
		Fe	P
Holo-native	As isolated	1.09 ± 0.02	0.10 ± 0.03
Apo/Fe	50 x $[Fe(NTA)_2]^{3-}$, 10 mM Tris, pH 7.8 12 h	2.4 ± 0.2	0.05 ± 0.08
Apo/Fe/P	10 x $[Fe(NTA)_2]^{3-}$, 10 mM Tris, pH 7.8, then 10 x phosphate, 1.5 h	1.8 ± 0.1	1.1 ± 0.1
Holo/Fe	10 x $[Fe(NTA)_2]^{3-}$, 10 mM Tris, pH 8.0, 4 h	1.10 ± 0.03	0.20 ± 0.01

* Molar excess (e.g. 10 x) is relative to protein concentration.

From the analytical result, it seems that there is no phosphate bound to *holo*-FBP although a bound phosphate was found in the crystal structure. This is due to the

extensive washing of the protein with 10 mM Tris-HCl, pH 7.8, which led to the loss of phosphate. Treatment of *apo*-FBP with excess chelated Fe(III) gave rise to 2-3 mol Fe per mol protein. Because phosphate forms an insoluble compound with Fe(III), in the presence of phosphate, less Fe(III) was bound to *apo*-FBP than the sample in non-phosphate buffer, but a 1:1 Fe: P ratio cannot be restored. Addition of a large excess of chelated Fe(III) to mono-ferric *holo*-FBP did not lead to additional binding of Fe, although the binding phosphate was removed. These results suggest that the reloaded Fe-FBP might have a different conformation from wild-type *holo*-FBP. For *holo*-FBP the binding cleft is closed when Fe(III) and phosphate bind to the protein and no more iron can gain access to the binding site. The binding cleft of reloaded Fe-FBP might be still open, so more iron(III) can bind to the protein.

3.3.5 Characterisation of Fe-FBP by Chromatography

Results from ICP-AES analysis revealed that the product of Fe(III) loaded to *apo*-FBP is complex. The final Fe-FBP product might be a mixture of several forms of Fe-FBP. To characterise different forms of Fe-FBP, purified *holo*-FBP and reloaded Fe-FBP in 10 mM Tris (pH 8.0) were loaded into a cation exchange Mono S™ HR 5/5 (Amersham) column. The elution rate was 0.5 ml/min. The chromatograms are shown in **Figure 3.5** and **Figure 3.6**.

In **Figure 3.5**, Two peaks were observed by detection at 280 nm, however, only one peak was observed at 480 nm (the tyrosine to Fe(III) charge-transfer band). The main peak observed with absorption at both 280 nm and 480 nm was assigned to *holo*-FBP, and the small peak observed with absorption at 280 nm only was assigned to *apo*-FBP. This reveals that *holo*-FBP isolated from cells is not saturated with Fe(III), but only one form of *holo*-FBP was found in solution.

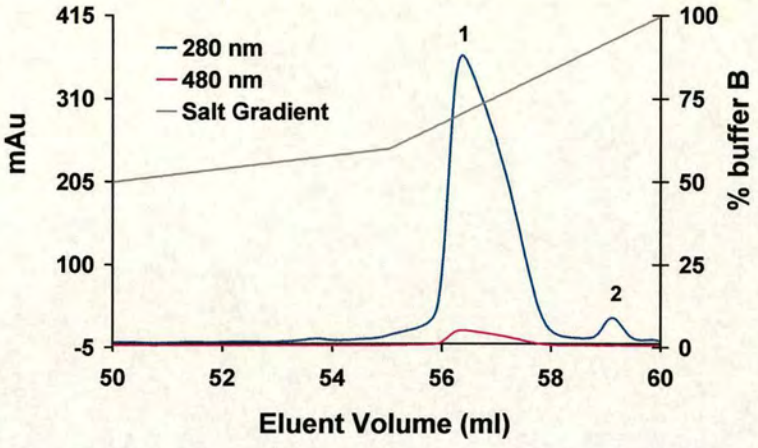

Figure 3.5 Characterisation of *holo*-FBP by chromatography on a MonoS™ HR 5/5 (Amersham) column. The left axis shows the absorption of *holo*-FBP at 280 nm and 480 nm; the right axis is the percentage of buffer B (10 mM Tris, 200 mM NaCl, pH 8.0). The grey line indicates the gradient of the buffer B applied during the elution process.

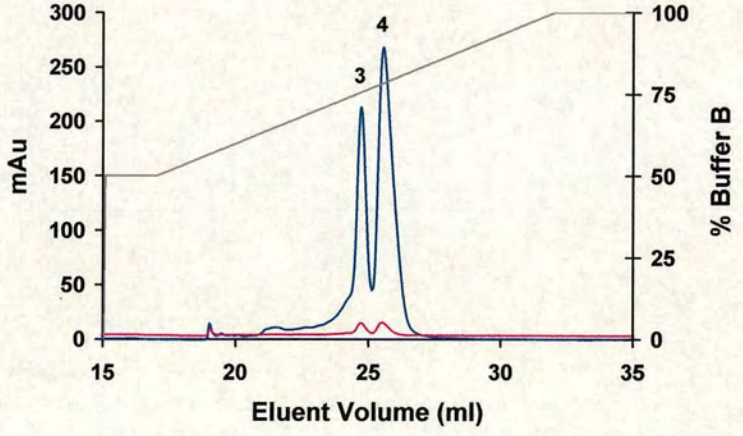

Figure 3.6 Characterisation Fe-FBP reloaded with $Na_3[Fe(NTA)_2]$ by chromatography on a MonoS™ HR 5/5 (Amersham) column. The left axis shows the absorption of *holo*-FBP at 280 nm (blue) and 480 nm (red), the right axis is the percentage of buffer B (10 mM Tris, 200 mM NaCl, pH 8.0). The grey line indicates the gradient of the buffer B applied during the elution process.

Two main peaks were found for Fe-FBP reloaded with $Na_3[Fe(NTA)_2]$. Both peaks have absorption at both 280 nm and 480 nm, which means that there are two forms of Fe-FBP in the solution. Combined with the results from ICP-AES analysis, one of the peaks is assigned to mononuclear Fe-FBP, the other peak, to polynuclear Fe-FBP.

3.3.6 Phosphoester Bond Cleavage by Fe-FBP

Enzymes which hydrolyse phosphoester bonds frequently possess catalytic metal ions in their active sites and the metal ions most frequently employed are Mg^{2+}, Zn^{2+}, Mn^{2+}, Ca^{2+} and Fe^{2+} [17]. The DNA backbone is formed by phosphodiester links, ubiquitous chemical bonds in biological systems. So hydrolysis of DNA is an important enzymatic reaction, but exceedingly difficult to mimic due to the resistance of DNA to hydrolysis [18]. Metal complexes are well established as phosphodiester cleavage agents and in general their action is mediated by a powerful nucleophilic attack [19, 20]. It has been reported that a dinuclear iron(III) complex can cleave DNA under mild temperature and pH conditions [21].

Bis(4-nitrophenyl) phosphate (BNPP) is often used for studies of the phosphodiesterase activity of metal complexes. To test the enzyme activity of Fe-FBP, the reaction between Fe-FBP and BNPP was monitored by UV-Vis at 400 nm.

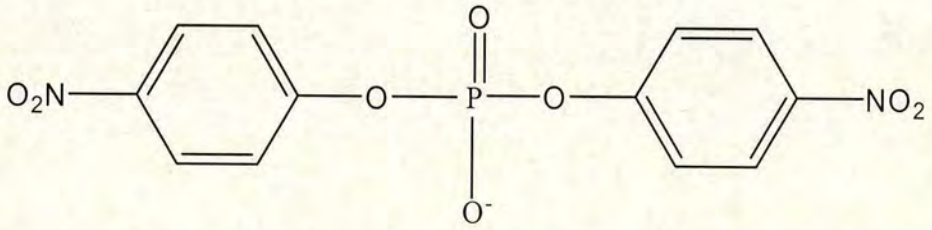

Figure 3.7 The structure of bis(4-nitrophenyl) phosphate (BNPP) [22].

Reloaded Fe-FBP was prepared as described in Section 3.2. Bis(p-nitrophenyl) phosphate (BNPP, 10 mM stock solution) was mixed with Fe-FBP in 10 mM Tris, 100 mM NaCl, pH 8.0 in a 1:1 molar ratio. The reaction was monitored by UV-Vis spectra at 37 °C from 800 nm to 220 nm in 30 minutes time intervals. Under the same

conditions, as a control, UV-Vis spectra were used to monitor any cleavage when BNPP was mixed with $Na_3[Fe(NTA)_2]$, and between BNPP and the buffer solution.

There was no reaction between either BNPP and $Na_3[Fe(NTA)_2]$ or BNPP and buffer. In addition, no reaction was detected for *holo*-Fe-P_i-FBP (Fe-FBP with phosphate bound) in 50 mM Hepes buffer, pH 7.5. However, the phosphoester bond of BNPP was cleavaged by Fe-FBP (either reloaded Fe-FBP or *holo*-Fe-FBP without phosphate). The phosphoester bond cleavage of BNPP by Fe-FBP yielded the product 4-nitrophenolate, which is yellow and has an absorption band at 400 nm.

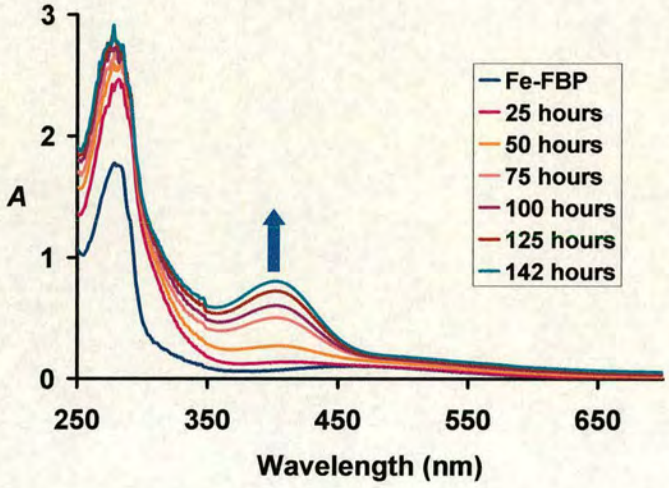

Figure 3.8 UV-Vis spectrum for the reaction between BNPP and reloaded Fe-FBP (molar ratio 1:1, pH 8.0). Hydrolysis of BNPP was followed by production of the 4-nitrophenolate anion, which is indicated by the increasing absorption at 400 nm.

Figure 3.8 shows that BNPP can be hydrolysed by Fe-FBP although the reaction is quite slow. Under the similar conditions (50 mM Tris, 0.1 M $NaNO_3$, pH 8.0) as in the experiment above (10 mM tris, pH 8.0), various amounts of BNPP were reacted with Fe-FBP at 37 °C, monitored at 400 nm, and the results are shown in **Figure 3.9**.

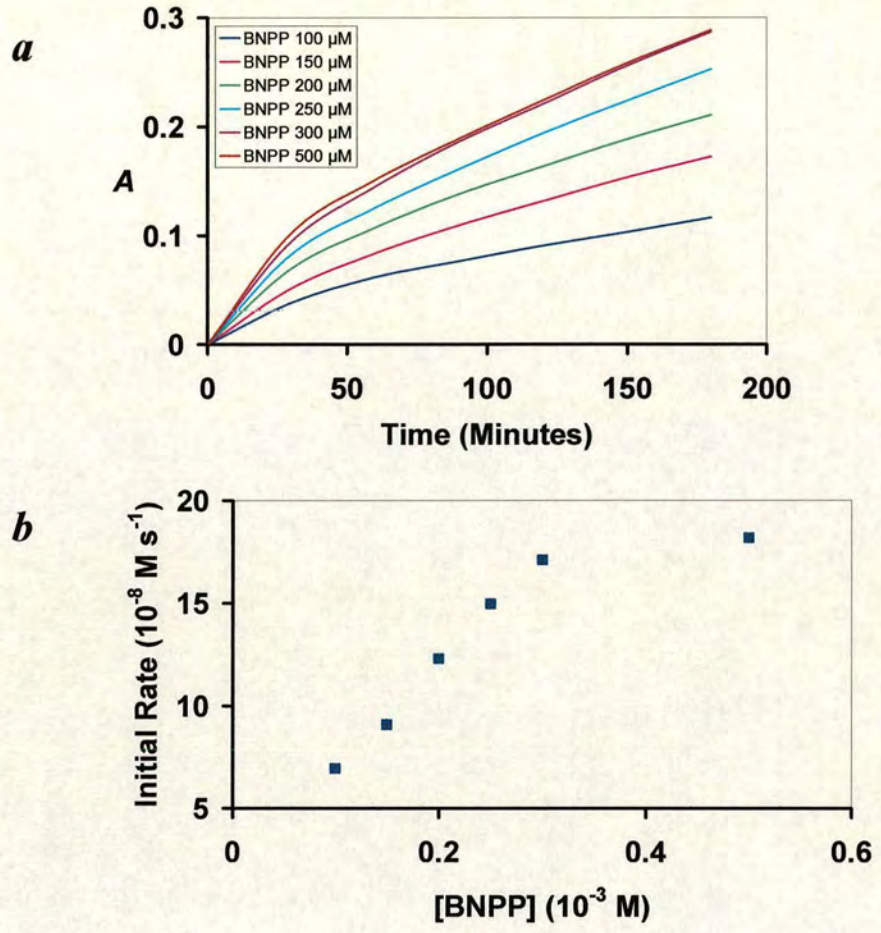

Figure 3.9 Reaction of Fe-FBP (35 μM) with various concentrations of BNPP (100 μM – 500 μM) . The reaction was monitored at 400 nm (diagram ***a***), and a plot of the initial reaction rate of 35 μM Fe-FBP versus different BNPP concentrations (100 μM – 500 μM) is shown in the diagram ***b***.

A large excess of BNPP was reacted with Fe-FBP to ensure pseudo first-order conditions. The extinction coefficient of 4-nitrophenol at 400 nm is ε_{400} = 18700 L mol^{-1} cm^{-1} [23]; it was corrected to ε_{400} = 18205 L mol^{-1} cm^{-1} at pH 8.0. At the molar ratio of Fe-FBP : BNPP = 1:14 (Fe-FBP 35 μM, BNPP 500 μM), the reaction rate is 6 x 10^{-6} mol L^{-1} s^{-1}. Under the same conditions, it would take several weeks for BNPP to undergo self-hydrolysis. At pH 7.0 and 100 °C, the self-hydrolysis rate of BNPP in water is 3.9 x 10^{-10} [24]. Therefore Fe-FBP-catalysed hydrolysis is at least 10^4 times faster than the self-hydrolysis rate of BNPP in water.

The phosphoester bond cleavage of BNPP by Fe-FBP suggested that Fe-FBP may cleave DNA under mild conditions. Linear PUC18 plasmid DNA was used in a reaction with Fe-FBP in 50 mM Hepes, pH 7.5. The mixture was examined with 1% agarose gel and 6% DNA retardation gel as shown in **Figure 3.10**.

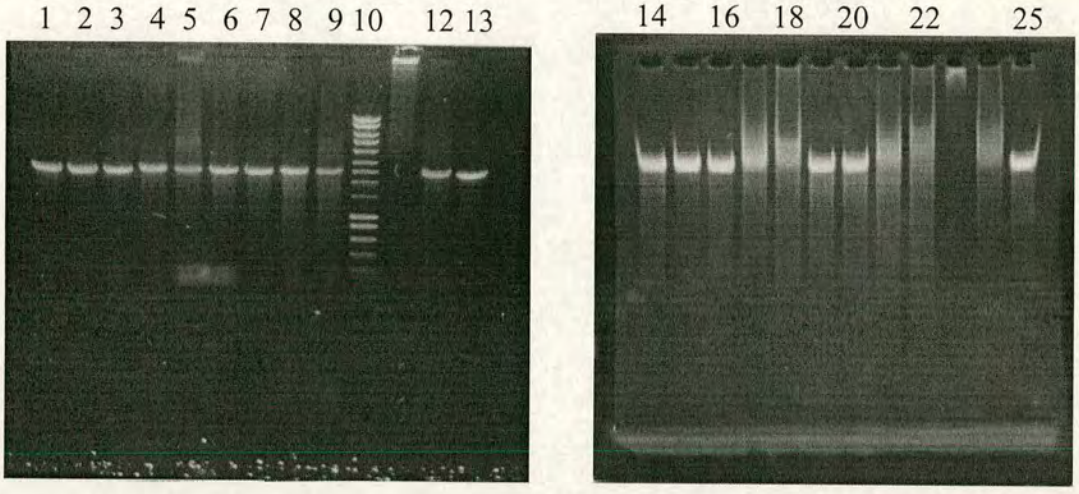

Figure 3.10 Characterisation of the reaction between Fe-FBP and linear PUC18 DNA on a 1% agarose gel (left) and 6% DNA retardation gel (right). In the agarose gel, lane 1 is DNA only, lanes 2 to 5 are various concentrations Fe-FBP (0.1 μM, 0.2 μM, 0.5 μM and 1 μM) mixed with linear PUC18 DNA and incubated at 37 °C for 3 hours. Lanes 6 to 9 are the same samples as lanes 2 to 5, but incubated at 37 °C for 24 hours. Lane 10 is DNA marker I (Bioline, band size 10,000 ~ 200), lane 12 is *holo*-FBP (1 μM) incubated with linear PUC18 DNA (37 °C, 24h), lane 13 is $Na_3[Fe(NTA)_2]$ (200 μM) incubated with linear PUC18 DNA (37 °C, 24h). The same samples in the same order were loaded onto the 6% DNA retardation gel, but in lane 25, the concentration of $Na_3[Fe(NTA)_2]$ was increased from 200 μM to 600 μM.

There is no clear evidence for DNA cleavage in both gels because no bands for small fragment band are seen on the gel. However, with the increasing Fe-FBP concentration and increasing incubation time, the DNA band became more and more blurred, and the intensity of the DNA band became also weaker and weaker. With a large excess of Fe-FBP to DNA, a precipitate formed. There is no obvious shift

difference between free DNA band (lane 1 and lane 14 in **Figure 3.10**) and band for the the protein-DNA mixture (lanes 2-9 and 15-22). Compared with Fe-FBP, when much more concentrated *apo*-FBP mixed with DNA, there is no difference can be observed between *apo*-FBP-DNA sample and free DNA sample in the gel. As a control, no reaction between $Na_3[Fe(NTA)_2]$ and linear PUC18 DNA was detected.

Hence, the conclusion is that Fe-FBP cleavage of linear PUC18 DNA is not really detected under the conditions used here. This may be due to the steric effect of the DNA, the size of linear DNA is too large to access the small metal binding pocket of Fe-FBP, although for reloaded Fe-FBP, the binding cleft is open. However, Fe-FBP is highly positively-charged, and DNA is highly negatively-charged, so there can be a strong electrostatic interaction between them. This may explain why the DNA band became weaker under conditions of higher Fe-FBP concentration and longer incubation time.

3.3.7 Crystallisation of *apo*-FBP and Reloaded Fe-FBP

The crystallisation conditions for *apo*-FBP, mononuclear Fe-FBP were screened using commercially-available screen solutions from Hamilton Research® and Molecular Dimensions®. It was found that crystals only grew in PEG containing solutions. Further screening experiments were done at various pH values (pH 6.0 - pH 8.5), different PEG concentrations (12% - 35%), different temperatures (4 °C and 17 °C) and with various types of PEG (PEG 400, PEG 1350, PEG 1450, PEG 3500, PEG 4000 and PEG 6000).

In most cases, for both proteins, large needle crystals (looking like a pencil) were grown two weeks after setting up the crystallisation tray. The crystals are large, and they were very smooth and transparent, but only diffracted to 3.3 Å maximum. A large unit cell was found for such kinds of crystals, which contains 25 molecules per unit cell. This made the structure determination work very difficult. Luckily, with the same crystallisation conditions, when the crystallisation tray was left at 4 °C, it happened once that some crystals with a new crystal form appeared two weeks after

setting up. This kind of crystal diffracted to higher resolution (1.5 Å for *apo*-FBP and 1.7 Å for Fe-FBP), and the unit cell contained only 9 molecules. At other times, even at 4 °C, with the same crystallisation condition, only large needle crystals were produced. The *apo*-FBP crystal which diffracted at high resolution was crushed and used as seeds to produce more high resolution *apo*-FBP crystals for further soaking experiments.

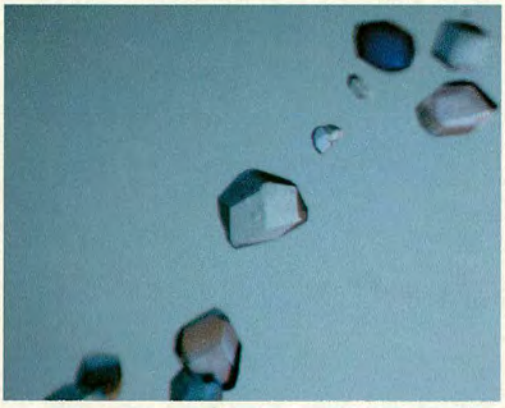

Figure 3.11 *Apo*-FBP crystals produced by introducing the seeds from crushed *apo*-FBP crystals to fresh saturated crystallisation drops. The colour of crystals is due to the light polarisation.

High-quality reloaded Fe_3-FBP crystals cannot be prepared by co-crystallisation. So, the soaking method was used. First of all, high-quality *apo*-FBP was prepared as described in the experimental section; then it was soaked in a solution containing dinuclear iron(III) complex - $(Hpy)_2[Fe_2(cit)_2(H_2O)_2]$. The colour of the crystal changed from colourless to brown-red (**Figure 3.12**), which means that iron was bound to *apo*-FBP during crystal soaking.

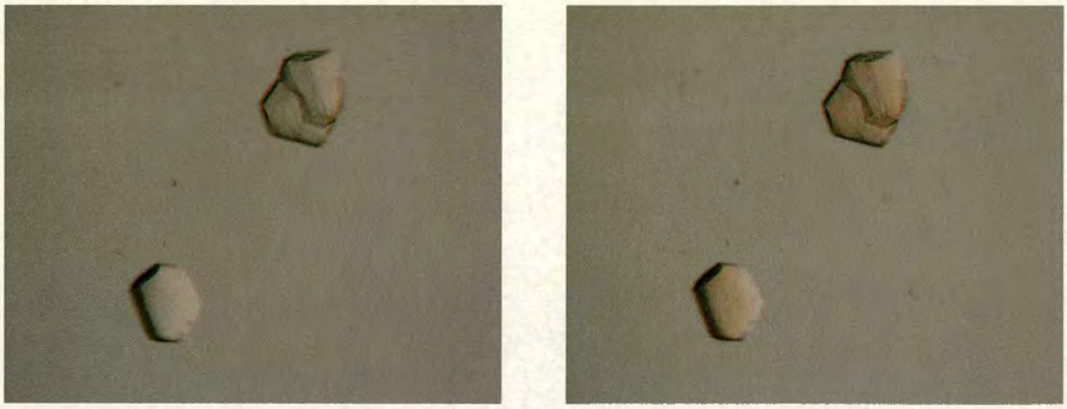

Figure 3.12 *Apo*-nFBP crystals soaking in a well solution containing the dinuclear $(Hpy)_2[Fe_2(cit)_2(H_2O)_2]$ complex. The left picture was taken immediately after the *apo*-FBP crystals were introduced to the soaking solution, the right picture was taken after 90 minutes soaking. The colour of crystals in the right picture is much redder than the colour of crystals in the left picture; this reveals that after soaking, Fe(III) binds to *apo*-FBP.

3.3.8 Crystal Structures of *apo*-nFBP, Fe-nFBP and Fe_3-nFBP

All three crystal structures were determined by Dr. Dmitriy Alexeev in ICMB (Institute of Cell and Molecular Biology) of The University of Edinburgh.

***Apo*-nFBP Structure** The crystal of *apo*-FBP from *Neisseria gonorrhoeae* diffracted to 1.9 Å resolution. There are 9 molecules in the asymmetric part of the unit cell, and the interdomain hinges of all 9 molecules are open. Similar to the structure of *apo*-FBP from *Haemophilus influenzae* [11], a phosphate is specifically bound to the N-terminus of the helix which terminates in Ala141 and the phosphate oxygens are within 3-4 Å of the oxygens of Tyr195 and Tyr196. At the metal binding sites of all 9 molecules, His9 and Glu57 are swung away, but the side-chains of Tyr195 and Tyr196 show versatile dynamic roles. One of the molecules in all 9 molecules is different from the other 8 molecules in that Tyr196 also has partial occupancy of a site in which it is flipped towards the entrance of the binding cleft (**Figure 3.13**).

Table 3.3 Crystallographic data and refinement statistics. Numbers in parentheses are for the highest resolution shell.

Parameter	***Apo*-FBP**	**Fe-FBP**	**Fe_3-FBP**
Wavelength (Å)	1.54	1.49	1.54
Resolution	1.80	1.80	1.77
Refined twinning fraction (%)	30.1	44.0	44.1
Completeness (%)	99.9 (99.7)	91.4 (64.1)	96.5 (87.1)
I/Σ	19.1 (5.2)	11.1 (1.2)	7.1 (2.1)
R_{sym}* (%)	5.4	8.5	11.7
R_{cyst}† (%)/R_{free}‡ (%)	15.6/31.6	19.1/35.2	16.7/30.0
rms deviations			
Bonds (Å)	0.007	0.007	0.006
Angles (°)	1.22	1.32	1.15
Average B-factors			
Protein (Å^2)	29.7	43.1	39.8
Water (Å^2)	35.3	37.6	35.8

*$Rsym = \Sigma|I_h - \langle I_h \rangle|/I_h$, where $\langle I_h \rangle$ is the average intensity over symmetry equivalent reflections. †$R_{cyst} = \Sigma|F_o - F_c|/\Sigma F_o$, where summation is over the data used for refinement. ‡R_{free} was calculated using 3% of data excluded from refinement.

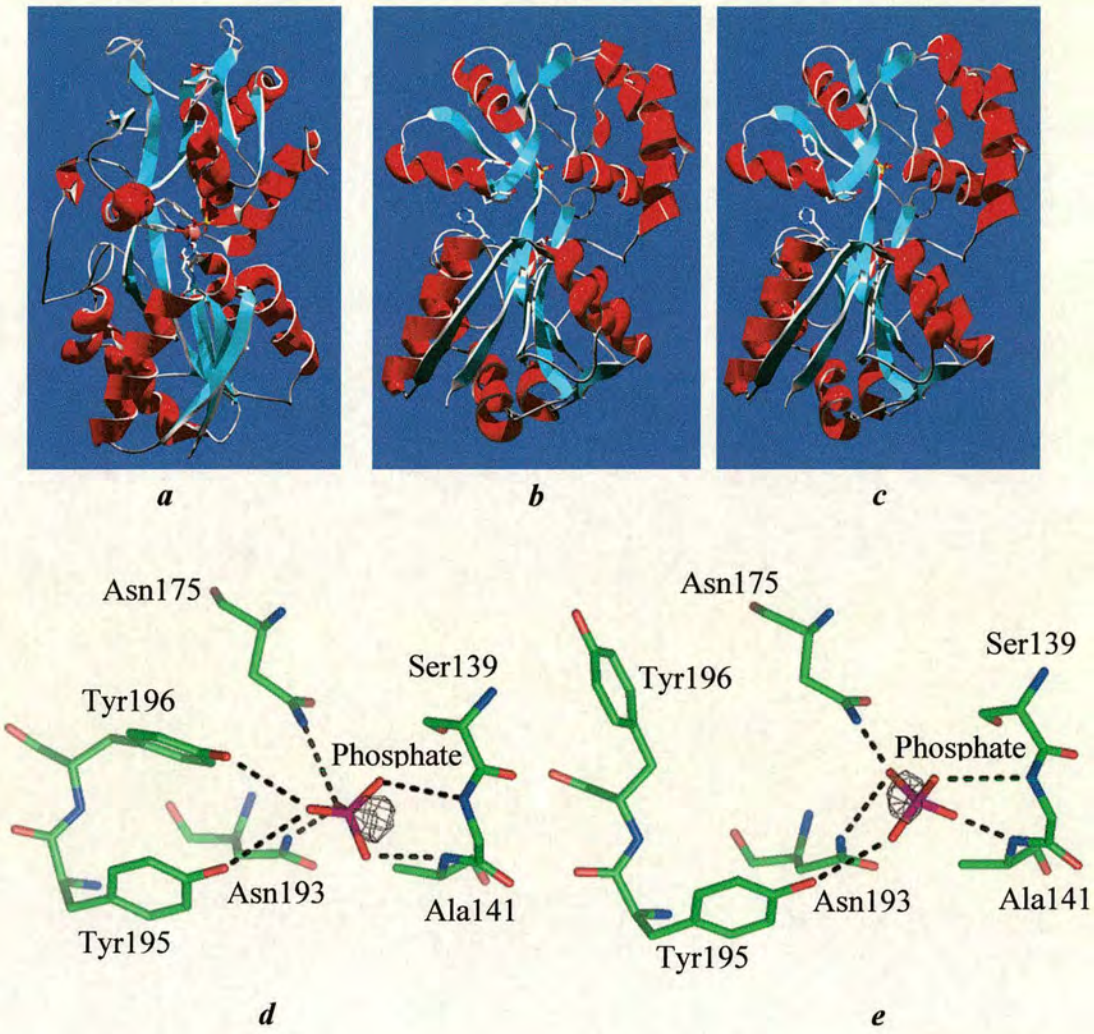

Figure 3.13 (*a*) Crystal structure of *holo*-nFBP [25]; the interdomain cleft is closed. (*b*) Molecule A in the unit cell of *apo*-nFBP; the interdomain cleft is open; both Tyr195 and Tyr196 are pointing to the metal binding site, and a phosphate is bound to the N-terminal domain. (*c*) Molecule F in the unit cell of *apo*-nFBP. It is different from the other molecules in the unit cell. Tyr196 is flipped towards the entrance of the binding cleft, but the binding cleft is also open. (*d*) The binding site of molecule A of *apo*-nFBP. Phosphate forms hydrogen bonds with Tyr195, Tyr196, Ser139, Ala141, Asn175, and Asn193. (*e*) The binding site of molecule F of *apo*-nFBP. Tyr196 in this molecule is different from other molecules in the same asymmetric unit cell; it is swung away and does not form hydrogen bonds with phosphate.

Fe-nFBP structure The crystal of Fe-nFBP was prepared by co-crystallisation and diffracts to 1.9 Å. The structure shows the presence of an open-cleft protein with a single Fe(III) bound only to Tyr195 and Tyr196, to NTA and water as ligands (**Figure 3.14**). Fe(III) is shielded by a chelating NTA ligand in much the same way as by bound EDTA in the recently reported *Haemophilus influenzae* Fe-(EDTA)-FBP in which His9 had been mutated to Gln [26]. This structure reveals that open-cleft mono-Fe-FBP can be formed and it is stable.

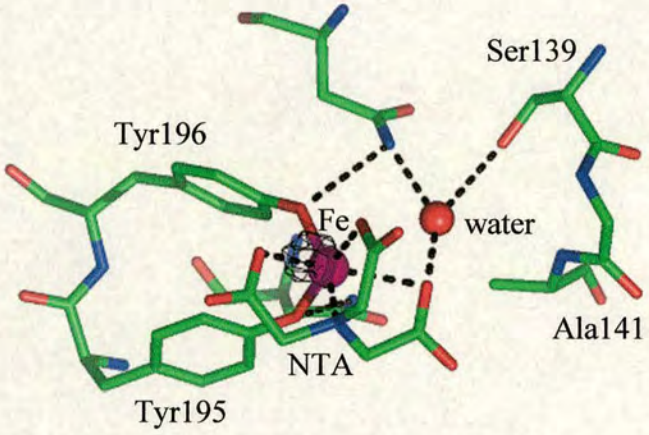

Figure 3.14 Metal binding site of Fe(NTA)-nFBP. Fe is bound to both tyrosines in all nine molecules. The binding cleft is open.

An open-cleft form of Fe-(N-lobe)ovotransferrin prepared by soaking crystals of the *apo*-protein with Fe-NTA has been reported [27]. It was said in the report that the open conformation was trapped by crystal packing forces, but in our case, the Fe(NTA)-nFBP crystal was obtained with co-crystallisation, so the cleft opening observed does not appear to depend on such forces. A similar structure reported recently is the 18 kDa NII domain fragment of duck ovotransferrin-nitrilotriacetate complex, the Fe(III) is bound to the synergistic carbonate anion and only one tyrosine residue in a manner almost identical to the intact protein. The carboxylate groups and the tertiary amino group of the nitrilotriacetate occupy the remaining coordination sites. The second tyrosine residue, Tyr95, is not bound directly to the iron [28].

Fe_3-nFBP structure It seems that Fe_3-FBP is the first example of an oxo tri-iron centre in a metalloprotein. Although the electron density does not reach atomic resolution, the maps clearly indicated the presence of tri-iron clusters. The orientation of the cluster in the metal-binding clefts of the nine molecules in the asymmetric part of the unit cell vary, but the overall shapes of all clusters are very similar and correspond well to Fe_3O_{13} tri-iron structural units. Examples of these clusters include $[Fe_9O(cit)_8(H_2O)_3]^{7-}$ [29] and Fe_{19} oxyhydroxide clusters [30]. Each cluster is situated in an open binding cleft, and contains a triangle of Fe(III) ions with each pair bridged by a μ_2-oxygen. There is a central μ_3-oxygen coordinated to all three irons. Three additional terminal oxygens coordinate to each Fe(III) of the tightly bridged Fe_3O_4 unit and complete the oxygen coordination shell of the octahedral iron atoms within the Fe_3O_{13} cluster.

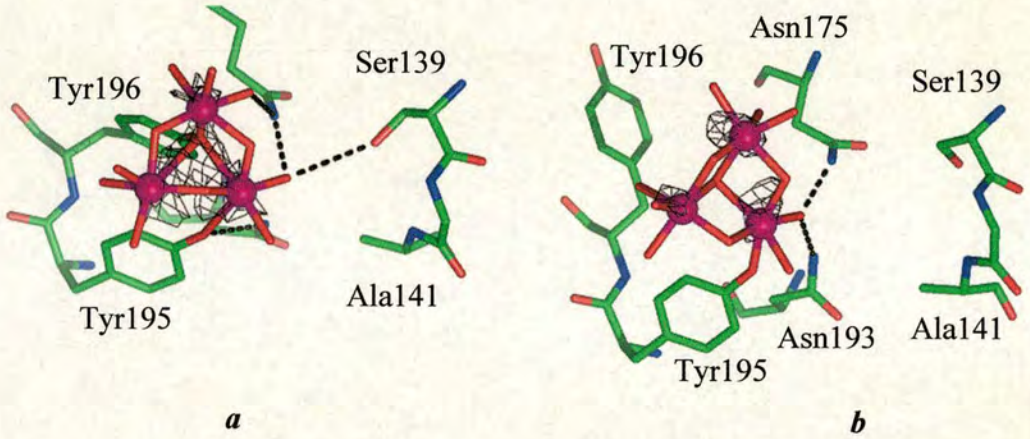

Figure 3.15 Binding site of Fe_3-FBP. (*a*) Trinuclear oxo-iron cluster in molecule A of Fe_3-FBP. Both Tyr195 and Tyr196 coordinate to the cluster. (*b*) Trinuclear oxo-iron cluster in molecule F of Fe_3-FBP. Tyr196 is flipped out.

Besides molecule F, the hydroxyl groups of Tyr196 of all other molecules in the nine molecules in the asymmetric unit cell of Fe_3-FBP are deprotonated and occupy the position of the central μ_3-oxygen in the coordination sphere of the tri-iron cluster. In molecule F, Tyr196 is turned away from the cluster and the μ_3-oxide is recruited from water. The coordination of Tyr195 varies much more widely. In some

molecules (A, B, F, G, H, I), Tyr195 is deprotonated and directly coordinated to iron. In other molecules, Tyr195 forms a hydrogen bond with one of the terminal oxygens of the cluster in molecules D and E, and one of the bridging μ_2-oxygens in molecule C. No citrate was found in Fe_3-FBP although the starting material was an Fe-citrate complex.

3.4 Discussion

The results above show that the dityrosyl motif plays a dynamic role in the capture of oxo tri-iron clusters, which suggests that FBP could be involved in a novel mode of iron acquiring from oxohydroxy iron polymers and minerals. The structure of *apo*-nFBP provides evidence of the versatile dynamic roles of the side-chain of Tyr195 and Tyr196. Similar to the structure of Fe_3-FBP, Tyr196 in molecule F of *apo*-FBP is also flipped towards the entrance of the binding cleft, suggesting a potential role for Tyr196 in guiding iron complexes into the cleft.

The binding clefts in all three structures (*apo*-nFBP, Fe-nFBP and Fe_3-nFBP) are open. However, the binding cleft of *holo*-Fe-P_i-FBP is closed. This means that after the metal is loaded onto the *apo*-FBP, phosphate controls the closure of the binding cleft. In the absence of phosphate, the binding cleft of iron FBP is open. Fe(III) in open-cleft FBP is accessible and potentially reactive. This is the reason why BNPP can enter the binding cleft and react with iron-FBP. However, in the *holo* form of Fe-P_i-FBP, due to the closure of the binding cleft, BNPP cannot gain access to the iron, so no reaction could be detected. It will be interesting to investigate the reaction between iron FBP and various natural substrates. The open form of iron FBP shows phosphatase activity, which might be a way to acquire phosphate to close the binding cleft. The phosphatase activity provides a mechanism for signalling iron status, and coupling cluster breakdown and cleft-closure around a single iron.

In a recent 2.5 Å resolution x-ray study, crystals of outer membrane iron transporter *apo*-FecA soaked in ferric citrate at pH 8 appeared to capture diferric dicitrate itself, triggering a conformational change of the extracellular loops of FecA, and closing

the external pocket [31]. The formation of Fe_3-FBP means that FBP could act as a periplasmic receptor for iron clusters taken up by FecA. In contrast to Fe-NTA-FBP, none of the oxo tri-iron clusters bound to FBP appears to contain bound chelated ligand (citrate). In the structure of $(Hpy)_2[Fe_2(cit)_2(H_2O)_2]$, two Fe(III) ions bridged by two alkoxide oxygen atoms of fully deprotonated citrate ligands [15]. The complex is stable in acidic solution at pH 2-3, in equilibrium with higher order clusters such as $[Fe_9O(cit)_8(H_2O)_3]^{7-}$ [29]. In 1:1 Fe(III) citrate solutions, citrate dissociates from Fe(III) at pH 4 and above, to give hydroxyl-iron polymers (particles) with citrate ions bound to the surface to prevent precipitation [32]. This chemical transformation could readily be observed by UV-Vis. The colour of the solution changed from yellow-green to red-brown at pH 8. The changing rate depends on the conditions. When strong hydroxide was added, the colour was changed immediately, when buffer was added, the colour was changed slowly. Exposure the solution to light also accelerated the colour change.

Previously, it has been thought that iron is transported across the periplasm only as mononuclear centres. In this Chapter, the finding that iron oxohydroxide clusters can bind to FBP suggests that fragments of mineralised iron can also be transported. It has been found that FBP can access the outer surface of bacteria [33] and so the clusters could perhaps be acquired directly from the environment. Alternative pathways for cluster acquisition by FBP might involve sequential acquisition of iron from mononuclear transporters in the outer membrane, and in some bacteria, via FecA and diferric citrate recognition system. Studies of a wide range of bacteria should now enable exploration of these proposed iron transport pathways with potential for increased understanding of bacteria-mineral interfaces and virulence, and the design of novel antibiotics.

References

1 Price, N.M., Morel F.M.M., in *Met. Ions. Biol. Syst.* **V35**, (eds. Sigel, A. and Sigel, H.) 2 (Marcel Dekker, New York, 1998).

2 Archibald, F.S., *FEMS Microbiol. Lett.*, **19**, 29 (1983).

3 Byers, B.R., Arceneaux, E.L., in *Metal Ions in Biological Systems* **V35**, (eds. Sigel, A. and Sigel, H.) p42 Marcel Dekker, New York, (1998).

4 Greenwood, N.N., and Earnshaw, A., *Chemistry of the Elements*, Pergamon Press, Oxford, p1275 (1984).

5 Lankford, C.E., *CRC Crit. Rev. Microbiol.* **2**, 273 (1973).

6 M. Y. Moridani, *Ph. D. Thesis, 3-Hydroxypyridin-4-ones Iron Chelators*, University of London (1996).

7 Genco, C.A., and Desai, P.J., *Trends Microbiol.*, **4**, 232 (1996).

8 Cornelissen, C.N., and Sparling, F.P., *Mol. Microbiol.*, **14**, 843 (1994).

9 Ferreiros, C., Criado, M.T., & Gomez, J.A., *Comp. Biochem. Physiol. B*, **123**, 1 (1999).

10 Gerstein, M., Anderson, B.F., Norris, G.E., Baker, E.N., Lesk, A.M., and Chothia, C., *J. Mol. Biol.*, **234**, 357 (1993).

11 Bruns, C.M., Anderson, D.S., Vaughan, K.G., Williams, P.A., Nowalk, A.J., McRee, D.E., and Mietzner, T.A., *Biochemistry*, **40,** 15631 (2001).

12 Jeffrey, P. D., Bewley, M. C., MacGillivray, R. T. A., Mason, A. B., Woodworth, R. C., and Baker, E. N., *Biochemistry* **37**, 13978 (1998).

13 Guo, M., Harvey, I., Yang, W., Coghill, L., Campopiano, D.J., Parkinson, J.A., MacGillivray, R.T.A., Harris, W.R., Sadler, P.J., *J. Biol. Chem.*, **278**, 2490 (2003).

14 Clegg, W., Powell, A.K., Ware, M.J., *Acta Crystallogr. Sec. C*, **40**, 1822 (1984).

15 Shweky, I., Bino, A., Goldberg, D.P., Lippard, S.J., *Inorg. Chem.*, **33**, 5161 (1994).

16 Sarker, G., Sommer, S., *Biotechniques* **8**, 404 (1990).

17 Hegg, E. L., Burstyn, J. N., *Coord. Chem. Rev.*, **173**, 133 (1998).

18 Radzicka, A., Wolfenden, R., *Science* **267**, 90 (1995).

19 Sreedhara, A., Freed, J.D., Cowan, J.A., *J. Am. Chem. Soc.* **122** 8814 (2000).

20 McCue, K.P., Morrow, J.R., *Inorg. Chem.* **38**, 6136 (1999).

21 Neves, A., Terenzi, H., Horner R., Horn Jr., A., Szpoganicz B., Sugai, J., *Inorg. Chem. Commu.* **4** 388 (2001).

22 Bond, D.R., Modro, T.A., Niven, M.L., Nassimbeni, L.R., *S. Afr. J. Chem.* **38**, 78 (1985).

23 Deck, K. M., Tseng, T. A., Burstyn, J. N., *Inorg. Chem.* **41**, 669 (2002).

24 Kirby, A.J., Younas, M.J., *Chem. Soc. B* 510 (1970).

25 Mcree, D. E., Bruns, C. M., Williams, P. A., Mietzner, T. A., Nunn, R., *Protein Data Bank*, http://www.rcsb.org, deposited 1999.

26 Shouldice, S.R., Dougan, D.R., Skene, R.J., Tari, L.W., McRee, D.E., Yu, R. and Schryvers, A.B., *J. Biol. Chem.* **278**, 11513 (2003).

27 Mizutani, K., Yamashita, H., Kurokawa, H., Mikami, B., Hirose, M., *J. Biol. Chem.* **274**, 10190 (1999).

28 Kuser, P., Hall, D. R., Haw, M. L., Neu, M., Evans, R. W. and Lindley, P. F. *Acta Cryst.* **D58**, 777 (2002).

29 Bino, A., Shweky, I., Cohen, S., Bauminger, E.R., Lippard, S.J., *Inorg. Chem.* **37**, 5168 (1998).

30 Goodwin, J.C., Sessoli, R., Gatteschi, D., Wernsdorfer, W., Powell, A.K., Heath, S.L., *J. Chem. Soc. Dalton* **12**, 1835 (2000).

31 Ferguson, A.D., Chakraborty, R., Smith, B.S., Esser, L., van der Helm, D., Deisenhofer, J., *Science* **295**, 1715 (2002).

32 Spiro, T.G., Pape, L., Saltman, P., *J. Am. Chem. Soc.*, **89**, 5555 (1967).

33 Ferreirós, C., Criado, M.T., Gómez, J.A., *Comp. Biochem. Physiol.* **B123**, 1 (1999).

Chapter 4 Hafnium(IV)-FBP

4.1 Introduction

Hafnium has a similar chemistry to iron in water at physiological pH. With the aim of designing novel metalloantibiotics, hafnium is a good choice of hetero-metal for investigating the hetero-metal-FBP interactions.

Hafnium has an atomic weight of 178.49 and its atomic number is 72. The electronic configuration is $[Xe]4f^{14}5d^{2}6s^{2}$, and atomic radius (empirical) is 155 pm [1]. There are six naturally occurring isotopes [2]:

Isotope	Natural abundance	Nuclear spin (I)	Isotope	Natural abundance	Nuclear spin (I)
^{174}Hf	0.16	0	^{178}Hf	27.28	0
^{176}Hf	5.26	0	^{179}Hf	13.62	9/2
^{177}Hf	18.60	7/2	^{180}Hf	35.08	0

After the discovery of zirconium, on the basis of Bohr's theory, a new element was expected to be associated with zirconium. It was finally identified in *zircon* ($ZrSiO_4$) from Norway, by means of X-ray spectroscopy analysis. It was named in honour of the city in which the discovery was made (Copenhagen). Most zirconium minerals contain 1 to 5% hafnium. The properties of hafnium are considerably influenced by the impurities of zirconium present. Of all the elements, zirconium and hafnium are two of the most difficult to separate. Their chemistry is almost identical. This is due in considerable measure to the effect of the lanthanide contraction making both the atomic and ionic radii (1.45 and 0.74 Å for Zr and Zr^{4+}; 1.44 and 0.75 Å for Hf and Hf^{4+}) essentially identical. However, the density of zirconium metal is about half that of hafnium. Zirconium and hafnium, because of the larger atoms and ions, differ from titanium in having more basic oxides, having somewhat more extensive aqueous chemistry, and more commonly attaining higher co-ordination numbers, 7

and 8. They have a more limited chemistry of the 3+ oxidation state. Hafnium is resistant to concentrated alkalis, but at elevated temperatures reacts with oxygen, nitrogen, carbon, boron, sulphur and silicon. Halogens react directly to form tetrahalides [3, 4].

4.1.1 Co-ordination Chemistry of Hafnium

The co-ordination chemistry of Hf involves many complexes with organic ligands. Cyclopentadienyl complexes Hf(IV) are especially common [5]. Generally, hafnium forms seven or eight co-ordinate complexes.

Three Hf(IV) complexes have been used in previous work to study the interaction with transferrin. The structures of two of these complexes have been determined by X-ray diffraction, the other complex was characterised by IR and Raman. $(NH_4)_2[Hf\{N(CH_2COO)_3\}_2]$ is a stable complex in aqueous solution throughout a wide pH range [6]. The synthesis and the crystal structure of this complex were published by Held et. al. in 2000 [7]. The structure of the complex $K_4Hf(C_2O_4)_4 \cdot 5H_2O$ was also determined by X-ray diffraction [8]. The complex $K_2[Hf(O_2)_2(cit)] \cdot H_2O$ has been synthesised and characterised by Dengel and Griffith, who found that this complex is stable only at pH values below 2 [9].

4.1.2 Biological Application of Hafnium

Hafnium is a reactive metal closely related to titanium and zirconium. When Ti and Hf were evaluated as implant materials in a biological environment, there were no quantitative and qualitative differences in the tissue organisation detected between them. This means that Hf is an interesting metal for biomedical applications [10]. When administered orally, hafnium was not absorbed by digestive organs [11]. However, it was found that hafnium could react with blood components and transport proteins [12]. Because of its biological similarity to ^{239}Pu, ^{181}Hf was used as a non-α-particle-emitting analog of Pu for metabolic, biochemical and selected human investigations [13]. In rats and hamsters, the radiohafnium organ distribution was skeleton > skin > muscle > liver at approximately 7 days postinjection. Biochemical

studies showed that the radiohafnium was bound mainly to the Fe-transport protein, transferrin, in blood plasma, and in the liver cytosol of both the rat and the hamster [14].

Several studies have been carried out to investigate interactions between hafnium and transferrin. One of them is the in vivo and in vitro studies of hafnium binding to rat serum transferrin. Three Hf(IV) complexes (Hf-NTA, Hf-oxalate and Hf-citrate) were used in these studies. The results show that with increasing percent iron-saturation of the serum from 32% to 86%, the fraction of ^{181}Hf bound to the protein was reduced; in the presence of excess iron, none of the ^{181}Hf was bound to protein [15]. Each of the two metal sites in transferrin was able to bind hafnium [16].

Studies of the interaction between Hf(IV) and lactoferrin showed that the binding situation is quite similar to transferrin. The binding was also influenced by: *a)* the presence of phosphate; *b)* the pH of the buffer, and *c)* the temperature [16].

Table 4.1 The influence of iron on hafnium binding to rat serum proteins [15]

Sample[a]		**% Iron saturation**	**% total serum ^{181}Hf recovered in protein fraction**
^{181}Hf-labelled rat serum	A	32	91 ± 3
	B	84	17 ± 4
	C	150	<2
Stable iron added to ^{181}Hf-labelled rat serum (A)		86	54 ± 12
		>200	<2

[a]Means (±SEM) of three analyses per point. Hafnium concentration in serum: 3 μM.

In experiments on Hf(IV) binding to transferrin, apart from the two specific binding sites, the authors suspected that there was a third binding site [15], which was not identical to the specific metal sites detected before [17]. The essential criterion for the specific binding of metals is the demonstration of competitive binding [18]. It was thought that because transferrin is optimised for the binding of iron, the binding strength of other metals to the specific sites is smaller by some orders of magnitude than that for iron [19].

4.1.3 Summary of Studies in this Chapter

Due to the structural and biological similarity between FBP and transferrin [20], a mononuclear Hf(IV) complex $Na_2[Hf(NTA)_2]\cdot 2H_2O$ and Hf(IV)-citrate complex were synthesised and characterised, and then Hf(IV) was loaded to *apo*-Fbp and the reaction was investigated by UV-Vis spectra, ICP-AES, ^{31}P NMR and cation-exchange chromatography. Finally, Hf-FBP was crystallised and the structure was determined by X-ray diffraction. To design novel metalloantibiotics targeted on the bacterial periplasmic iron transport protein (FBP), Hf-FBP provides a good example of the hetero-metal interaction.

4.2 Experimental Methods

Chemicals Hafnium chloride (Prod. No. 293250250) was purchased from Acros Organics. Sodium bicarbonate (Cat. No. S-5761), and Hepes ([4-(2-hydroxyethyl)-1-piperazineethanesulfonic acid], Cat. No. H3375), imidazole (Cat. No. I-2399), malic acid (Cat. No. M-0875), nitrilotriacetic acid (NTA, Cat. No. N-8407), *apo*-transferrin (human, Cat. No. T-4382) and atomic absorption standard solutions of P (Cat. No. 20735-7) and S (Cat. No. 33329-8) were obtained from Sigma-Aldrich. Sodium dihydrogen orthophosphate, sodium chloride and orthophosphoric acid (Prod. No. 010450/PB08) were purchased from Fisher Scientific. Tri-sodium citrate (Prod No. 10242), potassium chloride, plasma emission standard solution for Hf (Prod No. 455442W) and polyethylene glycol 4000 (Prod. No. 442734X) were purchased from BDH.

pH measurements The pH values of the solutions were adjusted by NaOH or HCl and measured with a Corning 240 pH meter equipped with an Aldrich micro combination electrode. The calibration buffer solutions were purchased from Aldrich with pH values of 4.00, 7.00 and 10.01 (20 °C).

UV-Vis spectroscopy All experiments were performed with 1 cm quartz cuvettes with a 0.5 ml working volume. The spectra were recorded from 600 nm to 220 nm, and reactions were monitored at 245 nm.

Preparation of $Na_2[Hf\{N(CH_2COO)_3\}_2]\cdot 4H_2O$ This complex was prepared by a slight modification of Then's method [15]. $HfCl_4$ was dissolved in 2M HCl. One mole of this solution was added to four moles of nitrilotriacetic acid (NTA) at 80 °C and neutralised by an appropriate amount of sodium bicarbonate at room temperature. The solution was heated to decrease the volume, and then cooled to room temperature. Large crystals appeared quickly. The product was recrystallised once from water. Fine single crystals, which were suitable for x-ray diffraction were obtained. Yield: 4.39 g, 73.1%. Four water molecules were found in the X-ray crystal structure, but after being dried in a desiccator, the complex lost two water molecules. Anal. Calcd ($C_{12}H_{12}HfN_2Na_2O_{12}\cdot 2H_2O$): C 22.64%, H 2.53%, N 4.40%. Obsd: C 22.98%, H 2.60%, N 4.25%.

Preparation of Hf(IV)-citrate complex Hf(IV)-citrate complex was prepared with Dengel and Griffith's method [21]. Reaction of the soluble oxychlorides HfOCl2·8H2O with sodium citrate (1:2 metal - ligand ratio) in a solution of 50% (v/v of 30% H_2O_2/H_2O) gave the complex with a possible structure $Na_2[Hf(O_2)_2(citrate)]\cdot H_2O$ because it was said that the pH of the complex formation was 2, a value low enough to suppress hydrolysis of the Hf(IV). The product was characterised by IR and proton NMR.

Preparation of Hf-FBP Hf-Fbp was made from $Na_2[Hf(NTA)_2]$ prepared in physiological buffer (4 mM phosphate, 25 mM $NaHCO_3$, 100 mM NaCl, pH 7.40) using a molar ratio of Hf/*apo*-Fbp= 4 : 1. The mixture of reactants was put into a 1.5 ml Eppendorf tube and was incubated in a 37°C water bath for three hours. The

products were initially purified on a PD-10 column (Amersham), and then using ultrafilters (Millipore Centricon® YM-30) by 0.1 M KCl for six times. Reaction with either 50 or 100 molar equivalents of $Na_2[Hf(NTA)_2]$ gave similar products.

Preparation of Hf-transferrin The powder of human *apo*-transferrin was dissolved in 10 mM Tris buffer, pH 8.0. Then 30-fold molar excess of $Na_2[Hf(NTA)_2]$ was added into the protein solution, the mixture was incubated in a 37 °C water bath for 16 hours. Excess $Na_2[Hf(NTA)_2]$ was removed on a PD-10 column, and then by ultrafiltration using a 30 kDa molecular weight cut off Centricon® (YM-30, Millipore).

Inductively Coupled Plasma Atomic Emission Spectrometry (ICP-AES) Hf-FBP was purified with the procedure above in 10 mM Tris buffer (pH 8.0) instead of 0.1 M KCl. The commercially available hafnium standard atomic absorption solution was diluted with 10 mM Tris buffer. Total protein concentration was determined from the sulphur concentration (1 sulphur per mol protein: Met 308). Values are averages of three determinations on each sample.

^{31}P NMR of Hf-FBP The ^{31}P NMR spectra was recorded at 202.4 MHz at 310 K on a Bruker Advance 600 spectrometer using a 5 mm BBO probe. Data for Hf-FBP were collected using a pulse width of 8.55 μs (60°) at 0.00 dB, relaxation delay 2 s, 16,384 data points and 16,896 transients. The spectral width was 40 ppm and the middle of the spectrum was –2.0 ppm. 85% H_3PO_4 sealed in a capillary tube, which was placed in 90% H_2O and 10% D_2O was used as external standard. The spectra were processed using exponential multiplication (line broadening of 8.0 Hz).

To investigate the binding of phosphate, *apo*-FBP (400 μM) was dissolved in physiological buffer (4 mM phosphate, 25 mM $NaHCO_3$ and 100 mM NaCl, pH 7.4) and the protein solution was incubated at 310 K in a water bath for 12 hours and then a ^{31}P spectrum was recorded at 310 K. To investigate the binding of phosphate to Hf-FBP, a six-fold excess of $Na_2[Hf(NTA)_2]$ solution was added to the *apo*-FBP solution and the mixture was incubated at 310 K for four hours, and then another spectrum was recorded at 310 K.

High Resolution Cation Exchange Chromatography Hf-FBP was prepared as described and then the buffer was changed to 10 mM Tris, pH 8.0. A cation exchange Mono S™ HR 5/5 (Amersham) column was equilibrated with 10 mM Tris buffer (pH 8.0, buffer A). Protein samples were injected onto the column and eluted with a NaCl gradient from low to high salt concentration (0 - 200 mM) consisting of 10 mM Tris, 200 mM NaCl (pH 8.0, buffer B). The experiments were performed on an ÄKTA Basic FPLC (Amersham), the elution rate was 0.5 ml/min and the eluant was monitored at 280 nm.

Protein Crystallisation Crystals of Hf-FBP were grown by the hanging-drop method at 17 °C. Purified Hf-FBP in 0.1 M KCl was mixed with precipitant solution in a 1:1 ratio (v/v, 5 μl/5 μl). The precipitant solution was prepared from 20% PEG 4000 (w/v), 0.4 M imidazole / malate buffer (pH 7.7) and 0.2 M KCl.

4.3 Experimental Results

4.3.1 Crystal Structure of $Na_2[Hf\{N(CH_2COO)_3\}_2]\cdot 4H_2O$

The crystal structure is closely related to that of $(NH_4)_2[Hf(NTA)_2]$ published by Held et. al [22], but in this work, the tetrahydrate complex was prepared. The unit cell is different from the unit cell of the sodium salt prepared here.

The complex is a mononuclear eight co-ordinate complex. The structure is shown in **Figure 4.1**. The hafnium atom is surrounded by two nitrogen atoms and six carboxylate oxygen atoms. The hafnium atom is on a two-fold rotation axis and both co-ordinating NTA ligands are symmetrically equivalent with respect to this axis.

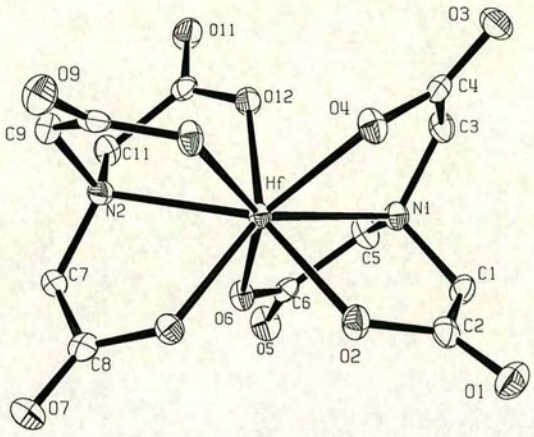

Figure 4.1 The X-ray crystal structure of the anion of $Na_2[Hf(NTA)_2]\cdot 4H_2O$ and atom numbering scheme.

Table 4.2 Bond lengths for $Na_2[Hf\{N(CH_2COO)_3\}_2]\cdot 4H_2O$

Bond	Bond Length (Å)	Bond	Bond Length (Å)
Hf-O(2)	2.122(3)	Hf-O(8)	2.161(3)
Hf-O(4)	2.158(3)	Hf-O(10)	2.134(3)
Hf-O(6)	2.112(2)	Hf-O(12)	2.123(2)
Hf-N(1)	2.436(3)	Hf-N(2)	2.439(3)

Table 4.3 Possible hydrogen bonds (calculated by Platon® 2000)

Type	**Donor- H···Acceptor**	**D-H (Å)**	**H···A (Å)**	**D···A (Å)**	**D-H···A (°)**
Inter	C(11)- H(11A).. O(15)	0.98	2.54	3.49	161.73

(**D:** Donor atom, **A:** Acceptor atom)

4.3.2 Characterisation of Hf(IV)-citrate Complex

Following Dengel and Griffith's suggestion, the formula of the Hf(IV) citrate complex should be $Na_2[Hf(O_2)_2(cit)]\cdot H_2O$ and it was only stable below pH 2. It was suggested that Hf(IV) is six-coordinate (assuming side-on co-ordination for peroxide) or seven coordinate if one molecule of water participates in the coordination sphere [21]. The complex was prepared with their method and characterized by IR with KBr slide and ^1H NMR at pH 7.

The IR spectrum of $Na_2[Hf(O_2)_2(citrate)]\cdot H_2O$ had a peak at 863cm^{-1} assignable to ν(O-O), a peak at 646 cm^{-1} assignable to $\nu_{sym}[Hf(O_2)]$, and a peak at 520 cm^{-1} assignable to $\nu_{asym}[Hf(O_2)]$.

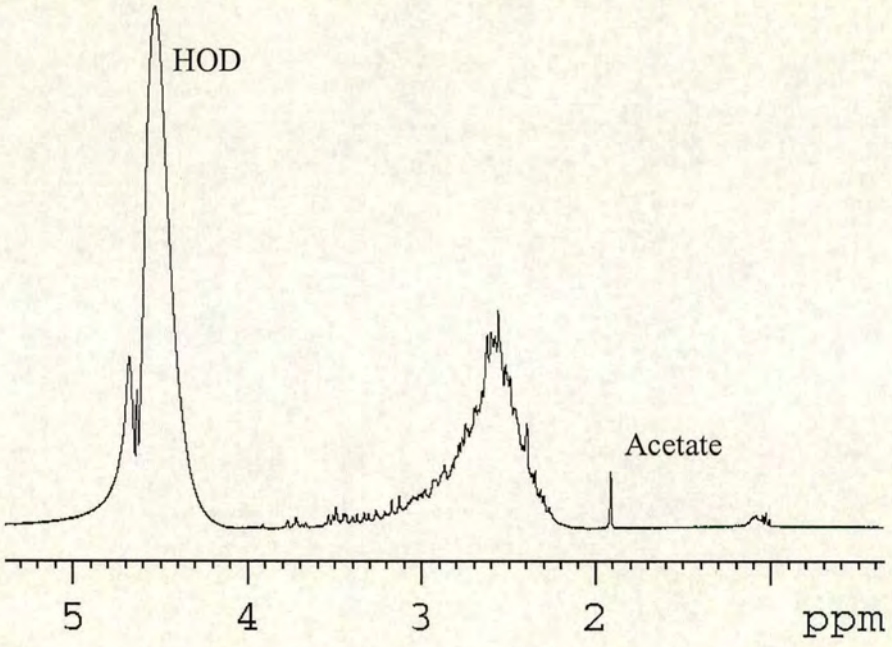

Figure 4.2 ^1H NMR of Hf(IV)-citrate complex in D_2O, pH 7.0 at 25 °C.

In the ^1H NMR spectrum, there was a strong broad peak at *ca.* 2.6 ppm, containing much fine structure, and a series of small peaks with fine structure between 3 and 4 ppm. It seems likely that the Hf(IV)-citrate complex is oligomeric in water at pH 7.0.

4.3.3 Characterisation of Hf-FBP in Solution

UV-Vis difference spectra The UV-Vis spectra of *apo*-FBP and Hf-FBP were recorded separately and the difference spectrum is shown in **Figure 4.3**.

There is a strong peak at 247 nm and a broad peak was found at 294 nm in the UV-Vis difference spectrum. The absorption changes are due to the deprotonation of the tyrosine residues of FBP. Further reactions between Hf(IV) and *apo*-FBP was monitored at 247 nm at different temperature and in the presence of various anions.

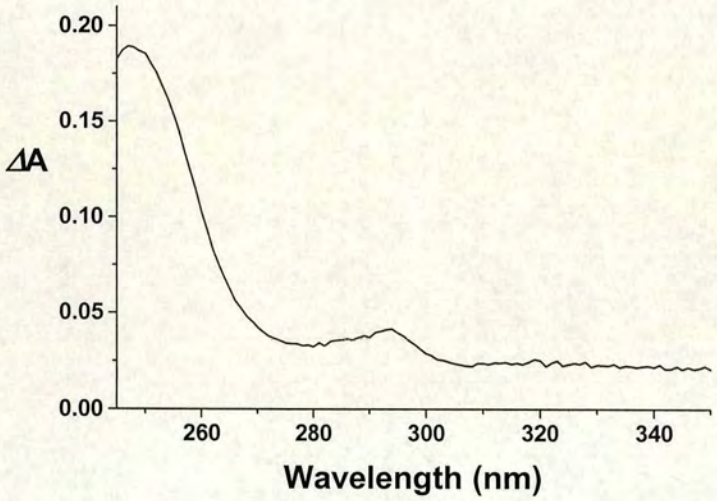

Figure 4.3 The UV/Vis difference spectrum recorded by subtraction of spectrum of *apo*-Fbp for that of Hf-FBP in 10 mM Hepes buffer (pH 7.36), at 25°C.

This reaction (**Figure 4.4**) took more than 20 h to reach the equilibrium under the above conditions. For transferrin, a synergistic anion is involved in metal binding. So, for FBP, the presence of anion may also be helpful for metal to be loaded to *apo*-FBP. The synergistic anion found in the crystal structure of *holo*-Fbp is phosphate, and the synergistic anion of transferrin is carbonate, so these two anions might play an important role in the metal loading process.

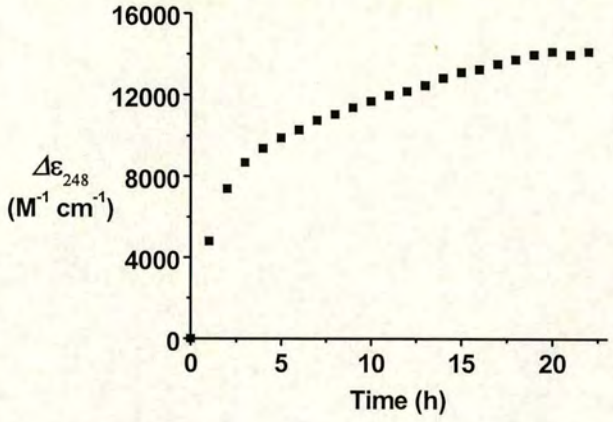

Figure 4.4 Timecourse for reaction of $Na_2[Hf(NTA)_2]$ with *apo*-Fbp in 10 mM Hepes buffer, pH 7.4, at 25°C, molar ratio 1:1 (22.10 μM).

In order to investigate the effects of anion in the metal loading process, further experiments were done in the presence of either carbonate or phosphate, at 25 °C and physiological pH. The reactions were monitored by UV-Vis at ~245 nm (**Figure 4.5**).

The time course diagrams reveal that in the presence of bicarbonate or phosphate, the reaction was accelerated. At 25°C, in the presence of bicarbonate, the reaction was completed within *ca.* 8 h, in the presence of phosphate, the reaction was completed in *ca.* 15 h. Three peaks are present in the UV/Vis difference spectrum of each reaction system (~246 nm, ~283 nm and ~291 nm).

Table 4.4 Time to reach equilibrium and extinction coefficient changes of three reaction conditions for the interaction between $Na_2[Hf(NTA)_2]$ and *apo*-Fbp at 25°C, pH 7.4.

Buffer	**Hepes**	**Hepes and bicarbonate**	**Hepes and phosphate**
$\Delta\varepsilon$ (M^{-1} cm^{-1})	14128	13131	17061
Time (h)	~ 22	~ 8	~ 15

The reaction rate follows the order of Hepes and bicarbonate > Hepes and phosphate > Hepes only. The extinction coefficient change of the reaction in the phosphate containing system was greater than that of the reactions in the non-phosphate containing systems, this suggested that in the presence of phosphate, Hf(IV) can bind differently to *apo*-FBP.

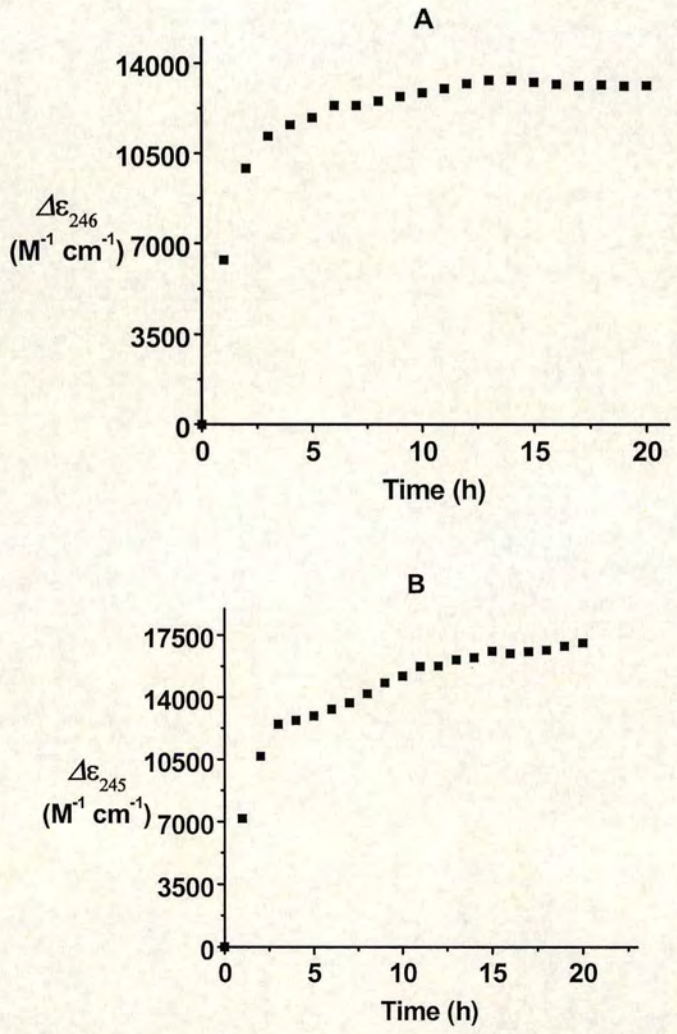

Figure 4.5 Timecourse of reactions of $Na_2[Hf(NTA)_2]$ (22 μM) with *apo*-Fbp (molar ratio 1:1) in 10 mM Hepes buffer in the presence of *(A)* bicarbonate (~22 μM) or *(B)* phosphate (~23 μM), pH 7.4, at 25°C.

Although the reaction was significantly accelerated by bicarbonate or phosphate, it still took at least eight hours to reach equilibrium. Further studies were carried out to investigate the effect of: 1) changing the buffer; 2) increasing the reaction temperature to 37°C.

First of all, the reaction temperature was maintained at 25°C, but the buffer was changed to physiological buffer (100 mM NaCl, 4 mM NaH_2PO_4 and 25 mM $NaHCO_3$, pH 7.4), which contains a high excess of both phosphate and bicarbonate. The reaction reached equilibrium within 50 min (**Figure 4.6**).

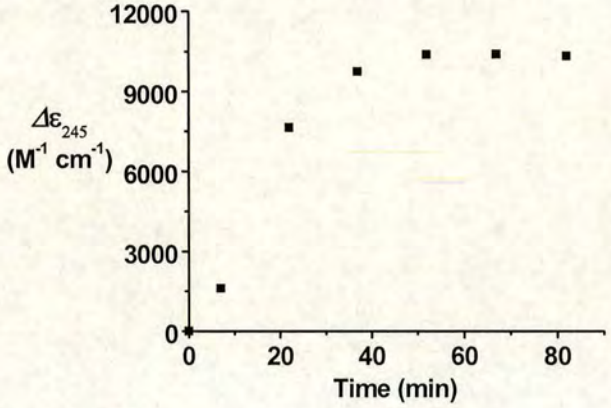

Figure 4.6 Timecourse for reaction of $Na_2[Hf(NTA)_2]$ with *apo*-Fbp (22 μM) in physiological buffer, 25°C, pH 7.4, $Na_2[Hf(NTA)_2]$ / *apo*-Fbp = 2:1.

The difference spectrum for this reaction was always the same as the difference spectrum of the reaction in Hepes or Hepes and bicarbonate. Three peaks were found at 318 nm, 245 nm and 290 nm.

Secondly, the buffer was Hepes only, without bicarbonate or phosphate, and the pH was kept at 7.4, but the reaction temperature was increased to 37 °C. The reaction was also accelerated, and reached equilibrium within 2.5 h (**Figure 4.7**).

This experiment reveals that increasing the temperature accelerates the reaction. At 25°C, it took *ca.* 22 hours to complete the reaction, $\Delta\varepsilon_{248} \cong 14000\ M^{-1}\ cm^{-1}$; whereas

at 37°C, the reaction was completed within 1.6 hours, $\Delta\varepsilon_{248} \cong 26000\ M^{-1}\ cm^{-1}$. This suggested that at higher temperature, more tyrosine residues were deprotonated than at lower temperature. Two peaks were found from the difference spectrum, one was the strong sharp peak at 248 nm, and the other was a small broad peak at 298 nm.

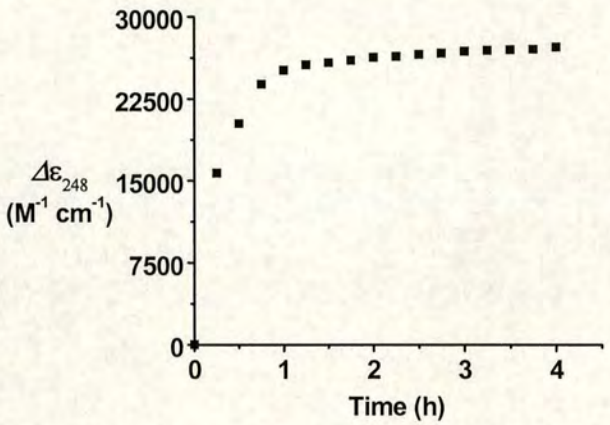

Figure 4.7 Timecourse curve for the reaction between $Na_2[Hf(NTA)_2]$ and *apo*-Fbp (22 μM) in 0.1 M Hepes buffer at 37°C, pH 7.4, $Na_2[Hf(NTA)_2]$ / *apo*-Fbp = 2:1.

Hence, to optimise the reaction conditions, the reaction was studied in the presence of both bicarbonate and phosphate and at 37°C. To investigate the influence of Hepes, the reaction was investigated in two systems: *1)* Hepes, bicarbonate and phosphate (**Figure 4.8**), *2)* NaCl, bicarbonate and phosphate (physiological buffer, **Figure 4.9**).

These two experiments show that with the combined anions (bicarbonate and phosphate) and increased temperature, the reaction is completed very quickly. In the Hepes buffer, the reaction reached equilibrium in *ca.* 45 minutes, $\Delta\varepsilon \approx 34{,}000\ M^{-1}\ cm^{-1}$, in the physiological buffer, the reaction reached equilibrium within 15 minutes, $\Delta\varepsilon \approx 10{,}500\ M^{-1}\ cm^{-1}$. The difference of $\Delta\varepsilon$ in two systems suggested that in Hepes buffer, Hf(IV) may bind more strongly to *apo*-FBP or more tyrosine residues were deprotonated for metal binding.

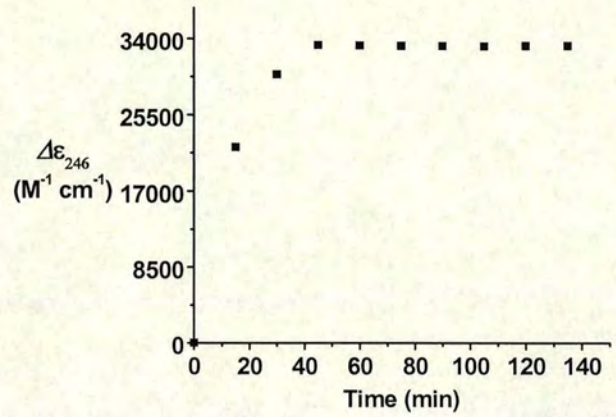

Figure 4.8 Timecourse for the reaction of $Na_2[Hf(NTA)_2]$ with *apo*-Fbp (22 μM). The buffer was 100 mM Hepes, 4 mM NaH_2PO_4 and 25 mM $NaHCO_3$ at 37°C, pH 7.4, $Na_2[Hf(NTA)_2]$ / *apo*-Fbp = 2:1.

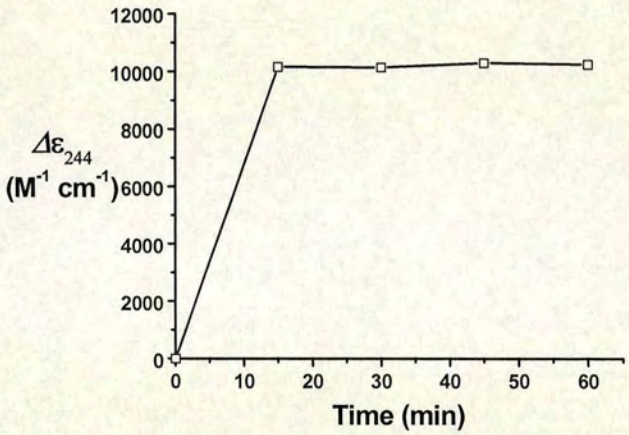

Figure 4.9 Timecourse for the reaction of $Na_2[Hf(NTA)_2]$ with *apo*-Fbp (22 μM), $Na_2[Hf(NTA)_2]$ / *apo*-Fbp = 2:1. The buffer was physiological buffer (100 mM NaCl, 4 mM NaH_2PO_4 and 25 mM $NaHCO_3$) pH 7.4, at 37°C. The points are connected by straight lines without fitting.

If Hf-citrate was used as starting material to react with *apo*-FBP, whatever the buffer, the reaction reached equilibrium within 20 minutes.

To determine the stoichiometry of Hf-FBP, *apo*-FBP was titrated with Hf(IV), and the reaction was monitored at 247 nm (**Figure 4.10**).

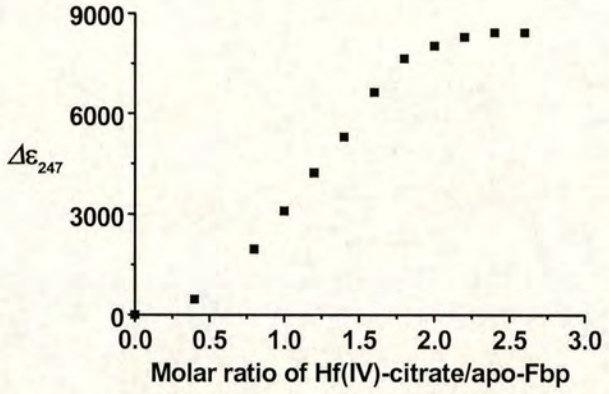

Figure 4.10 Hf(IV) was loaded to *apo*-FBP by titration at stepwise Hf(IV) : *apo*-FBP molar ratios. The reaction was monitored at 247 nm in 10 mM Hepes, at 25 °C, pH 7.4. Each sample was left 15 min to equilibrate before the absorbance was determined. Points were displayed without fitting.

The titration experiment suggested that more than one Hf(IV) ions bind per *apo*-FBP molecule although only one ferric iron binds to FBP in wild-type *holo*-FBP. To confirm this result, Hf-FBP sample was analysed with ICP-AES.

For all experiments below, Hf-FBP was prepared with $Na_2[Hf(NTA)_2]$ in physiological buffer.

Quantitative elemental analysis by ICP-AES The hafnium, phosphorus and sulphur contents were determined at the same time. The result showed that the molar ratio of Hf : *apo*-FBP was 4.03 ± 0.10 and the molar ratio of P : *apo*-FBP was 1.39 ± 0.04.

^{31}P NMR of Hf-FBP The result from ICP-AES analysis revealed that phosphate is involved in binding to Hf-FBP. From UV-Vis studies, it was known that both phosphate and carbonate play important role in Hf(IV) binding to *apo*-FBP.

Hence, ^{31}P and ^{13}C NMR were used to investigate the binding of phosphate and carbonate to Hf-FBP.

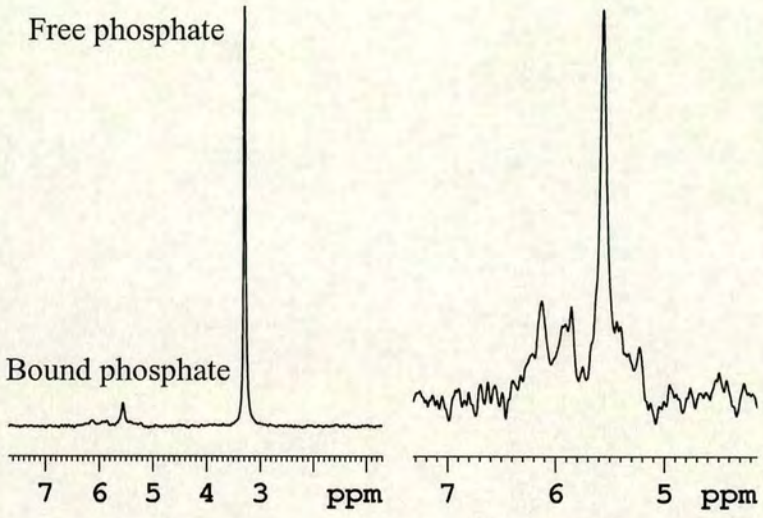

Figure 4.11 ^{31}P NMR spectrum shows the binding of phosphate to Hf-Fbp prepared from physiological buffer. The left spectrum is the whole spectrum, the right one is the spectrum expanded to show the bound phosphate peak.

The spectrum (**Figure 4.11**) showed that besides the free phosphate peak (3.28 ppm), new peaks were shifted downfield by 2-3 ppm. The main bound phosphate peak was found at 5.55 ppm, also, some smaller peaks were found around 6 ppm. This result provides evidence that phosphate can bind to hafnium in FBP. The multiple peaks mean that there are several phosphate binding environments in Hf-FBP. In the ^{13}C NMR spectrum, besides the free bicarbonate peak, no bound bicarbonate peak was found.

Characterisation of Hf-FBP by high resolution chromatography Purified Hf-FBP in 10 mM Tris (pH 8.0) was loaded into a cation exchange Mono S™ HR 5/5 (Amersham) column. The elution rate was 0.5 ml/min. The chromatogram is shown in **Figure 4.12**. The peaks relate to the different forms of Hf-FBP which have

different charges. This spectrum indicated that the Hf-FBP is heterogeneous in solution; there were at least five forms of Hf-FBP in the solution although under the same conditions, only a single peak was found for *apo*-FBP.

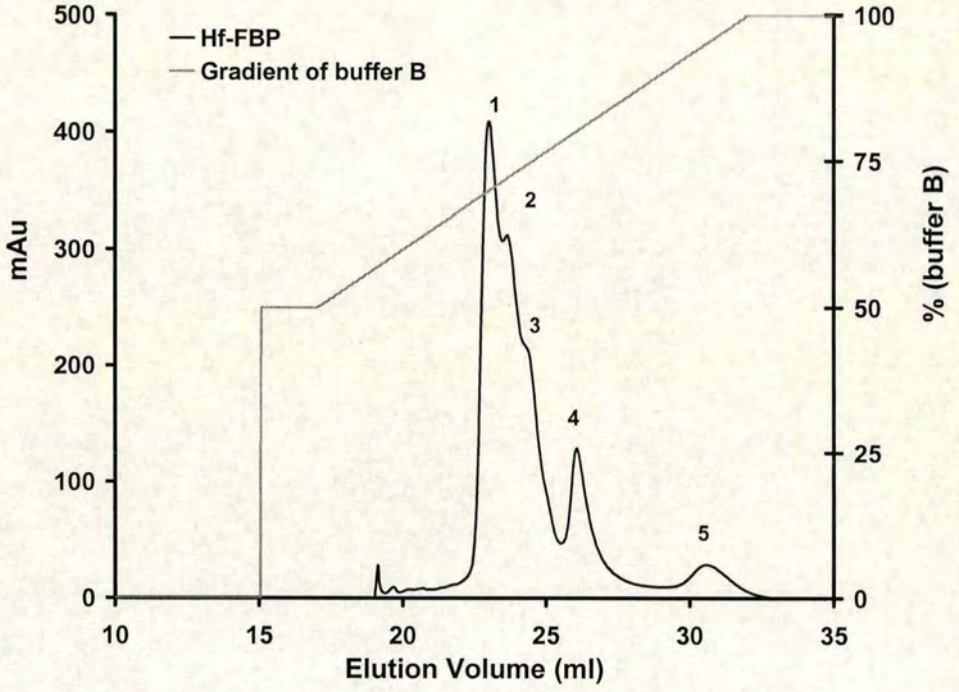

Figure 4.12 Characterisation of Hf-FBP by chromatography on a MonoS™ HR 5/5 (Amersham) column. The left axis shows the absorbance of Hf-FBP at 280 nm, the right axis is the percentage of the buffer B (10 mM tris, 200 mM NaCl, pH 8.0). The grey line indicates the gradient of the buffer B applied during the elution process.

The interaction between Hf(IV) and *holo*-Fbp was also studied by UV-Vis spectrometry. Hf(IV)-citrate complexes were incubated with *holo*-FBP in a 1:1 molar ratio, the reaction was monitored at 480 nm.

The broad peak at 480 nm is the specific LMCT band of *holo*-Fbp. When *holo*-Fbp reacted with Hf(IV)-citrate, the decay of this peak means that Fe(III) was displaced from the specific ferric ion binding site (**Figure 4.13**). When the molar ratio between Hf and Fe was 1 : 1, 47% of the bound Fe was replaced by hafnium (confirmed with

ICP-AES). Conversely, when $Na_3[Fe(NTA)_2]$ was mixed with Hf-FBP in a 1:1 molar ratio, hafnium was displaced by iron from Hf-FBP rapidly.

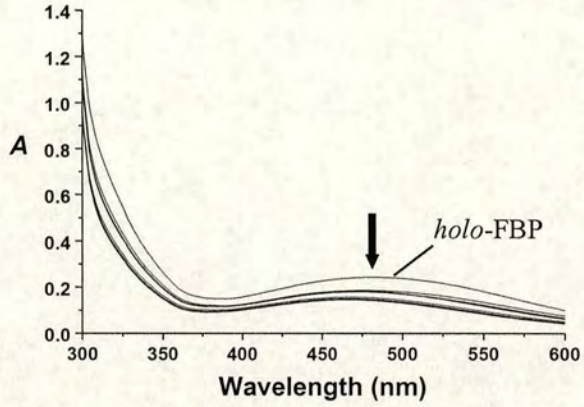

Figure 4.13 UV/Vis spectrum of *holo*-Fbp on reaction with $Na_2[Hf(NTA)_2]$ in physiological buffer, pH 7.4 at 37 °C. The spectra were recorded at 5 minute time intervals. The band at 480 nm is the LMCT band of *holo*-Fbp.

4.3.4 Crystal Structure of Hf-FBP

The data for the crystal of Hf-FBP which contains 4.8 Hf(IV) per mole protein was collected by Dr. Dmitriy Alexeev (ICMB, University of Edinburgh) at 1.7 Å resolution and the structure was solved by him by the molecular replacement phasing method. There are nine molecules (labelled A-I) in the asymmetric unit cell (space group $P3_2$). The crystal was twinned, but the structure was finally solved to R_{cryst}=16.5% and R_{free}=26.4%.

The arrangement of nine molecules was complex. The whole unit cell and the stacks of nine protein molecules in the asymmetric unit cell are shown in **Figure 4.14** and **Figure 4.15**. Nine protein molecules are labelled with **A-I** and individually coloured.

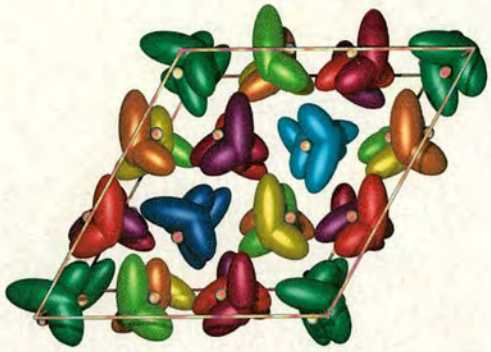

Figure 4.14 The complete unit cell. Space group $P3_2$, with the *z*-axis pointing towards the viewer.

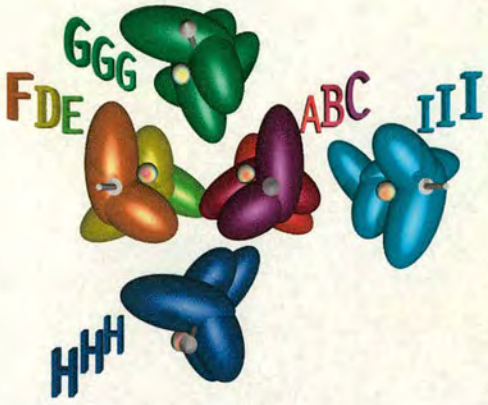

Figure 4.15 Stacks of molecules **A-I** in the asymmetric unit along the z-axis.

FBP has two hinged domains (α / β domains). In **Figures 4.14** and **4.15**, intersecting ellipsoids represent the two hinged domains of each protein molecule, the N-terminal domain is bigger. Small metallic balls in the middle indicate metal clusters.

In **Figure 4.15**, different orientations of the stacks along the *z*-axis are indicated by the directions of arrows running through the hinge area of the protein molecule (up for **A**, **B**, **C**, **G**, **H**, down for **D**, **E**, **F**, **I**). Molecules in each stacks of **G**, **H** and **I** molecules with the same colour are identical because they lie on a crystallographic three-fold screw axis (not shown). Both (**A**, **B**, **C**) and (**F**, **D**, **E**) are made of similar, but not identical molecules, which are therefore differently coloured. Individual molecules in these stacks are related by approximate non-crystallographic three-fold screw symmetry and have slightly different conformations. The stack **A**, **B** and **C** (arrow up) and the stack **F**, **D** and **E** (arrow down) are anti-parallel.

In *holo*-FBP, the hinge between domains is closed and only one Fe(III) is octahedrally coordinated to His9 and Glu57 from the N-terminal domain and di-tyrosyl Tyr195-Tyr196 from the hinge area, a water molecule and a phosphate as a synergistic anion bound to the C-terminal domain [23]. In *apo*-FBP the domain is open and mono-Fe(III) binding is accompanied by a hinge closure of approximately

26° [24]. In Hf-FBP, Hf(IV) clusters bind to FBP in the metal-binding site. The interdomain hinge remains open and the side chains of His9 and Glu57, previously identified as Fe(III) ligands in closed mono-Fe-FBP, are swung away from the metal binding site. The hinge angles of nine molecules (**A-I**) in Hf-FBP crystal are various and on average only 5.5° smaller than that of *apo*-FBP. The hinge angle difference in the most closed molecule **D** and the most open molecule **H** is 8.4°. The group of three molecules **G**, **H** and **I** have a wider hinge angle than other molecules.

The crystal environment of the metal-binding pocket among molecules is distinct, as the structures of the metal cluster at the metal binding site are different. Three main groups of hafnium clusters were found in the crystal, one is a trinuclear cluster with phosphate binding, and the others are pentanuclear clusters with and without phosphate binding.

Figure 4.16 The positively charged molecular surface around the metal pocket (calculated by GRASP [25], as indicated in blue.

Unexpectedly for cation binding, the surface of the Hf(IV) binding pocket is positively-charged (as shown in **Figure 4.16**). Besides bonded to the phenolate oxygens of Tyr195 and Tyr196, Hf(IV) ions are not contact with any of the protein atoms directly. Negatively-charged oxygen atoms bound Hf(IV) ions and bridge them in a manner similar to the structure of HfO_2 [26] (**Figure 4.19**).

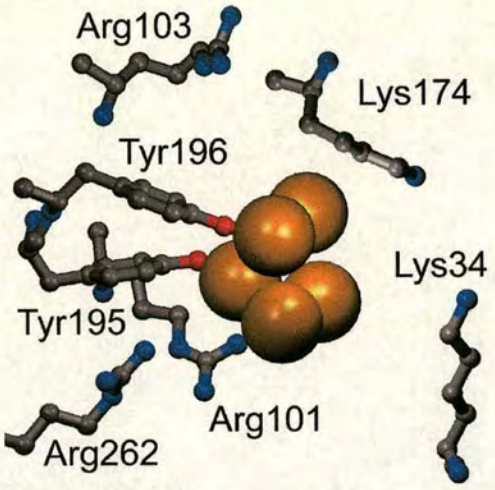

Figure 4.17 Lys and Arg residues in the vicinity of the Hf ions (gold spheres) in the cluster binding pocket. Bridging oxygens and the phosphate are omitted for clarity. Arg101 is completely conserved in all FBP sequences.

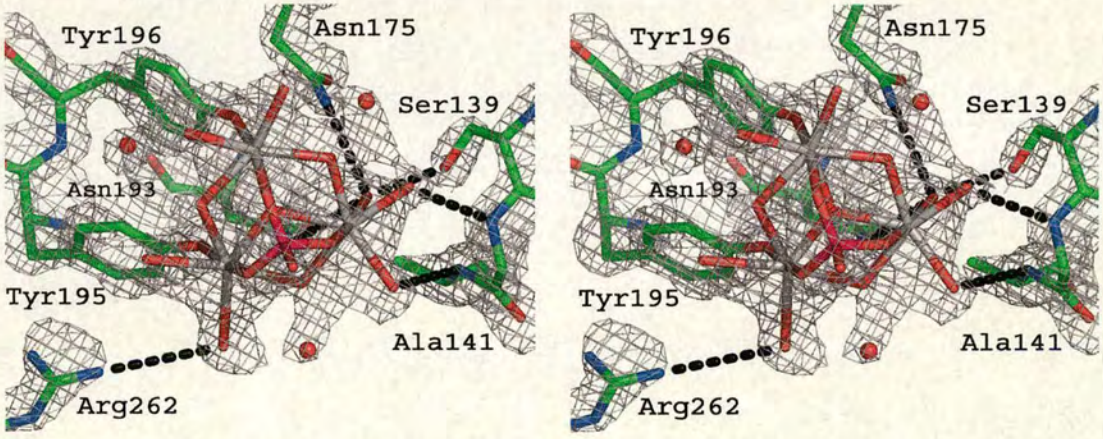

Figure 4.18 Stereo view of SigmaA [27]-weighted ($2F_o$-F_c) electron density map for the smallest cluster (D) calculated with CNS [28]. The small unconnected red balls represent water molecules. The metal ions are coordinated to the protein through the phenolate oxygens of Tyr195 and Tyr196.

The molecule **D** represents the group with a trinuclear cluster. It is the most closed and contains the smallest cluster of only three well-ordered metals Hf1, Hf2 and Hf3

(**Figure 4.18**) in the crystal. Hf1 is coordinated to Tyr196, Hf2 to Tyr195, and Hf3 to Hf1 and Hf2 through the bridging oxygens (**Figure 4.19a**). This trinuclear cluster is capped by a phosphate, which faces outward from the binding pocket. Each metal co-ordinates to seven oxygens with pentagonal bipyramidal geometry. The five equatorial oxygens are oxides (or hydroxides), and the axial oxygens are from tyrosinate (or water for Hf3) and phosphate. The Hf···Hf distances range from 3.6 Å to 3.8 Å, and the Hf···O distances range from 1.9 Å to 3.0 Å with the Hf-tyrosinate bonds being the shortest. The Tyr195-Tyr196 O···O distances of 4.03 Å to 4.48 Å are significantly longer than that in *holo*-FBP (3.01 Å)[23], where both tyrosines are bound to a single Fe(III). The overall calculated charge on the first coordination shell is –7 (if all four bridging oxygens are oxide). The net positive surface charge on the metal-binding cleft (**Figure 4.16**) may facilitate formation of the protein-cluster complex. This assembly of trinuclear cores of Hf(IV) ions is common in inorganic complexes containing alkoxide, aryloxide, hydroxide and oxide ligands [29, 30].

Molecules **A**-**F** except molecule **D** contain pentanuclear clusters. Compared with the trinuclear clusters, the bound phosphate is replaced by an oxo-metal ion (Hf4, **Figure 4.19*b***). As in molecule D, Hf1, Hf2 and Hf3 ions are fully ordered. The additional two ions Hf4 and Hf5 point into the solvent and are disordered. High electron density peaks (>10 σ) and strong anomalous signals (>3 σ) confirm that they are hafnium ions. The high temperature factors (B-factor = 95 $Å^2$) indicate that they are mobile. Hf5 forms an oxygen-bridged triangle with Hf1 and Hf4, similar to the triangle Hf1-Hf2-Hf3 of cluster in molecule **D** but without central oxygen. Both Hf4 and Hf5 are octahedrally coordinated to six oxygens. Molecules **A**-**C** have similar hinge angles and crystal contacts and contain similar metal clusters. The clusters in molecules **E** and **F** are different from the clusters in molecules **A**-**C** by an even higher mobility/disorder of Hf5.

Clusters in molecules **G**-**I** are also pentanuclear clusters but with an additional phosphate (**Figure 4.19*c***). Unlike the cluster in molecule **D**, the phosphate bridges Hf1 to Hf4 and Hf5 in molecules **G**-**I**. In contrast to molecules **A**, **B**, **C**, **E** and **F**, Hf4 and Hf5 in molecules **G**-**I** become well ordered (*B*-factor = 42 $Å^2$). The other pair of

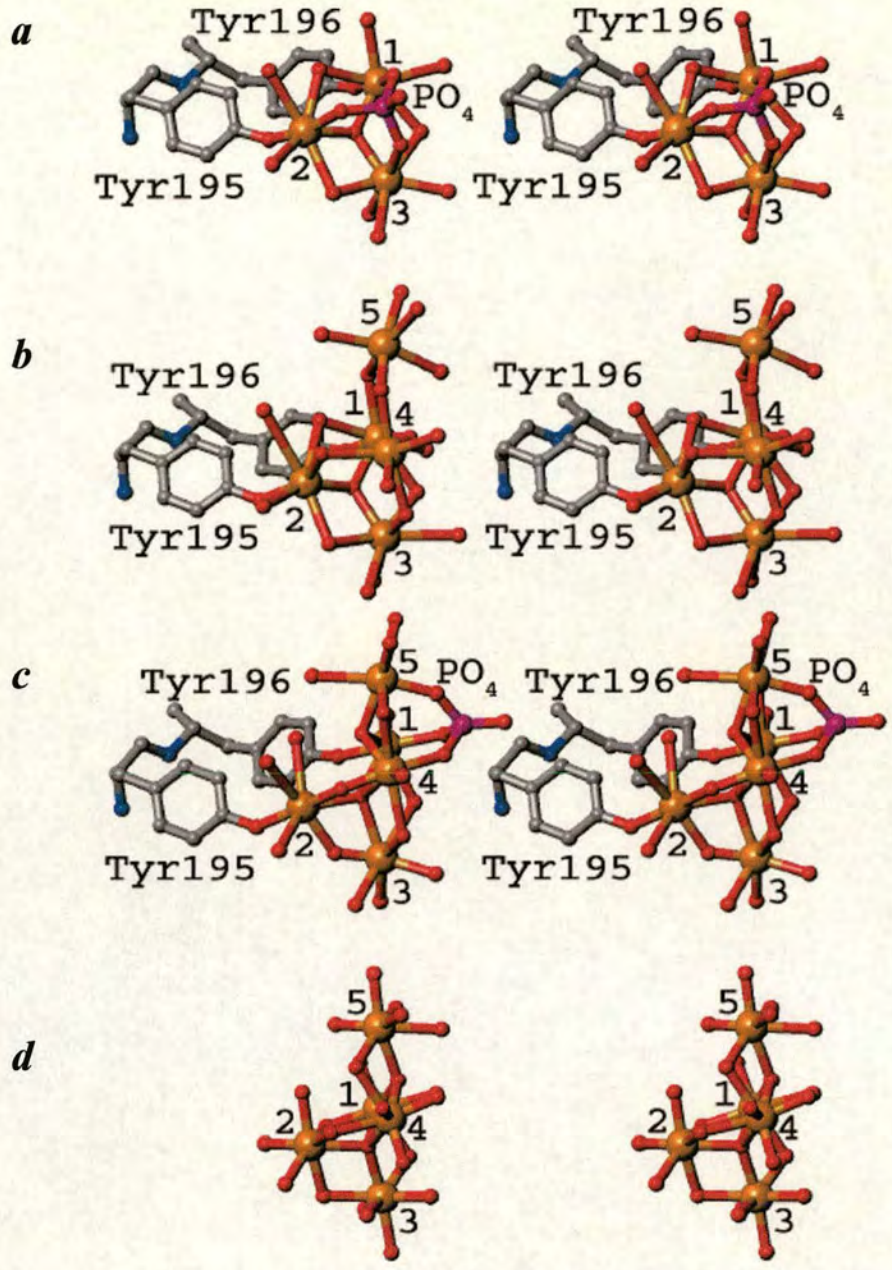

Figure 4.19 Stereo views of Hf coordination in the protein nanoclusters and mineral HfO_2. ***a,*** The smallest cluster in molecule **D**. Hf(IV) ions are gold and oxygen ions are red. Phosphate caps three Hf(IV) ions. ***b***, The metal clusters in molecule **A** (clusters in **B**, **C**, **E**, **F** are similar). This cluster contains five Hf(IV) ions and no bound phosphate. ***c***, Cluster in molecule **G** (clusters in **H** and **I** are similar). The Hf1, Hf4 and Hf5 ions are capped by phosphate. ***d***, A fragment of the crystal structure of mineral HfO_2 [26]. Molscript [31] was used to generate (*a-d*).

ions, Hf2 and Hf3, are well ordered in molecules A-F, and become mobile (*B*-factor = 92 $Å^2$) in molecules **G-I** although Hf2 (bound to Tyr195) and Hf3 are the most buried in the binding pocket. The phosphate capping the cluster Hf1-Hf4-Hf5 is identical to that of Hf1-Hf2-Hf3 in molecule **D**, but situated further away from the bottom of the metal binding pocket.

Positional disorder seems to be associated with phosphate binding and not with the tyrosyl ligands. The size of the cluster correlates with the hinge-angle opening, the most closed molecule **D** contains the smallest cluster and the larger clusters are found in the more open molecules **G-I**.

4.4 Discussion

FBP is highly conserved among various pathogenic bacteria, so it is a potential target for broad-spectrum antibacterial drug design. Hetero-metal complexes can play the role of metalloantibiotics to inhibit the iron-uptake process which is essential for the survival of those pathogens. This targeting pathway could counter the rapidly growing problem of anti-microbial drug resistance.

Experiments performed in this chapter reveal that Hf(IV) can bind to *apo*-FBP specifically. Whatever the starting Hf(IV) complex, $Na_2[Hf(NTA)_2]$ or Hf-citrate, the UV-Vis difference spectra are the same. However, when Hf(IV) was loaded to *apo*-FBP by Hf-citrate, the reaction reached equilibrium with 20 minutes in any buffer and at lower temperature (25 °C). When $Na_2[Hf(NTA)_2]$ was used to load Hf(IV) to *apo*-FBP, the reaction rate was influenced dramatically by the components of buffer and temperature. The best loading conditions for $Na_2[Hf(NTA)_2]$ were found at 37 °C, in physiological buffer (100 mM NaCl, 4 mM phosphate, 25 mM bicarbonate, pH 7.4), where the reaction can reach the equilibrium within 30 minutes. New bands appeared at ~245 nm and ~290 nm which are typical of phenolate groups (π-π^* transitions) generated by binding of Hf(IV) to Tyr195 and Tyr196 in the iron-binding site of FBP.

The result from the titration experiment monitored by UV-Vis appeared to indicate that more than one Hf(IV) ions bind to FBP, but the ICP-AES result reveals that there are more than two hafnium ions bound to one protein molecule. The crystal structure gives a clear answer for this mismatch. There are two hafnium ions bound to Tyr195 and Tyr196 separately, which deprotonates the Tyr residues and causes the UV absorption change. Further hafnium ions form clusters via oxo bridges with hafnium ions bound to Tyr, and do not cause further deprotonation, so no further absorption change is monitored in this procedure.

To determine which anion is involved in binding to Hf-FBP, ^{13}C and ^{31}P NMR was used. Hf-FBP was dissolved in physiological buffer, and ^{13}C and ^{31}P spectra were recorded. In the ^{13}C spectrum, besides a free carbonate signal, no new peak appeared. However, in the ^{31}P spectrum, new peaks, shifted downfield from free phosphate by 2-3 ppm were observed. This evidence matches for phosphate binding agrees with the interpretation of the X-ray structure. The shape of the electron density of an anion in the crystal structure, which is tetrahedral, and the model of phosphate fits the electron density map very well, so the anion of Hf-FBP was determined as phosphate. Nevertheless, the crystal structure of Hf-FBP reveals that phosphate is not essential for Hf(IV) ions to bind to *apo*-FBP. Some molecules of Hf-FBP in the asymmetric unit cell has no phosphate binds to the Hf(IV)-FBP complex.

Five peaks were found in the high-resolution ion-exchange chromatogram, which shows that there are multiple species of Hf-FBP present in solution. This is also found in the crystal structure of Hf-FBP, the nine molecules in the asymmetric unit cell can be classified in three groups, trinuclear clusters with phosphate bound, and pentanuclear clusters with and without phosphate. When ligands of $Na_2[Hf(NTA)_2]$ were replaced by *apo*-FBP, without the protection of the chelating ligand and in the presence of water, hafnium forms various clusters in the metal-binding site of FBP.

Open transferrin conformations are known with a single bound Fe(III) ion [32, 33, 34]. Domain closure was not reported for mammalian transferrin treated with Hf-NTA in solution [35]. When human *apo*-transferrin was treated with a 30-fold molar

excess of $Na_2[Hf(NTA)_2]$ under similar condition as used for Hf-FBP preparations, it was found in the present work by ICP-AES that the Hf:protein:phosphate ratio was 3.5:1:1.1, similar to FBP. This suggests that at least the N-lobe, which is wider open in the *apo* protein, binds Hf clusters. The cleft of the N-lobe of transferrin can open some 20° wider [36] than FBP and can contain more phosphate-binding sites [34], potential anchors for oxo-metal clusters. This, together with the high affinity of FBP for multimetal clusters, suggests that the N-lobe of transferrins could also bind metal clusters. The C-lobe may not be able to open wide enough to bind metal clusters, and this may be relevant to the functional difference between two lobes.

It seems that cluster binding occurs as readily as mononuclear binding, which requires a conformational transition plus a synergistic anion (phosphate or carbonate). Helper anions are not necessary for cluster binding: oxygens of oxo clusters take the place of the synergistic anion in the positively-charged binding site. The metal binding cleft of Hf-FBP is open.

Native *holo*-FBP contains a single metal ion anchored to two tyrosines in a closed inaccessible binding pocket and cannot take up further metal ions. The studying of Hf-FBP revealed that each tyrosine can bind to a separate metal ion. The two tyrosine residues bring these metal ions into close proximity, simulating further growth of cluster. Oxygens from the cluster replace the synergistic anion. Hence, the metal uptake pathway may also include bound multinuclear intermediates.

References

1 Lide, D.R. *CRC Handbook of Chemistry and Physics*, **72nd edition,** p4 (1992).

2 http://www.webelements.com (1993-2003).

3 Greenwood, N.N., and Earnshaw; *Chemistry of the Elements*, **First edition**, p1111 Oxford **(1984)**.

4 Cotton and Wilkinson, *Advanced Inorganic Chemistry* **Fourth Edition,** New York, 823 – 831 (1972).

5 Page, E., and Wass, S., *Coord. Chem. Rev.* **152**, 411 (1996).

6 Intorre, B. I., Martell, A. E., *J. Am. Chem. Soc.*, **82,** 358 (1960).

7 Held, P., Listl, B., Tillmanns E., Ahrweiler S., Hellwig H., Bohaty L., *Z. Kristallogr.* **215**, 65 (2000).

8 Tranqui, P.D., Boyer, P., Laugier, J., Vulliet, P., *Acta Cryst.*, **B33,** 3126 (1977).

9 Dengel, A., and Griffith, W. P., *Polyhedron* **8,** 1371 (1989).

10 Mohammadi, S., Esposito, M., Cucu, M., Ericson, L. E., Thomsen, P. *J. Mater. Sci.* **12,** 603 (2001).

11 Enomoto, S., Yanaga, M., Hirunuma, R., Endo, K., Ambe, S., Ambe, F., *Kidorui* **26**, 406 (1995).

12 Sotogaku, N., Endo, K., Hirunuma, R., Enomoto, S., Ambe, S., Ambe, F., *J. Radioanal. Nuc. Chem.* **239**, 429 (1999).

13 Taylor, D. M., Seidel, A., Doerfel, H., *Int. J. Nucl. Med. Biol.* **12**, 387 (1985).

14 Taylor, D. M., Lehmann, M., Planas-Bohne, F., Seidel, A., *Radiation Research* **95,** 339 (1983).

15 Then, G.M., Appel, H., Duffield, A.J., Taylor, D.M., Thies., W.G., *J. Inorg. Biochem.*, **27**, 255 (1986).

16 Becker, G., Appel, H., Neu, M., Schwab F.J,; Thies W.G., *Hyperfine Interactions*, **80**, 1161 (1993).

17 Huchens, T.W., Yip, T.Y., *J. Chromatogr.*, **536**, 1 (1991).

18 Aisen, P., Editor(s): Jacobs, A., Worwood, M., *Iron Biochem. Med.* **2**, 87 (1980).

19 Schwab, F.J., Appel, H., Mason. A.B., Thies W.G., *BioMetals*, **6**, 193 (1993).

20 Nowalk, A. J., Tencza, S. B., Mietzner T.A., *Biochemistry* **33**, 12769 (1994).

21 Dengel, A., and Griffith, W. P., *Polyhedron*, **8**, 1371 (1989).

22 Held, P., Listl, B., Tillmanns E., Ahrweiler S., Hellwig H., Bohaty L. *Z. Kristallogr.* **215**, 65 (2000).

23 Bruns, C.M., Nowalk, A. J., Arvai, A. S., Mctigue, M. A., Vaughan, K. G., Mietzner, T. A., Mcree, D. E., *Nat. Struct. Biol.* **4**, 919 (1997).

24 Bruns, C. M. Anderson, D. S., Vaughan, K. G., Williams, P. A., Nowalk, A. J., McRee, D. E., Mietzner, T. A., *Biochemistry* **40**, 15631 (2001).

25 Nicholls, A., Sharp, K.A. & Honig, B., *Proteins* **11**, 281 (1991).

26 Ruh,R. & Corfield, P.W.R., *J. Am. Ceram. Soc.* **53**, 126 (1970).

27 Read, R.J., *Acta Crystallogr.* **A 42**, 140 (1986).

28 Brunger, A.T., *Acta Crystallogr.* **D 54**, 905 (1998).

29 Evans, W.J., Ansari, M.A. & Ziller, J.W., *Polyhedron* **17**, 869 (1998).

30 Starikova, Z.A., Turevskaya, E. P., Kozlova, N. I., Turova, N. Ya., Berdyev, D. V., Yanovsky, A. I., *Polyhedron* **18**, 941 (1999).

31 Kraulis, P.J., *J. Appl. Crystallogr.* **24**, 945 (1991).

32 Mizutani, K., Yamashita, H., Kurokawa, H., Mikami, B. & Hirose, M., *J. Biol. Chem.* **247**, 10190 (1999).

33 Khan, J.A., Kumar, P., Srinivasan, A., & Singh, T.P., *J. Biol. Chem.* **276**, 36817 (2001).

34 Kuser, P., Hall, D. R., Haw, L., Neu, M., Evans, R. W., Lindley, P. F., *Acta Crystallogr.* **D 58**, 777 (2002).

35 Grossmann, J. G., Neu, M., Evans, R. W., Lindley, P. F., Appel, H., Hasnain, S. S., *J. Mol. Biol.* **229**, 585 (1993).

36 Jeffrey, P.D., Bewley, M. C., MacGillivray, R. T. A., Mason, A. B., Woodworth, R. C., Baker, E. N., *Biochemistry* **37**, 13978 (1998).

Chapter 5 Phosphate-Vanadate Analogy in FBP

5.1 Introduction

Vanadium has an atomic weight of 50.941 and its atomic number is 23. The electronic configuration is $[Ar]3d^3 4s^2$, and atomic radius (empirical) is 134 pm [1].

The discovery of vanadium is attributed to Andres Manuel del Rio (a Spanish mineralogist) who prepared a number of salts from a material contained in "brown lead" in Mexico City around 1803. Unfortunately, the French chemist Collett-Desotils incorrectly declared that del Rio's new element was only impure chromium. Del Rio thought himself to be mistaken and withdrew his claim. The element was rediscovered in 1830 by the Swedish chemist Nils Gabriel Sefström who named it after the Norse goddess Vanadis, the goddess of beauty and fertility because of its beautiful multicolored compounds. It was isolated in nearly pure form by Roscoe, in 1867, who reduced the chloride with hydrogen. Vanadium of 99.3% to 99.8% purity was not produced until 1922. Vanadium is found in about 65 different minerals among which are carnotite, roscoelite, vanadinite, and patronite, important sources of the metal. Vanadium is also found in phosphate rock and certain iron ores, and is present in some crude oils in the form of organic complexes. It is also found in small percentages in meteorites. Natural vanadium is a mixture of two isotopes, ^{50}V (0.24%) and ^{51}V (99.76%). ^{50}V is slightly radioactive, having a half-life of $> 3.9 \times 10^{17}$ years. Nine other unstable isotopes are recognised. Vanadium and most of its compounds are toxic and should be handled with care. The coordination chemistry of vanadium is summarised in **Table 5.1**.

Table 5.1 Oxidation states and stereochemistry of Vanadium [2].

Oxidation state	Coordination number	Geometry	Examples
V^{-1}, d^6	6	Octahedral	$[V(CO)_6]^-$, $Li[V(bipy)_3]\cdot 4C_4H_8O$
V^0, d^5	6	Octahedral	$[V(CO)_6]$, $V(bipy)_3$, $V[C_2H_4(PMe_2)_2]_3$
V^I, d^4	6	Octahedral	$[V(bipy)_3]^+$
		Tetragonal pyramidal	η^5-$C_5H_5V(CO)_4$
	7	Monocapped octahedral	$[V(CO)_3(PMe_3)_4]^+$, $V(CO)_2(dmpe)_2Cl$
V^{II}, d^3	4	Almost planar	$[Li(THF)]_2V(2,6\text{-diisopropylphenolate})_4$
	5	Square Pyramidal	$(2,6\text{-}Ph_2C_6H_3O)_2V(py)_3$
	6[a]	Octahedral	$[V(H_2O)_6]^{2+}$, $[V(CN)_6]^{4-}$
V^{III}, d^2	3	Planar	$V[N(SiMe_3)_2]_3$, $V[CH(SiMe_3)_3]_3$
	4	Tetrahedral	$[VCl_4]^-$
	5	Trigonal bipyramidal	*trans*-$VCl_3(SMe_2)_2$, $VCl_3(NMe_3)_2$
	6[a]	Octahedral	$[V(NH_3)_6]^{3+}$, $[V(C_2O_4)_3]^{3-}$, VF_3
	7	Pentagonal bipyramidal	$K_4[V(CN)_7]\cdot 2H_2O$
V^{IV}, d^1	4	Tetrahedral	VCl_4, $V(NEt_2)_4$, $V(CH_2SiMe_3)_4$
	5	Tetragonal pyramidal	$VO(acac)_2$, $PCl_4^+VCl_5^-$
		?	$[VO(SCN)_4]^{2-}$
		Square pyramidal	$[V_4O_4(OH)_2(PhPO_3)_4]^{2+}$
		Trigonal bipyramidal	$VOCl_2$ *trans*-$(NMe_3)_2$

Oxidation state	Coordination number	Geometry	Examples
	6[a]	Octahedral	VO_2 (rutile), K_2VCl_6, $VO(acac)_2(py)$, $V(acac)_2Cl_2$
	8	Dodecahedral	$[VCl_4(diars)_2]$, $V(S_2CMe)_4$
V^v d^0	4	Tetrahedral (C_{3v})	$VOCl_3$
	5	Trigonal bipyramidal	VF_5 (g), $VNCl_2(quinuclidine)_2$
		Square pyramidal	$CsVOF_4$
	6[a]	Octahedral	VF_5 (s), VF_6^-, V_2O_5 (very distorted, almost *tbp* with one distant O); $[VO_2(ox)_2]^{3-}$, V_2S_5
	7	Pentagonal bipyramidal	$VO(NO_3)_3 \cdot CH_3CN$, $VO(Et_2NCS_2)_3$

[a]Most important states.

5.1.1 The Chemistry of Vanadate in Water

A summary of current understanding of the vanadate system in water is given in **Figure 5.1**. This shows how the existence of various vanadate species depends on the pH and on the total concentration of vanadium. In these equilibria, the site of protonation in the species $[HVO_4]^{2-}$, $[H_2VO_4]^-$, etc., is an oxygen atom (not vanadium); a more precise representation would therefore be $[VO_3(OH)]^{2-}$, $[VO_2(OH)_2]^-$, etc. However, the customary formulation is retained for convenience [3].

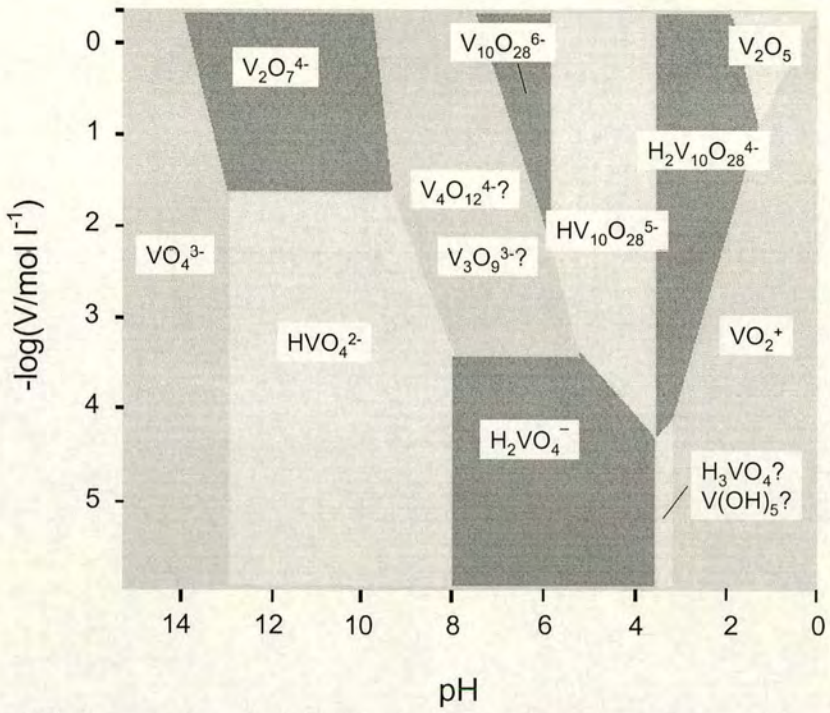

Figure 5.1 Occurrence of various vanadate and polyvanadate species as a function of pH and total concentration of vanadium [3].

It is evident from **Figure 5.1** that only in very dilute solutions are monomeric vanadium ions found and any increase in concentration, particularly if the solution is acidic, leads to polymerisation [3].

5.1.2 Vanadium in Biological System

The interest in vanadium chemistry from a biological and pharmacological perspective has exploded over the past 20 years, which is mainly based on the discoveries of the role of vanadium as an insulin mimic, and the presence of vanadium in certain haloperoxidases and nitrogenases [4, 5]. The chemical analogy between vanadates and phosphates is a key point for the understanding of how vanadium actually works in biological systems. One of the unclear questions is whether vanadate generally acts as a stable transition state analogue for phosphate blocking specific receptor sites or whether there are cases for which the vanadate substitution actually leads to new active sites with a completely different reactivity

with consequences for the pharmacological application and the toxicity of vanadium [6].

The particular importance of the biological function of vanadium is the ability of vanadium to influence phosphate-metabolising systems and the fact that vanadium is an inherent part of enzymatic active sites. For both types of vanadoenzymes known as vanadium-containing haloperoxidases and vanadium nitrogenases from the nitrogen fixing bacteria *Azotobacter*, functional analogs are found in nature which are either more widely spread or more efficient, e.g. the heme-containing haloperoxidases and the conventional nitrogenases with molybdenum cofactor, respectively. This leads to the question of how these enzyme systems evolved and in particular whether the vanadium-containing enzymes known today are retained functional analogs, which simply could sustain evolutionary forces [6]. New insight concerning these questions may be gained on the basis of newly found similarities for vanadate and phosphate in biological systems [7].

The wide-spread physiological effects of vanadium are mainly attributed to the similarity between vanadate(V) and phosphate. But there are also important differences between these two anions. At physiological pH values, monovanadate is found as doubly-protonated $[VO_2(OH)_2]^-$ species, whereas phosphate occurs in the monoprotonated form HPO_4^{2-}. This is also important for possible mechanisms of the transport systems for these two anions [8, 9, 10]. In addition, vanadium is easily reduced under physiological conditions to yield cationic species [V(V)/V(IV), E^o = 1.00 V, V(IV)/V(III), E^o = 0.34 V, V(III)/V(II), E^o = - 0.26 V]. The third difference is given by the pronounced ability of vanadium to adopt higher coordination numbers. The higher coordinative flexibility of vanadium can deliberately be used for the structural characterisation of phosphate metabolising enzymes [6].

Recently the crystal structures of several stable enzyme aggregates of phosphatases with vanadate as a transition state analogue have been reported. Interesting examples are the protein tyrosine phosphatases [11, 12], which are involved in signal transduction mechanisms for controlling and regulating intracellular processes (e.g.

the insulin receptor system). In these aggregates, the vanadium is trigonal bipyramidal and linked to the protein with a single axial bound cysteine residue, whereas the oxygen atoms of the vanadate moiety are involved in a hydrogen bonding network. A similar structure is found for the active site of rat prostatic acid phosphatase with the complexed transition state analogue vanadate [13].

It is said that vanadate complexes show insulin-mimetic effects [14]. The first chelated vanadium complex designed and tested chronically in *vivo* as an insulin mimetic agent (bis(maltolato)oxovanadium(IV), BMOV) has been thoroughly characterized chemically [15, 16] and tested biologically [17, 18].

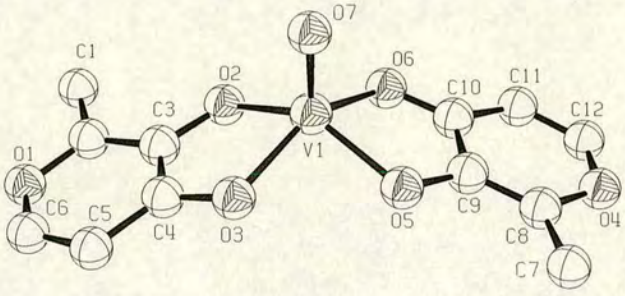

Figure 5.2 Crystal structure of bis(maltolato)oxovanadium(IV), (BMOV) [15].

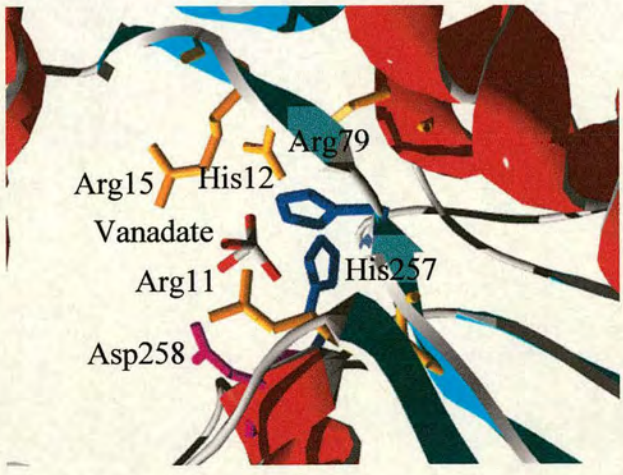

Figure 5.3 The metal binding site of rat prostatic acid phosphatase with the transition state analogue vanadate complex [13].

The overall structure of the enzyme remains unchanged upon binding of the metal oxyanions, only local conformational differences in the positions of some side chains at the active site were found. The vanadium is linked to the protein through an axially bound histidine residue, and forms a trigonal bipyramidal coordination geometry. The metal ion is within coordination distance of the His12 side chain which is located at one of the axial positions. The three equatorial oxygen atoms interact with the conserved residues Arg11, Arg15, Arg79 and His257. Within hydrogen-bonding distance of the axial oxygen atom is the side-chain of the conserved residue Asp258 [13].

It has been found that vanadium can bind to transferrin in blood [19, 20, 21]. Some research in *vivo* showed that in serum, vanadium is mainly bound to transferrin; however, a small amount of vanadium is also bound to albumin. Besides these two V-protein complexes, a significant part of vanadium occurred as readily exchangeable ("free") vanadium [22]. In *vitro*, vanadate binds to the metal-ion binding site in transferrin in the absence of anion as the dioxovanadium(V) cation, VO_2^+ [23]. It has been suggested that the ligands normally provided by the anion are supplied by the two oxo ligands of dioxovanadium. Thus VO_2^+ is believed to be coordinated in a trigonal bipyramidal or octahedral fashion to two tyrosines, an aspartate, as well as hydrogen bonded to a histidine and an arginine through the oxo group [24]. The study of possible relationships between iron and vanadium metabolism has been extended to the vanadium in the biochemical mechanisms which involve the exchange of iron between transferrin and ferritin. The results show that the maximum transfer was observed when V-transferrin and V-ferritin were mixed in their natural environments, such as plasma and liver cytosol, but no transfer of vanadium between two proteins was observed when the two proteins were mixed and incubated in a buffer at physiological pH. This suggests that the exchange of the vanadium between the two proteins is affected by biochemical factors which are present in the body [25].

5.1.3 Summary of Study in this Chapter

In order to investigate the binding of vanadate to the FBP. ^{51}V quadrupolar central transition (QCT) NMR, ^{31}P NMR and X-ray crystallography were used. (1) From ^{51}V NMR, information about the symmetry and motion of the bound metal ion was obtained from the chemical shift of ^{51}V. The effects of pH, ionic strength, solvent and temperature on the chemical shift of ^{51}V were also examined. (2) The phosphate vanadate analogy was investigated by the replacement of bound phosphate in *holo*-FBP by vanadate, and ^{31}P NMR was used to monitor the replaced phosphate. (3) The detail of vanadate binding to *apo*-FBP was studied by X-ray crystallography.

5.2 Experimental Methods

5.2.1 ^{51}V Quadrupolar Central Transition (QCT) NMR

Several properties of the ^{51}V nucleus make it ideal for studies of the protein-bound metal ion [26, 27]. ^{51}V is a quadrupolar nucleus (I = 7/2) with a high natural abundance (99.75%) [28], and very good NMR sensitivity (six times more sensitive than ^{31}P). The interaction of the nuclear quadrupole moment with the electric-field gradient at the vanadium nucleus allows for the determination of second-order quadrupole effects that can be used to characterise the symmetry of the local environment [29]. Spectra generated from a quadrupolar nucleus bound to a protein therefore can provide information on the symmetry of the ligand environment around the nucleus as well as its motion. This approach has been used successfully with the transferrins using ^{51}V NMR [30, 31, 32]. In addition, the nuclear quadrupole moment of ^{51}V is very small ($-0.052 \cdot 10^{-28}$ m^2) [30], thus it can potentially give well resolved spectra. The chemical shift range of ^{51}V is vast (> 4000 ppm) [30], and reflects its sensitivity to the coordinated ligands and local environment [24, 33].

The dominant relaxation mechanism for a half integer quadrupolar nucleus (nuclear spin, I > ½) is quadrupolar relaxation. This relaxation mechanism has features that are ideal for the study of macromolecules by NMR. The detection of higher resonance frequency half-integer quadrupolar nuclei in the limit of slow molecular

motion can reveal information about the motion of the metal ion as well as the symmetry of its local environment through second-order quadrupole interaction [34]. Different from spin = ½ nuclei, the line-width of the resonance of a half integer quadrupolar nucleus decreases as both molecular weight and magnetic field strength increase when $\omega_0\tau_c >> 1$ (ω_0, Larmor frequency; τ_c, rotational correlation time), due to the detection of only the central quadrupolar transition [30].

Details of quadrupolar relaxation theory can be found in various references [35, 36, 37]. Several equations have been derived to describe the properties relevant to the work in this Chapter. Information about the metal binding site of FBP is directly obtained from the chemical shift (δ_{obs}) and the line-width ($\Delta\nu_{1/2}$) of a bound nucleus. These two properties of the central transition ($m_I = ½ \rightarrow m_I = - ½$) reflect changes in the quadrupole coupling constant (χ), deviation from the isotropic chemical shift (δ_i), and τ_c of the bound metal ion. In the condition of slow isotropic molecular motion ($\omega_0\tau_c >> 1$), also called "far from extreme narrowing," the line width of the central transition of a I = 7/2 nucleus (^{51}V) is given by [37]:

$$\Delta\nu_{1/2} = 2.5 \cdot 10^{-3} \frac{\chi^2}{\nu_0^2 \tau_c}$$

χ (quadrupole coupling constant) is a measure of the coupling between the electric-field gradient and the nuclear quadrupole moment at the nucleus [38]. Thus, as the symmetry of the ligand field around the nucleus increases, χ and $\Delta\nu_{1/2}$ decrease, so this can be used as a measure of local environment around the atom of interest. Line-width is also inversely proportional to the resonance frequency of the nucleus (ν_0) and its rotational correlation time. This is opposite to what is observed for spin = ½ nuclei because as the above equation implies, slowing the motion of the metal ion, either by decreasing the temperature or increasing the size of the macromolecule to which it is bound, decrease the line-width of the NMR signal. The correlation times of the various transferrins and their half molecules [39] are of suitable magnitude to allow the detection of QCT NMR signals from various quadrupolar nuclei bound in

the metal-ion sites. Furthermore, by using high-field NMR spectrometers, the spectra of quadrupolar nuclei can be vastly improved through the narrowing of line-widths.

The observed chemical shift (δ_{obs}) of a quadrupolar nucleus experiencing slow isotropic motion can also be used to assess the symmetry of the local environment of the nucleus due to a "second order dynamic frequency effect" [37, 40] which causes an upfield shift of the central transition and is dependent on the external magnetic field. As derived elsewhere [41, 42], this shift can be described for a I = 7/2 nucleus:

$$\Delta\delta_d = \delta_{obs} - \delta_i = -2.5 \cdot 10^3 \frac{\chi^2}{\nu_0^2}$$

where δ_i is the isotropic chemical shift. If B_0 is increased, the second-order effect decreases, causing the observed signals to shift downfield toward the isotropic value. This second-order effect allows the calculation of χ simply by obtaining chemical shifts at different magnetic field strengths [43].

5.2.2 Sample Preparation and ^{51}V NMR of V-FBP

Vanadium-FBP samples for NMR spectroscopy were prepared by dissolving lyophilised *apo*-FBP in 6 ml 10 mM Tris, (H_2O/D_2O, 90%/10%, v/v), then 50 μl of saturated (20 °C) aqueous NH_4VO_3 (Aldrich, Cat. No. 20,555-9)) (H_2O/D_2O, 90%/10%, v/v) was added to the protein solution; the final pH was 7.8. The mixture was incubated in 37 °C on a water bath for 6 hours before the NMR spectra were recorded. The final concentration of the protein was 436 μM. The vanadium-*holo*-FBP complex was prepared as described in section 5.2.3. All ^{51}V NMR spectrum were recorded on a Bruker DMX 500 (γ_0 = 131.5 MHz) spectrometer fitted with a 5 mm BBO probe at 37 °C. $VOCl_3$ [vanadium(V) oxytrichloride, Aldrich, Cat. No. 20,089-1] was used as external shift reference; it was sealed in a capillary tube under argon atmosphere, and then this capillary tube was put inside a sealed 5 mm NMR tube containing D_2O. V-FBP spectra were acquired with a pulse length of 27.75 μs at 9 dB (90°). The relaxation delay was 3 seconds, and the frequency width was 66 kHz. The number of scans was 15872. The time domain size was 16 k and data were

processed with an exponential function, resulting in a line broadening of 20 Hz. Saturated NH_4VO_3 solutions (~ 50 mM) were prepared under various conditions to study the effects of solvent, temperature, buffer, ionic strength, and pH on the chemical shift of ^{51}V. The samples were prepared in D_2O, 10 mM Hepes (D_2O, pD 7.4, pD = pH*+0.4), (90% H_2O, 10% D_2O), (90% H_2O, 10% D_2O with 0.1 M KCl) and in (90% H_2O, 10% D_2O with 0.1 M KCl at pH 7-10). The pulse length was 27.75 μs at 9 dB (90°), relaxation delay 3 seconds, and frequency width was 66 kHz. The number of scans was 128. The time domain size was 16 k.

5.2.3 ICP-AES Analysis of V-FBP

V-FBP was purified on a cation exchange MonoS™ column eluted with 10 mM Tris, pH 8.0. The standard atomic absorption solution (Aldrich) was diluted with 10 mM Tris buffer (pH 8.0). The analysis was performed on a Thermo Jarrell Ash IRIS instrument. Total protein concentration was determined from the S concentration (1 S per mol protein; Met 308) without digestion. Values are averages of three determinations of the sample. The concentration of sulphur was determined from the emission at 182.034(142) nm, and the concentration of vanadium from the emission of 309.311(84) nm.

5.2.4 ^{31}P NMR Studying of Vanadate Displace Phosphate from *holo*-FBP

^{31}P NMR spectra were recorded at 202.4 MHz at 310 K on a Bruker DMX 500 spectrometer using a 5 mm BBO probe. An aliquot of a saturated NH_4VO_3 solution (100 μl) was added to 500 μl of *holo*-FBP solution (920 μM, in 10 mM Tris, 50 mM NaCl, pH 8.0), and the mixture was incubated at 37 °C for 102 hours, then 70 μl D_2O was added to the protein solution to provide an NMR lock. The spectrum was collected using a pulse width of 22.65 μs at 9.00 dB, relaxation delay 2 s, 8192 data points and 14336 transients. The spectral width was 30 ppm and the middle of the spectrum was set as 0.0 ppm. A sealed capillary containing 85% H_3PO_4 was used as external standard. The spectra were processed using exponential functions (line-broading of 20 Hz).

5.2.5 Preparation of V-FBP

Vanadium(V)-FBP was prepared by mixing the freshly prepared saturated NH_4VO_3 solution with *apo*-FBP solution in 10 mM Tris buffer, pH 8.0 and incubated in 37 °C water bath for 3 hours. The product was initially purified using a PD-10 column, followed by ultrafiltration (Amicon™ YM-30, Millipore) with 10 mM Tris, pH 8.0.

5.2.6 Crystallisation of V-FBP

V-FBP was crystallised using the hanging drop method. Large needle crystals appeared in the drop composed of 21% PEG 4000, 0.5 M imidazole buffer (pH 6.4) within two weeks. However, the unit cell of this form of crystal is large (25 molecules per unit cell), so the resolution was not good (~3.5Å).

Better V-FBP crystals were prepared by soaking. High quality *apo*-FBP crystals harvested from a drop composed of 31% PEG 1450, 0.4 M imidazole buffer, (pH 7.2) were soaked in an NH_4VO_3-containing solution for more than 12 hours at 17 °C. The soaking solution was prepared by mixing 20% stock solution and 80% well solution (31% PEG 1450, 0.4 M imidazole buffer, pH 7.2). The stock solution was prepared with 30% PEG 1450, 0.4 M imidazole buffer, pH 7.2 and saturated with NH_4VO_3.

5.3 Experimental Results

5.3.1 Factors that Influence the Chemical Shift of ^{51}V

As shown in **Figure 5.1**, the chemistry of vanadium in aqueous solution is very complex. A large variety of species can form depending on the pH, ionic strength, and concentration [44]. Previous studies have shown that vanadate can react with various buffers [33], and pH has a marked effect on the spectra of aqueous vanadium. Here, the effects of solvent, ionic strength, temperature, and buffer on the chemical shift of ^{51}V were examined at neutral pH. Also, the effect of pH on the chemical shift of ^{51}V was examined in the pH range of 7-10.

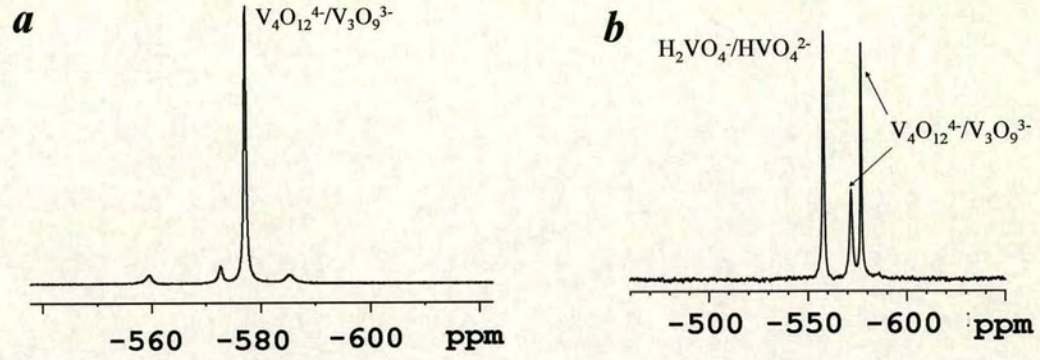

Figure 5.4 ***(a)*** ^{51}V NMR spectrum of saturated aqueous NH_4VO_3 (~50 mM). ***(b)*** ^{51}V NMR spectrum of 0.4 mM NH_4VO_3 in 90% H_2O, 10% D_2O, 10 mM Tris, pH 8.0.

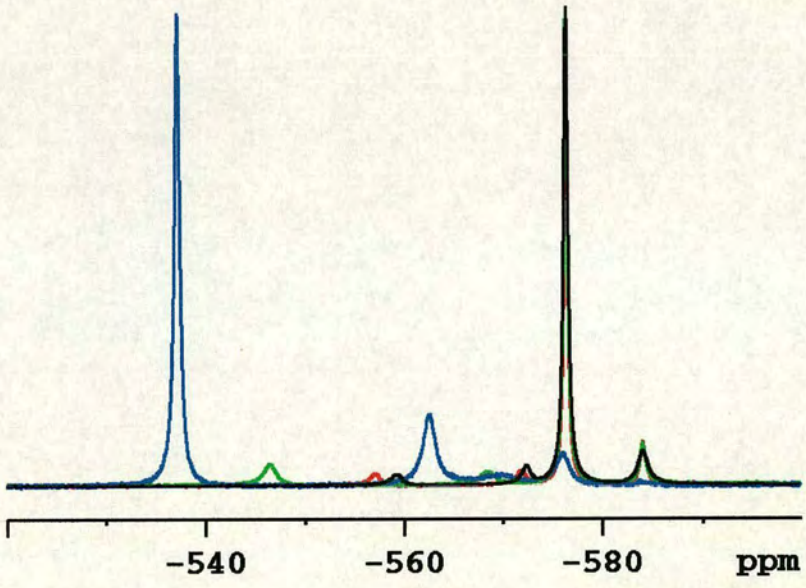

Figure 5.5 pH effects on ^{51}V chemical shift. The sample is a saturated aqueous NH_4VO_3 solution. ^{51}V spectra were recorded at pH 7.23 (black line), pH 8.02 (red line), pH 9.00 (green line) and pH 10 (blue line). Main peaks of red line, green line and black line at -577 ppm were perfectly overlaid.

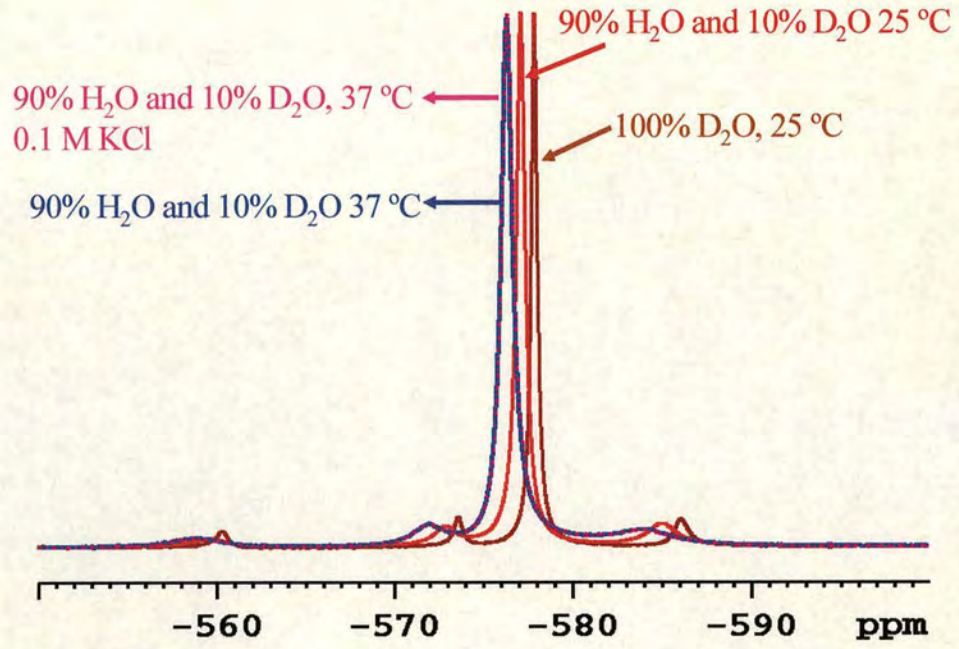

Figure 5.6 Solvent, temperature and ionic strength effects on ^{51}V chemical shift. The sample was saturated aqueous NH_4VO_3 solutions (~50 mM). The pink line and the blue line are perfectly overlaid.

All peaks in **Figure 5.4 – Figure 5.6** were assigned according to references 30, 31, 32. $VOCl_3$ was used as external standard (0 ppm).

^{51}V NMR spectra shown in **Figure 5.4** reveal that different species exist in saturated aqueous NH_4VO_3 solutions (~50 mM) and diluted NH_4VO_3 solution (0.4 mM). **Figure 5.4*a*** shows that the main species in the saturated NH_4VO_3 solution (~50 mM) is $V_4O_{12}^{4-}/V_3O_9^{3-}$ (a sharp single peak at about -578 ppm). However, as shown in **Figure 5.4b**, when the sample was diluted from ~50 mM to 0.4 mM, and the spectra were recorded at the same solvent, buffer, pH as the saturated sample, a new peak appeared, which was assigned to $HVO_4^{2-}/H_2VO_4^-$ (-557.8 ppm). Two sharp peaks at -571.9 ppm and -576.8 ppm were assigned to $V_4O_{12}^{4-}/V_3O_9^{3-}$. The results revealed that a mononuclear vanadate species was formed when the sample was diluted. The concentration of vanadate in the sample used to record the spectrum in **Figure 5.4*b***

was almost the same as in the V-FBP sample used to record the ^{51}V NMR spectrum, so the spectrum in **Figure 5.4*b*** can be used to be a reference spectrum for the ^{51}V spectrum of V-FBP.

Figure 5.5 shows the effect of pH on chemical shift of ^{51}V. The results show that between pH 7 and pH 9, the peak for the main species was stable (fully overlapped, black line, pH 7.23, red line, pH 8.02, green line, pH 9.00). However, when the pH was increased to 10 (blue line), the peak was shifted downfield by 39.1 ppm. For the ^{51}V NMR experiments performed in this Chapter, the pH range of the reference sample (0.4 mM aqueous NH_4VO_3) and the V-FBP is between pH 7 and pH 8, hence, there is no pH effect on the chemical shift difference between the two samples.

The effects of solvent, temperature and ionic strength on the chemical shift of ^{51}V were investigated by ^{51}V NMR and the spectra are shown in **Figure 5.6**. The results show that when the solvent is changed from 100% D_2O (brown line) to 90% H_2O and 10% D_2O (red line), the main peak shifted to downfield by 0.6 ppm. In the same solvent, when the temperature was changed from 25 °C (red line) to 37 °C (blue line), the main peak shifted downfield by 0.8 ppm. At the same temperature, when 0.1 M KCl was added (pink line), there was no change in the NMR spectra at all. So, ^{51}V NMR experiments for both reference sample and V-FBP sample were performed in the same solvent and the same temperature.

5.3.2 Vanadium(V) Binds to *apo*-FBP and *holo*-FBP

There is no previous report of the binding of vanadate to FBP, although it has been reported that vanadate can bind to transferrin [21]. Here, the binding of vanadate to *apo*-FBP was investigated by ^{51}V NMR, which shows that vanadate does bind.

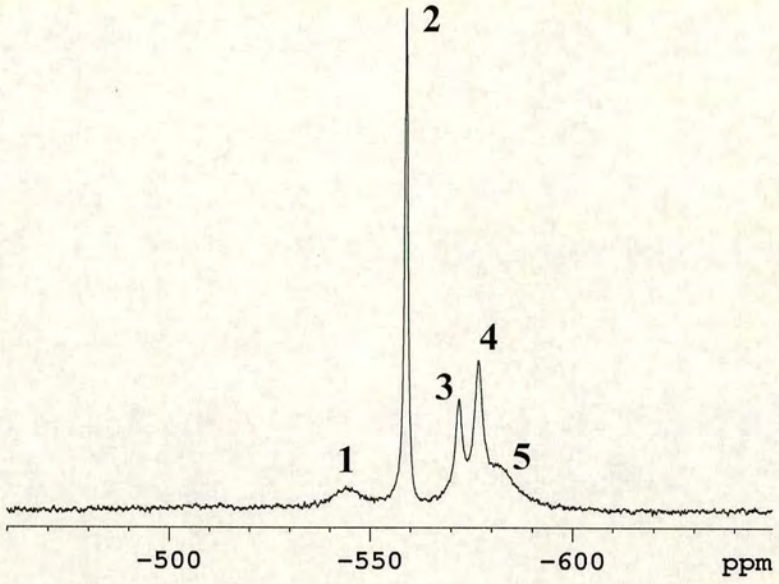

Figure 5.7 ^{51}V spectrum of V-FBP (~436 μM) with excess vanadate (V / protein = 10:1) at 37 °C, in 10 mM Tris, pH 8.0.

Compared with the reference spectrum shown in **Figure 5.4*b***, new peaks appeared at -543.8 ppm (peak **1**), and there is a broad peak (peak **5**, -582 ppm) overlapping with peak **3** and **4**. According to the chemical shift of free species in literatures [30], and the chemical shift of bound vanadate in transferrin [30], peak **1** is assigned to the species VO_2^+ bound to the protein. The broad peak (peak **5**) overlapped with peaks **3** and **4** is assigned to $V_4O_{12}^{4-}/V_3O_9^{3-}$ species, the broadening of the peak is due to binding to the protein. However, when excess vanadate in the protein solution was removed with gel-filtration chromatography, the ICP-AES analytical result of this purified sample shows that the V/protein ratio is 0.99 ± 0.2.

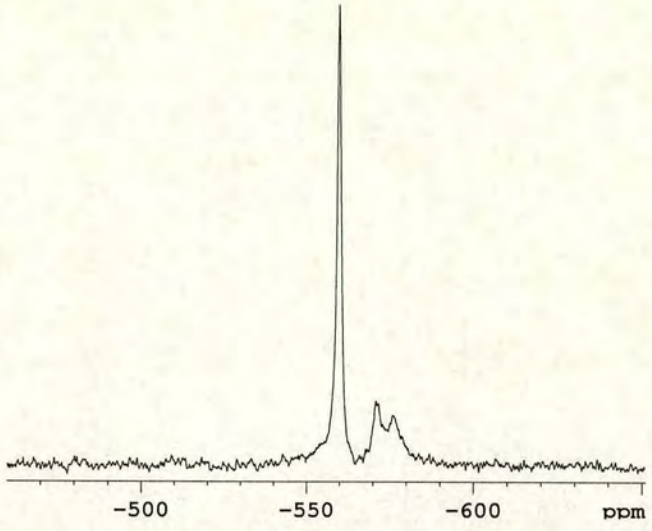

Figure 5.8 ^{51}V NMR spectrum of ammonium vanadate (V/protein = 10:1) in 11 mM Tris, 100 mM NaCl, incubated with *holo*-FBP (690 μM).

Figure 5.7 is the spectrum of *apo*-FBP incubated with excess of vanadate, **Figure 5.8** is the spectrum of *holo*-FBP incubated with a 11-fold molar excess of vanadate. Comparing the two spectra, it is evident that the peak at -543.8 ppm in **Figure 5.7** has disappeared **in Figure 5.8.** This reveals that in the *holo*-FBP sample, vanadate cannot displace Fe(III) from the metal binding site; this is also confirmed by the presence of the red colour of the *holo*-FBP sample, which means that Fe(III) is still bound to the protein. In both spectra, in addition to the sharp peak at -558 ppm of free vanadate, the peaks at around -580 ppm are broad, which means that vanadate species $V_4O_{12}^{4-}/V_3O_9^{3-}$ interact with the protein. Nevertheless, bonds between VO_2^+ and $V_4O_{12}^{4-}/V_3O_9^{3-}$ and the protein might be weak. This is the reason why $V_4O_{12}^{4-}$ $/V_3O_9^{3-}$ are lost during the purification of V-FBP by chromatography and the ICP-AES analytical result showed that only one vanadium atom is bound strongly to one protein molecule.

One of the most important biological properties of vanadium is its analogy to phosphate. ^{51}V NMR proved that vanadate can interact with *holo*-FBP without the replacement of the ferric ion; then the question is what is the nature of the interaction site between vanadate and *holo*-FBP? Can vanadate play the same role as phosphate

in *holo*-FBP? To find the answer of this question, ^{31}P NMR was used to investigate whether vanadate can replace phosphate from *holo*-FBP.

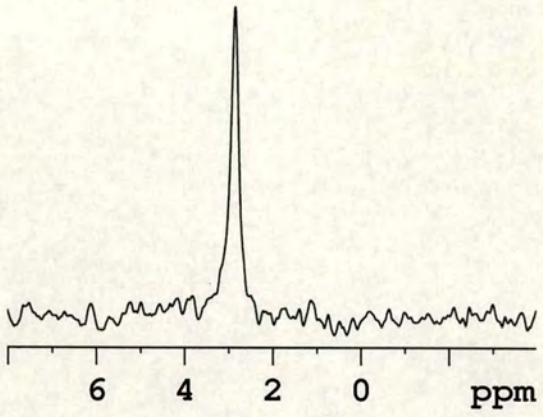

Figure 5.9 ^{31}P NMR spectrum of *holo*-FBP (690 μM) containing an 11-fold molar excess of vanadate in 10 mM Tris, 100 mM NaCl. The sample is the same as used to record the spectrum in **Figure 5.8**.

A ^{31}P NMR spectrum of *holo*-FBP was recorded, and no phosphate signal was found due to the paramagnetic effect of Fe(III). However, after the addition of an 11-fold molar excess of vanadate, a phosphate peak appeared at 2.9 ppm, which was assigned to free phosphate. This shows that vanadate can displace phosphate in *holo*-FBP. This result suggests that in V-FBP, in the presence of excess vanadate, vanadate clusters ($V_4O_{12}^{4-}$/$V_3O_9^{3-}$, as shown in **Figure 5.7**) can bind to VO_2^+ in the role of an anion.

5.3.3 Crystallisation of V-FBP

Crystal of V-FBP were prepared by soaking *apo*-FBP crystals in a vanadate-containing soaking solution. Diffraction data were collected using a rotating anode generator RF591 (λ = 1.488 Å) by Dr. Dmitriy Alexeev (ICMB, University of Edinburgh).

Table 5.2 Crystallographic Data for Vanadium(V)-FBP

Wavelength	1.542 Å
Resolution	2.00 Å
Crystal System	Hexagonal
Space Group	$P3_2$
Unit Cell Parameter	$a = b = 146.93$ Å, $c = 114.70$ Å
	$\alpha = \beta = 90^\circ$ $\gamma = 120^\circ$
Refl. Collected/Unique	2102722/346722
Molecules/Asymmetric Unit	9
Temperature (K)	100
Completeness (%)	98.3%
Overall I/Sigma(I)	12.93
Redundancy	6.1

The structure determination work for V-FBP by Dr. Dmitriy Alexeev is still in progress. The initial results show that the V-FBP crystal has the same space group as the other FBP crystals. The crystal structure of V-FBP will hopefully give a clear view of the coordination geometry of V-FBP in the metal binding site of FBP.

5.4 Discussion

V-FBP is the first observation of vanadium bound to bacterial transferrin. Experiments performed in this Chapter suggest that vanadate can bind to *apo*-FBP

strongly as the species VO_2^+. In the presence of excess vanadate, vanadate clusters $V_4O_{12}^{4-}/V_3O_9^{3-}$ can also interact with the protein. However, the interaction between the vanadate cluster and protein is weak, and the vanadate cluster was readily lost during the purification procedure with gel-filtration chromatography.

In addition, vanadate can also react with *holo*-FBP, and the anion of *holo*-FBP (phosphate) can be replaced by vanadate in the presence of an 11-fold molar excess of vanadate, but the bound Fe(III) cannot be replaced by vanadate. This discovery matches the performance of vanadium in *vitro* studying - its analogy to phosphate.

These results suggest that in the presence of excess vanadate, vanadate clusters $V_4O_{12}^{4-}/V_3O_9^{3-}$ may play the role of anion in the protein and interact with *holo*-FBP at the position of phosphate. As has been discovered in previous Chapters, vanadate clusters $V_4O_{12}^{4-}/V_3O_9^{3-}$ may form weak bonds with FBP-bound vanadium ion via oxygen bridges to form a bigger cluster.

The high-quality V-FBP crystal diffracts to 2.0 Å resolution. This provides a chance to clarify all the assumptions of the bonding and geometry situation in the metal binding site of V-FBP with further structural determination work.

References

1 Lide, D.R. *CRC Handbook of Chemistry and Physics*, **72nd edition** p4 (1992).

2 Cotton, F. A., Wilkinson, G., Murillo, C. A., Bochmann, M., *Advanced Inorganic Chemistry,* **Sixth Edition**, Wiley, New York, Chichester, p715 (1999).

3 Greenwood, N. N., and Eranshaw A., *Chemistry of the Elements*, **First edition**, Pergamon Press Ltd., Oxford, England, p1138 (1984).

4 Slebodnick, C., Hamstra, B.J., Pecoraro, V.L., *Struct. Bonding* **89**, 51 (1997).

5 (Eds.: Sigel, H., Sigel, A.), *Met. Ions. Biol.l Syst.,* **Vol 31***: Vanadium and Its Role in Life*, Marcel Dekker, New York, 1995.

6 Plass, W., *NIC Symposium 2001, proceedings* (Eds.: Rollnik, H., Wolf, D.) *NIC series,* **Vol. 9**, p103 (2002).

7 Plass, W., *Angew. Chem. Int. Ed.*, **38**, 909 (1999).

8 Quiocho, F.A., Ledvina, P.S., *Mol. Microbiol.* **20**, 17 (1996).

9 Luecke, H., Quiocho, F. A., *Nature* **347**, 402 (1990).

10 Herzberg, O., Reddy, P., Sutrina, S., Saier, J.M.H., Reizer, J., Kapadia, G., *Proc. Natl. Acad. Sci. USA* **89**, 2499 (1992).

11 Denu, J.M., Lohse, D. L., Vijayalakshmi, M. A., Saper, J. E., Dixon, J. E., *Proc. Natl. Acad. Sci. USA* **93**, 2493 (1996).

12 Zhang, M., Zhou, M., van Etten., R. L., Stauffacher, C. V., *Biochemistry* **36**, 15 (1997).

13 Lindqvist, Y., Schneider, G., Vihko, P., *Eur. J. Biochem.* **221**, 139 (1994).

14 Orvig, C., Thompson, K. H., Battell, M., McNeill, J. H., in *Met. Ions.Biol. Syst., **Vol. 31**: Vanadium and Its Role in Life* (Eds.: Sigel, H., Sigel, A.), Marcel Dekker, New York, 575 (1995).

15 Caravan, P., Gelmini, L., Glover, N., Herring, F. G., Li, H., McNeill, J. H., Rettig, S. J., Setyawati, I. A., Shuter, E., Sun, Y., Tracey, A. S., Yuen, V. G., Orvig, C., *J. Am. Chem. Soc.*, *117*, 12759 (1995).

16 Hanson, G. R., Sun, Y., Orvig, C., *Inorg. Chem.*, *35*, 6507 (1996).

17 Yuen, V. G., Orvig, C., McNeill, J. H., *Can. J. Physiol. Pharmacol.*, *71*, 263 (1993).

18 Yuen, V. G., Pederson, R. A., Dai, S., Orvig, C., McNeill, J. H., *Can. J. Physiol. Pharmacol.*, *74*, 1001 (1996).

19 Chasteen, N. D., Grady, J. K. and Holloway, C. E., *Inorg. Chem.* **25**, 2754 (1986).

20 Sabbioni, E. and Marafante, E., *Bioinorg. Chem.* **9**, 389 (1978).

21 Harris, W. R., Friedman, S. B., and Silberman, D., *J. Inorg. Biochem.* **20**, 157 (1984).

22 De Cremer, K., Van Hulle, M., Chery, C., Cornelis, R., Strijckmans, K., Dams, R., Lameire, N., Vanholder, R., *J. Biol. Inorg. Chem.* **7**, 884 (2002).

23 Harris, W. R. and Carrano, C. J., *J. Inorg. Biochem.* **22**, 201 (1984).

24 Butler, A. and Carrno, C. J., *Coord. Chem. Rev.* **109**, 61 (1991).

25 Sabbioni, E., Rade, J., Bertolero, F., *J. Inorg. Biochem.* **12**, 307, (1980).

26 Howarth, O.W., *Prog. NMR Spec.* **22**, 453 (1990).

27 Rehder, D., *Bull. Magn. Reson.* **4**, 33 (1982).

28 http://www.webelements.com (1993-2003).

29 Lapina, O. B., Mastikhin, V. M., Shubin, H. A., Krasilnikov, V. N., and Zamaraev, K. I., *Prog. NMR Spec.* **24**, 457 (1992).

30 Saponja, J. A., Vogel, H. J., *J. Inorg. Biochem.*, **62**, 253 (1996).

31 Butler, A., Danzitz, M. J., Eckert, H., *J. Am. Chem. Soc.*, **109**, 1864 (1987).

32 Butler, A. and Eckert, H., *J. Am. Chem. Soc.*, **111**, 2802 (1989).

33 Chasteen, N. D., *Struc. Bond.* **53**, 105 (1982).

34 Rehder, D., in *Vanadium In Biological Systems*, Chasteen, N. D., Ed., Kluwer Academic Publishers, Boston, 173, (1990).

35 Bull, T. E., Forsén, S., and Turner, D. L., *J. Chem. Phys.* **70**, 3016 (1979).

36 Hubbard, P. S., *J. Chem. Phys.* **53**, 985 (1970).

37 Westlund, P. –O., and Wennerström, *J. Magn. Reson.* **50**, 451 (1982).

38 Aramini, J. M., *Metal Ion NMR studies of Metalloproteins*. PhD dissertation, University of Calgary, Calgary, Alberta, Canada (1994).

39 Aramini, J. M. and Vogel, H. J., *J. Am. Chem. Soc.* **115**, 245 (1993).

40 Werbelow, L. G., *J. Chem. Phys.* **70**, 5381 (1979).

41 Aramini, J. M., Germann, M. W., and Vogel, H. J., *J. Am. Chem. Soc.* **115**, 9750 (1993).

42 Aramini, J. M., McIntyre, D. D., and Vogel, H. J., *J. Am. Chem. Soc.* **116**, 11506 (1994).

43 Germann, M. W., Aramini, J. M., and Vogel, H. J., *J. Am. Chem. Soc.* **116**, 6971 (1994).

44 Willsky, G. R., in *Vanadium in Biological Systems*, Chasteen, N. D., Ed., Kluwer Academic Publishers, Boston, p25, (1990).

Chapter 6 Conclusions and Future Work

6.1 Conclusions

FBP is a convergent nodal point for Fe(III) trafficking subsequent to a variety of very different transport strategies across the outer membrane. It belongs to the transferrin superfamily, which encompasses the mammalian transferrin proteins. Transferrins and FBP are structurally and functionally related [1].

All previous studies have shown that FBP is a mono-iron complex, and it was assumed that iron is transported across the periplasm only as mononuclear centres. The Fe_3-FBP characterised in this work (Chapter 3) appears to be the first example of an oxo tri-iron centre in a metalloprotein. It is well known that (hydr)oxo-di-iron centres are present in ribonucleotide reductase, methane monooxidase, and hemerythyrin [2]. Ferritin has a particulate core of Fe(O)OH, taken up as Fe(II) and oxidised in gated pores in the protein coat [3, 4]. Sulfide-bridged di, tri- and tetra-iron clusters are found in ferredoxins. Ferredoxins have a multitude of diverse roles including electron transport, and probably sustained early life in a highly reducing environment. [5]. The finding that FBP can bind oxo-iron cluster adducts suggests the possibility that small fragments of (hydr)oxo iron minerals could be involved in iron trafficking. It is known that FBP has access to the outer surface of the bacteria [6], so clusters might be acquired directly from the external environment by periplasmic FBP or might be assembled from uptake of mononuclear iron (**Figure 6.1**). A database search revealed that nearly half of the bacteria which possess a FBP homolog also possess a FecA homolog (**Appendix 1**). FecA might therefore be considered as a possible donor of polynuclear iron to FBP.

In the structure of mono Fe-NTA-FBP (**Figure 3.14**), Fe(III) is shielded from solvent by the chelated NTA ligand in much the same way as by bound EDTA in the recently reported structure of *Haemophilus influenzae* Fe-EDTA-FBP in which His9 had been mutated to Gln [7]. The authors concluded that the open cleft conformation was trapped by crystal packing forces, but the Fe-NTA-FBP was crystallised from

formed complex, thus, the cleft opening observed does not appear to depend on such packing forces.

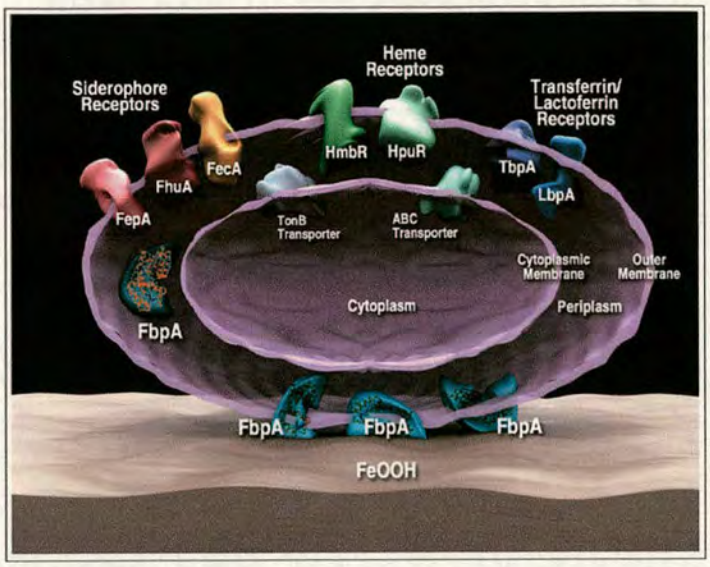

Figure 6.1 Stylized view of iron acquisition pathways for Gram-negative bacteria. Shown across the top of the bacterium are outer membrane (OM) receptor-mediated uptake of iron from Fe^{3+}–siderophores by FhuA, FepA, FecA or any of numerous other siderophore receptors; hemin or hemoglobin by HmbR or HpuR or other heme receptors; and Fe^{3+}–transferrin or Fe^{3+}–lactoferrin by TbpA or LbpA, respectively. Cell-surface reductases can also be present that facilicate iron transport across the outer membrane (not shown). In some cases TonB or ABC transporters, which transport the iron across the cytoplasmic membrane (CM), are coupled with the OM-receptor transport processes. Fbp also facilitates transport of iron across the periplasmic space to the CM. Along the bottom of the bacterium, the question of whether Fbp can sample the outer bacterial surface is raised. Can Fbp come in contact with oxophilic metal–containing minerals to sequester Fe^{3+} and other metal ions? [1]

As shown by the structures of Fe_3-FBP and *apo*-FBP (**Figure 3.15** and **Figure 3.13**), the mobility and acid-base properties of the side-chains provide the dityrosyl motif of FBP with a potentially versatile role in the capture and release of iron. Although in most of the protein molecules in the unit cell of Fe_3-FBP the tri-iron cluster is

anchored by Tyr196 as a triply-bridging ligand and by Tyr195 as a monodentate terminal ligand, either Tyr residue can also act as a single arm anchor for the cluster. Hence, the versatile structural roles of these Tyr residues may provide facile mechanisms for iron uptake and release either as mono- or polynuclear centres. A potential role for Tyr196 is to guide iron complexes into the cleft. Evidently the two iron-binding tyrosine residues can have distinctly different roles within the binding cleft of FBP as has been illustrated for human transferrin by mutation of Y95 and Y188, the metal-binding tyrosines in the N-lobe cleft [8], and for the duck NII domain fragment [9].

Fe(III) in open-cleft FBP is accessible and potentially reactive. The phosphatase activity observed (**Section 3.3.6**) provides a mechanism for signalling iron status by coupling cluster breakdown and cleft-closure around a single iron. This might also be an alternative way for bacteria to obtain phosphate in the phosphate poor environment.

The crystal structure of hafnium-FBP (**Section 4.3.4**) gives a good example of hetero-metal FBP interaction. Hafnium can bind to *apo*-FBP as oxo-hafnium clusters with 3 – 5 hafnium ions. This suggests that the metal binding cleft of FBP can accommodate large clusters, which means larger iron mineral fragment could be formed in the metal binding motif. Phosphate is important but it is not essential for the hafnium loading process.

Vanadium showed dual roles in FBP. Vanadate can bind to *apo*-FBP, and clusters were also formed in the metal binding site in the presence of excess of vanadium. In addition, vanadate can take the place of phosphate in *holo*-FBP, which shows its property as a phosphate mimic in FBP. The crystals of V-FBP which I prepared will, it is hoped, eventually yield the structural details of V-FBP at atomic resolution.

It has been found that transferrin can bind to more than 30 metals [10]. Previous studies show that both hafnium and vanadium can bind to the N- or C- lobes of transferrin as single ions [11, 12]. In these studies of Hf-FBP and V-FBP, it is found that they are quite similar to Fe-FBP; both metals can form clusters in the metal

Reference

1 Butler, A., *Nat. Struct. Biol.* **10**, 240-241 (2003).

2 Kurtz, D. M., *J. Biol. Inorg. Chem.* **2**, 159-167 (1997).

3 Theil, E.C., *Annu. Rev. Biochem.*, **56** 289-315 (1987).

4 Chasteen, N. D. and Harrison, P. M., *J. Struct. Biol.* **126**, 182-194 (1999).

5 Rees, D.C., Howard, J.B., *Science* **300**, 929 (2003).

6 Ferreirós, C., Criado, M. T., and Gómez, J. A., *Comp. Biochem. Physiol.* **B123**, 1-7 (1999).

7 Shouldice, S. R., Dougan, D. R., Skene, R. J., Tari, L. W., McRee, D. E., Yu, R., and Schryvers, A. B., *J. Biol. Chem.* **278**, 11513-11519 (2003).

8 He, Q-Y., Mason, A. B., Woodworth, R. C., tam, B. M., MacGillivray, R. T. A., Grady, J. K. and Chasteen, N. D., *Biochemistry* **36**, 14853-14860 (1997).

9 Kuser P., Hall, D. R., Haw, M., Neu, M., Evans, R. W., and Lindley, P. F., *Acta Cryst.*, **D58**, 777 (2002).

10 Welch, S. in *Transferrin: the iron carrier* (Welch, S., Ed.), 1-127, CRC Press, Boca Raton, FL. (1992).

11 Becker, G., Appel, H., Neu, M., Schwab, F. J., Thies, W. G., *Hyperfine Interactions*, **80**, 1161-1165 (1993).

12 Harris, W. R. and Carrano, C. J., *J. Inorg. Biochem.* **22**, 201 (1984).

Appendix 1

Sequence (in bold) and secondary structure of *holo*-FBP from *Neisseria gonorrhoeae* (PDB code 1d9y, McRee etal, unpublished). Secondary structure is calculated and described according to the method of Kabsch and Sander, *Biopolymers* **22**, 2577-2637 (1983). The assignments are: H=helix; B=residue in isolated beta bridge; E=extended beta strand; G=3_{10} helix; I=pi helix; T=hydrogen bond turn; S=bend.

Chain 1D9Y:A

Compound	**Periplasmic Iron-Binding Protein**		
Type	**Protein**		
Molecular Weight	**33641**		
Number of Residues	**309**		
Number of Alpha	**12**	Content of Alpha	**40.13**
Number of Beta	**11**	Content of Beta	**17.15**

(A) Amino acid sequence of N gonorrhoeae Fbp and conserved residues in homologs. Sequence with grey highlights for residues conserved in organisms listed in **(B)**, sequence with underline highlighs for residues bound to Fe(III) in *holo*-FBP.

(A) Sequence and secondary structure

```
  1 DITVYNGQHK EAAQAVADAF TRATGIKVKL NCAKGDQLAG QIKEEGSRSP
    EEEEE S H HHHHHHHHHH HHHH   EEE EES HHHHHH HHHHHGGG

 51 ADVFYSEQIP ALATLSAANL LEPLPASTIN ETRGKGVPVA AKKDWVALSG
    SEEEESSHH HHHHHHHTT  B    TTTHH HH  TT     TTS  EE EE

101 RSRVVVYDTR KLSEKDLEKS VLNYATPKWK NRIGYVPTSG AFLEQIVAIV
    EEEEEEEETT T  GGGS SS GGGGTTGGGT TTEEEETT H HHHHHHHHHH

151 KLKGEAAALK WLKGLKEYGK PYAKNSVALQ AVENGEIDAA LINNYYWHAF
    HHHTHHHHHH HHHHHHHHSE EESSHHHHHH HHHTTSSSEE EEETHHHHHH

201 AREKGVQNVH TRLNFVRHRD PGALVTYSGA AVLKSSQNKD EAKKFVAFLA
    HHHH GGG   EEEE   TTT GGG EEEEEE EEETT SSHH HHHHHHHHHH

251 GKEGQRALTA VRAEYPLNPH VVSTFNLEPI AKLEAPQVSA TTVSEKEHAT
    THHHHHHHHT TS  EE  TT    SS    H HHHT         HHHHHHHH

301 RLLEQAGMK
    HHHHHHT
```

(B) Based on an SIB BLAST network service search (S. F. Altschul, et al. *Nucleic Acids Res.* **25**, 3389 (1997); exception, Halobacterium sp. G229S). Fe ligands (H9, E57, Y195, Y196) in closed cleft form of *Neisseria* and *Haemophilus* Fe-P_i-Fbp are underlined in (**A**).

Archaea		
Halobacterium sp	.	
Bacteria		
Neisseria gonorrhoeae	Neisseria meningitidis	Actinobacillus actinomycetemcomitans
Haemophilus influenzae	Pseudomonas aeruginosa*	Pseudomonas putida*
Serratia marcescens*	Yersinia pestis*	Rhizobium loti*
Yersinia enterocolitica*	Anabaena sp.*	Synechocystis sp.
Bacillus halodurans	Synechococcus elongatus	Campylobacter jejuni
Vibrio cholerae*	Synechococcus sp.	Vibrio parahaemolyticus*
Ehrlichia chaffeensis	Pasteurella multocida	Brucella melitensis
Pseudomonas syringae pv.*	Agrobacterium tumefaciens*	Shewanella oneidensis*
Bacillus halodurans	Clostridium perfringens	Pasteurella haemolytica
Pseudomonas fluorescens†	Burkholderia fungorum†	Nostoc sp.†
Trichodesmium erythraeum†	Nitrosomonas europaea†	

*Bacteria with homolog of *E. coli* FecA † Sequences available only up to residues 196-218

Appendix 2

Summary Information for the Structure of Hf-FBP from Protein Data Bank (PDB code 1O7T)

Compound: Mol_Id: 1; Molecule: Iron Binding Protein; Chain: A, B, C, D, E, F, G, H, I; Engineered: Yes

Exp. Method: X-ray Diffraction

Classification: Ferric-Binding Protein

Source: *Neisseria gonorrhoeae*

Resolution [Å]: 1.65 *R-Value:* 0.164

Space Group: P 3_2

Unit Cell: *dim [Å]:* *a* 148.13 *b* 148.13 *c* 115.84
angles [°]: *alpha* 90.00 *beta* 90.00 *gamma* 120.00

Polymer Chains: A, B, C, D, E, F, G, H, I *Residues:* 2781

Atoms: 23605

HET groups:

ID	*Name*	*Formula*	*Retrieve All PDB IDs Containing*
HF3	SMALLEST HF-OXO-PHOSPHATE CLUSTER HF3	$H_7O_{15}Hf_3P$	HF3
HF5	HF OXO CLUSTER HF5	$5(H_{12}O_{21}Hf_5)$	HF5
PHF	HF-OXO-PHOSPHATE CLUSTER PHF	$3(H_{11}O_{23}Hf_5P)$	PHF

Named Sites: HF1, HF2, HF3, HF4, HF5, HF6, HF7, HF8, HF9